

JOURNAL OF SCIENCE & ENGINEERING

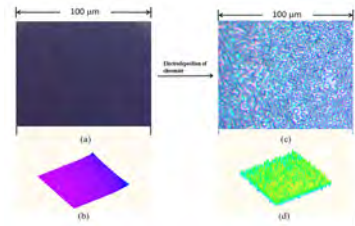
HITTITE



A Simple and Rapid Method for Preparing Carbon Nanopore Electrode Ensemble by Coating A Glassy Carbon Electrode with Chromate 01-07

by Faruk Gökmeşe

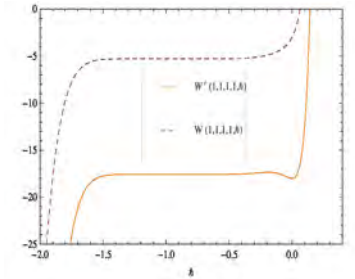
A simple preparation method for carbon nanopore electrode ensemble (CNEE) was reported. The CNEE consists of a number of pinholes which remain after coating a carbon surface with chromate. The transformation from transient to steady-state voltammetric behavior of carbon surface was presented.



On Critical Buckling Loads of Euler Columns With Elastic End Restraints 09-13

by Musa Başbük

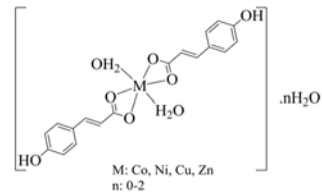
In this paper, homotopy analysis method (HAM) is applied to find buckling loads of Euler columns with elastic end restraints. The critical buckling loads obtained by using HAM are compared with the exact analytic solutions in the literature.



Synthesis and Thermal Characterization of p-Coumaric Acid Complexes of CoII, NiII, CuII and ZnII Metal Cations and Biological Applications 15-22

by Sineray Koç

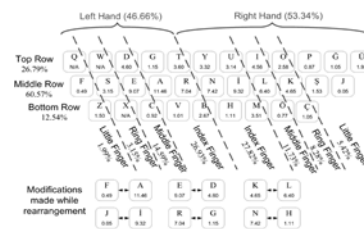
In this study, metal complexes of p-coumaric acid ligand with the transition metal cations (CoII, NiII, CuII, ZnII) were synthesized. The structure of the synthesized complexes was studied via elemental analysis, infrared and ultraviolet-visible spectroscopy, magnetic measurements, melting point and thermal analysis.



Optimized Rearrangements of Turkish Q and F Keyboards by Means of Language-Statistics and Simple Heuristics 23-28

by Asum Egemen Yılmaz

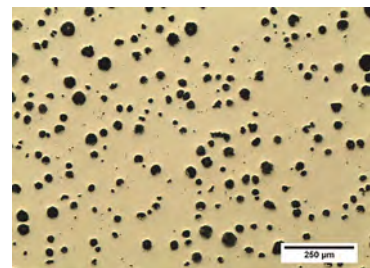
In this study, based on the language (particularly n-gram) statistics of Turkish extracted from a large corpus of meaningful written text of various categories, we try to propose some improvements via some simple rules and heuristics.



Microstructural Analysis of Austempered Ductile Iron Castings 29-34

by Barış Çetin

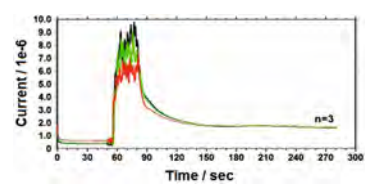
In this paper the efforts regarding to a localization project of ADI is presented. In a more detailed manner, the first locally produced ADI which cannot satisfy the mechanical properties stated in ISO 17804 is compared with the original sample which is conform with the standard.



Non-Enzymatic Phenol Determination in River Water Over Modified Electrode with Poly(3-methylthiophene) Removal from The Aqueous Solution

35-40

by Muammer Kavanoz

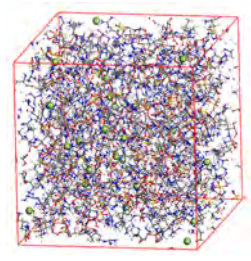


This paper describes non-enzymatic phenol determination using poly(3-methylthiophene) coated Pt electrode.

The Structural and Thermal Characterization of New Cu-Arginate Complex; Experimental and Simulated Hydrogen Adsorption Properties

41-49

by Zarife Sibel Şahin

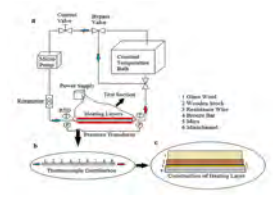


The copper-arginate complex was synthesized and characterized by using FTIR, TG/DTA-DSC, UV-Vis spectroscopy and elemental analysis methods. In addition, hydrogen storage capabilities were investigated.

Experimental Analysis of Laminar Flow and Heat Transfer in Multi-Port Finned Mini-Channel

51-60

by Berk Çevrim



In this study, fluid flow and heat transfer in a multi-port finned minichannel with a rectangular cross section was investigated experimentally under the constant heat flux boundary condition.

Journal Name : HITTITE JOURNAL OF SCIENCE AND ENGINEERING
Year : 2016
Managing Editor : Prof. Dr. Ali KILIÇARSLAN
Managing Office : Hitit University Graduate School of Natural and Applied Sciences
Managing Office Tel : +90 364 219 40 00
Publication Language : English
Publication Type : Peer Reviewed, Open Access, International Journal
Delivery Format : 2 times a year (semi-annually)
Print ISSN : 2149-2123
Publisher : Bir Medya
Publisher Address : Yeni yol Mah. Gazi 12. Sok. No:9/13 ÇORUM
Publisher Tel : +90 364 225 66 64



This new issue of Hittite Journal of Science and Engineering contains eight manuscripts from the disciplines of chemistry, mathematics, materials science and engineering, mechanical engineering, industrial engineering and electrical and electronics engineering. These manuscripts were first screened by Section Editors using plagiarism prevention software and then reviewed and corrected according to the reviewer's comments. I would like to express my gratitude to all our authors and contributing reviewers of this issue.

I would like to inform all our readers that we are still in the evaluation period to be indexed and abstracted by TR Dizin (ULAKBIM), Scopus and Web of Science. We strongly hope to be indexed in one of these with our next issue.

I would like to thank to the President of Hitit University, Prof. Dr. Reha Metin Alkan, for his constant interest in HJSE and also to the Associate Editors of HJSE, namely Dr. Dursun Ali Kose and Dr. Oncu Akyildiz, as well as our Production Editors Dr. Kazim Kose and Mustafa Guzel for their invaluable efforts in making of the journal.

It's my pleasure to invite the researchers and scientists from all branches of science and engineering to join us by sending their best papers for publication in Hittite Journal of Science and Engineering.

Dr. Ali Kiliçarslan

Editor-in-Chief

Director of Graduate School of Natural and Applied Sciences of Hitit University

A Simple and Rapid Method for Preparing Carbon Nanopore Electrode Ensemble by Coating A Glassy Carbon Electrode with Chromate

Faruk Gökmeşe, Ebru Gökmeşe and Zuhale Emire
Hitit University, Department of Chemistry, Çorum, TURKEY

ABSTRACT

A simple preparation method for carbon nanopore electrode ensemble (CNEE) was reported. The CNEE consists of a number of pinholes which remain after coating a carbon surface with chromate. The transformation from transient to steady-state voltammetric behavior of carbon surface was presented. The effect of electrochemical technique to structure of chromate film was investigated. The optimum deposition time and optimum concentration of chromate solution for coating carbon surface substantially were determined for bulk electrolysis (BE) technique. On the other hand for cyclic voltammetry (CV), the effects of scan rate, number of cycle and coating solution concentration on forming uniform partly-insulating layer have been examined. The CNEE prepared by BE technique showed larger hysteresis which means more resistivity than the one prepared by CV. Under the optimum coating conditions the thinner and more useful CNEE with lower resistivity can be prepared by CV.

Article History:

Received: 2015/11/11
Accepted: 2016/04/18
Online: 2016/06/30

Correspondence to: Faruk Gökmeşe,
Hitit University, Faculty of Science and
Arts, Department of Chemistry, Çorum,
TURKEY

Tel: +90 (364) 2277000/1632
Fax: +90 (364) 2277005
E-Mail: farukgokmese@hitit.edu.tr

Key Words:

Carbon nanopore electrode ensemble (CNEE), chromate, steady-state current, radial diffusion, microelectrode.

INTRODUCTION

Since the early 1980s, a number of voltammetric studies have been carried out with microelectrodes that have dimensions that are smaller than an order of magnitude. The electrochemical behavior of these tiny electrodes is significantly different from classical electrodes, whose diameters are generally in between 1.5 mm and 3 mm, and appears to offer advantages in certain analytical applications [1-4]. Such electrodes have been called microscopic electrodes, or ultramicroelectrodes, to distinguish them from classical voltammetric electrodes. Nanoelectrodes may be defined as electrodes with a critical dimension in the nanometer range, here critical dimension is the dimension that controls the electrochemical response. On the other hand, a microelectrode or ultramicroelectrode may be viewed as any electrode in which the electrode is smaller in magnitude than the diffusion layer which can be achieved in an experiment, yielding an electrode with a critical dimension of the order of 25 μm . When the electrode's critical dimension is decreased to the

order of the thickness of the electrical double layer or the molecular size, the experimental behavior starts to deviate from that of the larger electrodes [5].

The primary reason for the use of ultramicroelectrodes and smaller electrodes is the benefit obtained from the enhanced mass transport [6-11]. As electrodes decrease in size, 3-dimensional (radial) diffusion becomes dominant and results in faster mass transport. This high rate of diffusion at small electrodes enables measurement of kinetics by steady-state experiments rather than by transient techniques. Analytical measurement systems can potentially exploit the increased mass transport characteristics of microelectrodes in achieving shorter response times to freely-diffusing species in solution. Another analytical benefit should be the increased faradaic to charging current ratio obtained, due to the enhanced mass transport for diffusion-controlled faradaic currents.

Microelectrodes take several forms. The most

common one is a planar electrode formed by sealing a carbon fiber with a radius of 5 μm or a gold or platinum wire having dimensions from 0.3 to 20.0 μm into a fine capillary tube; the fiber or wires are then cut flush with the ends of the tubes. Cylindrical electrodes are also used, in which a small portion of the wire extends from the end of the tube. There are several other forms of these electrodes.

Besides above mentioned benefits of nanoelectrodes, there are some difficulties in their fabrication, and handling as well as the sensitivity of the instrumentation available with which to make reliable electrochemical measurements. Fortunately, several commercial sources of microelectrodes now exist with higher prices than that of bigger ones. In order to solve the sensitivity of instrumentation problems, the microelectrode arrays or ensembles have been fabricated. The individual electrodes in the array operate in parallel thus amplifying the signal while retaining the beneficial characteristics of the microelectrodes. However, it is generally required a complicated and expensive equipment to prepare these arrays or ensembles [12].

Clark and McCreery examined the oxygen reduction reaction on copper, platinum, and glassy carbon electrodes, with regard to its inhibition by exposure of the electrode to chromate ion, Cr (VI), in NaCl solution [13]. They reported that all three electrode materials exhibit a mass transport limited current for the oxygen reduction reaction at sufficiently negative potentials, but this current was strongly inhibited in the presence of Cr (VI).

In this study a simple and fast method has been proposed for fabricating an electrode which exhibit microelectrode behavior while being a classical GC voltammetric electrode. Despite the microelectrodes are commercially available, this method may represent an economically viable alternative to the do-it-yourself approach. In addition, since most of the commercial carbon fiber microelectrodes contain Epoxy resins [14, 15] it is difficult to modify these electrodes. The electrode prepared with this method has a potential usage in modification studies.

For coating the normal size commercial glassy carbon electrode, $\text{K}_2\text{Cr}_2\text{O}_7$ solution in NaCl was used. Both cyclic voltammetry (CV) and constant potential coulometry (bulk electrolysis, BE) were used to reduce Cr (VI) and form Cr (III) film on the glassy carbon surface. The conductivity of this coated surface has been studied with ferrocene electrooxidation, which is known as outer sphere redox system that does not require adsorption to the electrode surface.

It is not the purpose of the present study to provide a detailed mechanism for Cr (VI) reduction, yet we agree on

the mechanism proposed by Hurley et al. [16]. Mainly, we aimed to use the pin holes retained on the surface while forming the Cr (III) monolayer as individual microelectrodes. The effects of voltammetric technique used for coating, scan rate and number of cycle for CV, coating time and $\text{K}_2\text{Cr}_2\text{O}_7$ concentration for BE were investigated.

2. MATERIALS AND METHOD

2.1. Reagents

Acetonitrile (ACN), ferrocene (FC), silver nitrate (AgNO_3) and tetrabutylammonium tetrafluoroborate (TBATFB) were purchased from Sigma-Aldrich Chemical. All other chemical compounds used in this study ($\text{K}_2\text{Cr}_2\text{O}_7$, NaCl etc.) were reagent grade commercial products. Milipore Water Purification System was used to obtain deionized water with resistivity of 18.3 $\text{M}\Omega\cdot\text{cm}$. Unless otherwise noted, 0.1 M NaCl served as the supporting electrolyte for aqueous solutions and 0.1 M TBATFB for acetonitrile. The stock coating solution was 0.005 M $\text{K}_2\text{Cr}_2\text{O}_7$ in 0.1 M NaCl and the other coating solutions were prepared from this stock solution by diluting. The testing solution for the coated electrodes was prepared as 0.001 M FC in 0.1 M TBATFB.

2.2. Carbon nanopore electrode ensemble (CNEE)

The production of carbon nanopore electrode ensemble (CNEE) by coating GC electrode with Cr (VI) was executed in two electrochemical techniques which were BE and CV, respectively. Firstly, the electrolysis potential was determined from CV experiment of 0.005 M $\text{K}_2\text{Cr}_2\text{O}_7$ solution in 0.1 M NaCl depending on the reduction peak potential of chromate. Thus the suitable electrolysis potential was chosen as -1 V vs Ag/AgCl which is 0.2 V beyond the end of reduction peak. The produced CNEE from both techniques was controlled by CV and LSV of 0.001 M FC solution in 0.1 M TBATFB in ACN. The GC electrode was coating for 10 min in 0.005 M $\text{K}_2\text{Cr}_2\text{O}_7$ solution in 0.1 M NaCl by applying the electrolysis potential to cover most of its conductive area. Following the coating step, the electrode was rinsed with water and ACN, respectively, and then placed in 0.001 M FC solution in ACN.

2.3. Instrumentation and electrochemical techniques

The electrochemical studies were carried out with CH Instruments (CHI) Model 660C Electrochemical Analyzer equipped with an ENTEK C4 Cell Stand and CHI 200 Picoamp Booster and Faraday Cage. The experimental solutions were purged with argon (99,99% purity) for at least 15 min just before the voltammetric experiments and throughout the hydrodynamic experiments like

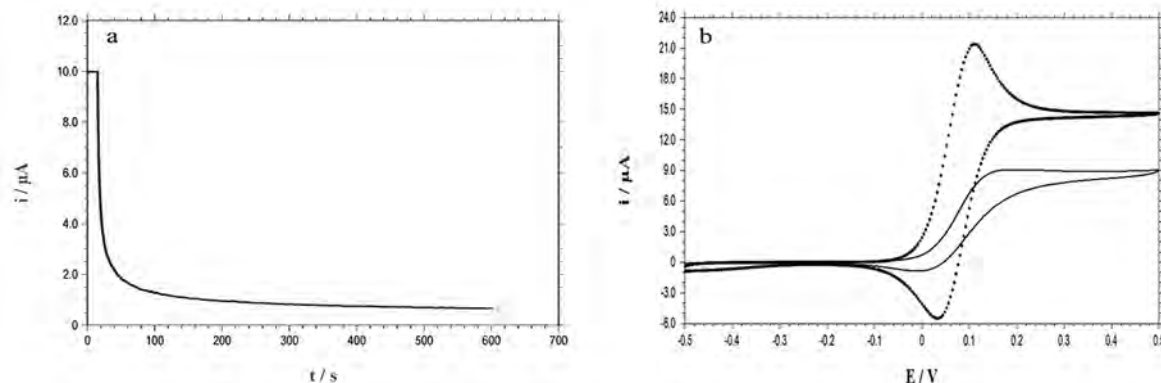


Figure 1. (a) Amperometric result for 0.05 M $K_2Cr_2O_7$ in 0.1 M NaCl in water at GC electrode, deposition potential is -1 V, deposition time is 10 min. (b) Cyclic voltammograms of 1 mM FC in 0.1 M TBATFB in ACN at Bare-GC (---) and Cr-GC (—) electrodes, scan rate is 0.01 V/s

Bulk Electrolysis. The working electrode was Glassy Carbon electrode (CHI 104 Model, 3 mm diameter, GC) and the counter electrode was a Pt wire. The reference electrode employed in non-aqueous experiments was $Ag|Ag^+$ containing 0.01 M $AgNO_3$ and 0.1 M TBATFB in ACN medium. Experiments in water utilized $Ag/AgCl$ as the reference electrode and all potentials quoted with respect to this reference. The electrochemical coatings were made with the use of cyclic voltammetry (CV), and bulk electrolysis (BE) techniques. The coated surface was inspected by CV and linear scan voltammetry (LSV) for determining the electrochemical behavior.

Commercial GC electrode (CHI 104, 0.071 cm^2 area) were polished successively in 1-, 0.3-, and $0.05\ \mu\text{m}$ alumina slurries made from dry Buehler alumina and deionized water on Buehler polishing microcloth. Polished GC electrodes were sonicated in water and then in a mixture of 50:50 (v/v) 2-propanol/acetonitrile in both cases for 10 min. After sonication, the electrode was rinsed with ACN and then with the water, dried with an argon gas stream.

The Cr(III) oxyhydroxide coated surface of GC obtained from both optimization studies for electrolysis time and electrolysis solution concentration was characterized by using 0.001 M FC solution in 0.1 M TBATFB in ACN. The effect of electrolysis time on the number and dimensions of

members of the ensemble was investigated for four different potential application period, $t=2, 5, 10$ and 20 min.

3. RESULTS AND DISCUSSION

A typical $i-t$ curve acquired from BE experiment is given in Figure 1a for $0.005\text{ M } K_2Cr_2O_7$ solution in 0.1 M NaCl in aqueous medium. Figure 1b shows the voltammetric responses (0.01 V/s) of bare GC (dashed) and chromate coated GC (solid line) in the 0.001 M FC solution. The voltammetric response of GC electrode has changed after coating step. In agreement with the theory and previous results of voltammetry at classical disc shaped electrodes, the voltammetric response for bare GC displays peak-shaped voltammogram. On the other hand, the voltammogram for chromate coated GC has a sigmoidal shape, characteristic of the radial diffusion. The magnitude of the steady-state current ($\sim 9\ \mu\text{A}$) was much more than that of the current for a single micro/nano scale electrode (in nano ampere scale) at the same time retained steady-state behavior as expected from the nano electrode ensemble (NEE) at intermediate sweep rate [17-20]. These results were demonstrated that GC surface was coated partly with chromate blocking the electron transfer.

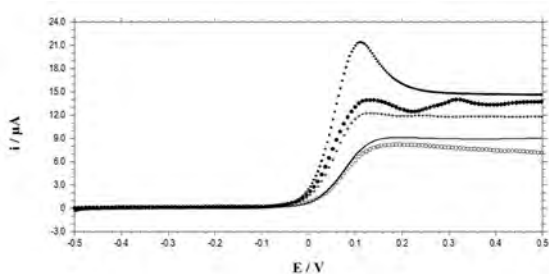


Figure 2. The effect of deposition time on the coating of GC surface with chromate, (♦) Bare-GC, (◆) 2 min, (◻) 5 min, (◻) 10 min and (◻) 20 min deposition times, scan rate is 0.01 V/s for all voltammograms.

The linear sweep voltammetric responses of the electrodes coated for different periods were shown in Figure 2. According to Figure 2 the oxidation peak or steady-state current for FC decreased with increasing electrolysis time while the peak or half wave potential was almost stable. The steady-state behavior started after 5 min deposition and further the active electrode area became smaller. Even though the 10 min coating had an ideal steady-state behavior the 20 min coating could also be used in order to get smaller CNEE. In the studies of concentration effect on coating, 0.0001, 0.0005, 0.001 and 0.005 M $K_2Cr_2O_7$ solutions prepared in 0.1 NaCl were used. It was found that the oxidation peak or steady-state current of FC decreased with increasing the concentration of coating solution. It

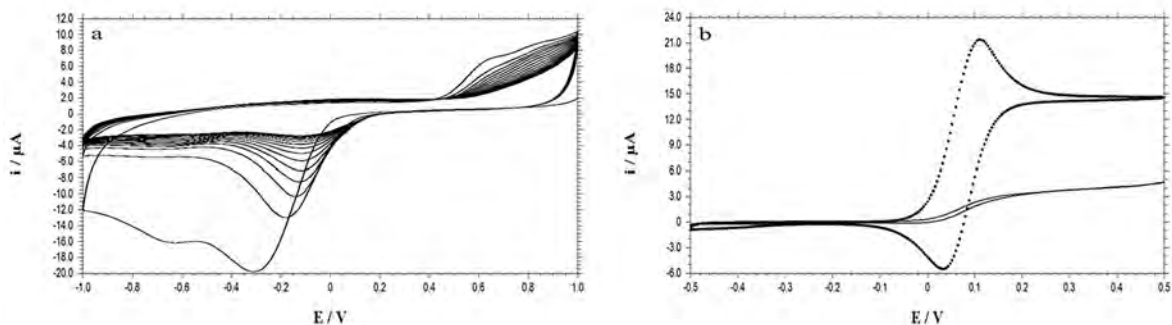


Figure 3. (a) The successive cyclic voltammogram for 0.05 M $K_2Cr_2O_7$ in 0.1 M NaCl in water at GC electrode, scan rate is 0.1 V/s, number of cycle is 15. (b) Cyclic voltammograms of 0.001 M FC in 0.1 M TBATFB in ACN at Bare-GC (---) and Cr-GC (—) electrodes, scan rate is 0.01 V/s

means that the higher concentration for coating solution the wider coated area on the GC surface. Otherwise the longer deposition process like 20 min in more concentrate solution caused the chromate film to be thicker and the voltammetric response started to turn into a peak shape voltammogram. These results proved that all pin holes among the coating behaves as a nanopore electrode, individually [21].

Alternatively, another voltammetric technique, CV, was investigated for coating method. The successive cyclic voltammogram of 0.005 M $K_2Cr_2O_7$ in 0.1 M NaCl for 15 cycles at 0.1 V/s scan rate is given in Figure 3a. The chromate reduction peak is seen in the first cycle at 0.31 V and shifts to the more positive potentials together with decreasing peak current at the further scans. The shifted in peak potential and the decrease in peak current result from both changing the electrode surface feature and degrowth of the active surface area, respectively. The voltammetric response after coating the GC electrode using CV technique supported these results. The shape of cyclic voltammogram turned from a peak to a sigmoidal form and the resulting steady-state current is also smaller than the peak current obtained at the bare GC surface (Figure 3b). The effect of scan rate on CV coating of GC surface was illustrated in Figure 4. The electrode coated with chromate by CV at 0.01, 0.1, 1 and 10 V/s scan rates, respectively. The number of cycle and the potential scan interval were adjusted to five and “-1 V – 1 V”, respectively, for all the experiments in order to be sure that

all the parameters were same except scan rate.

Figure 4a shows the transformation of the voltammetric response from a peak-shaped form to the sigmoid forms. The coating at high scan rate (10 V/s) with CV was not sufficient to get small enough pin holes needed for a steady-state response. Smaller pin holes (e.g. individual nano electrode) could be obtained by slowdown the scan rate in CV coating. When the scan rate is 1 V/s for coating experiment it is possible to have the sigmoidal steady-state voltammogram for oxidation of FC. The steady-state current decreased with decreasing scan rate on the coating stage. Furthermore, the coating at 0.01 V/s has almost totally inhibited the electron transfer from and to the GC electrode. Detailed inspection of the coatings done at 1 V/s and 0.1 V/s scan rates shows that the more useful CNEE can be prepared by 0.1 V/s scan rate (Figure 4b). The voltammograms for two of them have a sigmoidal shapes but the one belonging to 1 V/s scan rate coating displays more hysteresis than the other. The faster scan causes to form thicker chromate film, more and bigger pin holes because of enhanced electrolysis speed. On the other hand, more homogenous CNEE with thinner chromate film could be generated with the scan rate of 0.1 V/s as seen from the cyclic voltammetric response with very small hysteresis.

The thickness of chromate film is also affected by the number of cycles applied in the coating method. In this part

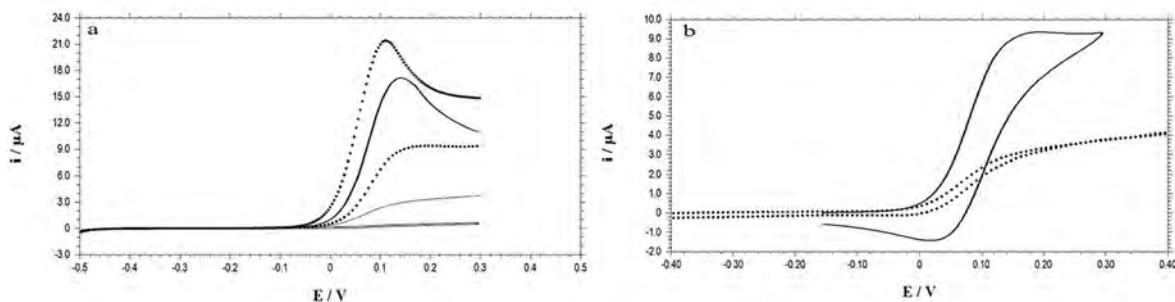


Figure 4. (a) The effect of scan rate on the CV coating of GC surface. The linear scan voltammograms of 0.001 M FC in 0.1 M TBATFB at (◆) Bare-GC, after coating at (-) 10 V/s, (•) 1 V/s, (-) 0.1 V/s and (◊) 0.01 V/s scan rates. (b) The cyclic voltammograms of 0.001 M FC in 0.1 M TBATFB at chromate coated-GC at scan rates of (-) 1 V/s and (•) 0.01 V/s. Scan rate for all voltammetric responses is 0.01 V/s.

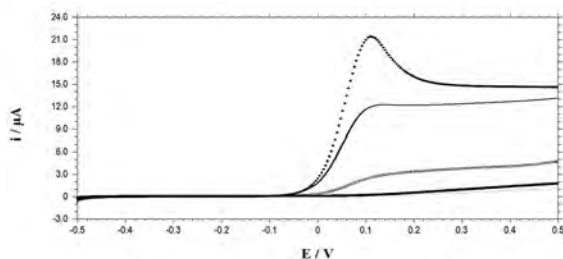


Figure 5. The effect of number of cycle on the CV coating of GC surface with chromate. The linear scan voltammograms of 0.001 M FC in 0.1 M TBATFB at (●) Bare-GC, after coating with (○) 1 cycle, (◻) 5 cycles, (◻) 10 cycles and (◻) 15 cycles, scan rate is 0.01 V/s for all voltammograms.

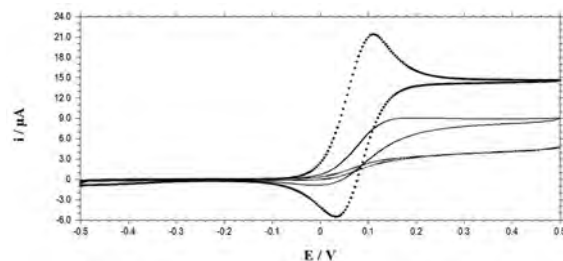


Figure 6. The comparison of electrochemical coating techniques. The cyclic voltammograms of 0.001 M FC in 0.1 M TBATFB at (●) Bare-GC, (○) the chromate coated-GC prepared by BE coating for 10 min deposition and (◻) the chromate coated-GC prepared by CV coating at 0.1 V/s scan rate for 15 cycles, scan rate is 0.01 V/s for all voltammograms.

of study four different electrodes were prepared with 1, 5, 10 and 15 cycles at 0.1 V/s scan rate and compared with each other and bare GC as well. When the optimum scan rate (0.1 V/s) was used the steady-state response was reached even with only one cycle coating (Figure 5). The active electrode area and thus the steady-state current decrease as the number of cycle increase. Moreover, if the number of cycle is equal to or more than 15 one can obtain almost totally insulating surface which is called as “dead electrode”. From the results acquired so far, the optimum experimental conditions for preparing the better designed, readily made CNEE by CV technique have determined as the scan rate of 0.1 V/s, the cycle number of 10 and the coating solution

concentration of 0.005 M.

The comparison of the two methods used for coating GC surface is shown in Figure 6. The electrolysis time for BE method is 10 min and the total experiment time for deposition step by CV is 3.33 min (for 5 cycle potential scan between 1 V and -1 V at 0.1 V/s scan rate). As seen from the experiment times the CV method is 3 times faster than BE method. In addition the limiting current of FC on CNEE prepared by BE is about 3 times higher than the other. It means that despite the shorter experiment time for CV method the coating ratio of bare GC is higher compared with BE method. On the other hand, when we inspect the voltammograms generated by two different NEEs closely, both of them have a sigmoidal shape but the one belonging to BE method displays much more hysteresis. The CV technique causes not only smaller nanopores on the chromate coated surface but also thinner coating with lower resistivity.

The prepared surface by using optimum conditions has been inspected under an optical microscope (Figure 7). It is seen from the figure that the polished GC electrode surface is very smooth (Figure 7a and 7b). After electrodeposition of chromium on the GC, a new inhomogeneous surface forms (Figure 7c and 7d). It is also seen that there are too many round pin holes and different shape holes and cracks behaving conductive area.

In addition to optical zoom the optical micrograph of chromium coated surface (Figure 8a) has been also magnified by the software program 5 times digitally (Figure 8b). Thus the micron and submicron pin holes could be seen closely. From the 3D form (Figure 8c) of the new micrograph the roughness of the surface is also realized.

A summary of CNEE formation is presented Figure 9a. At the chromate deposition step in either BE or CV,

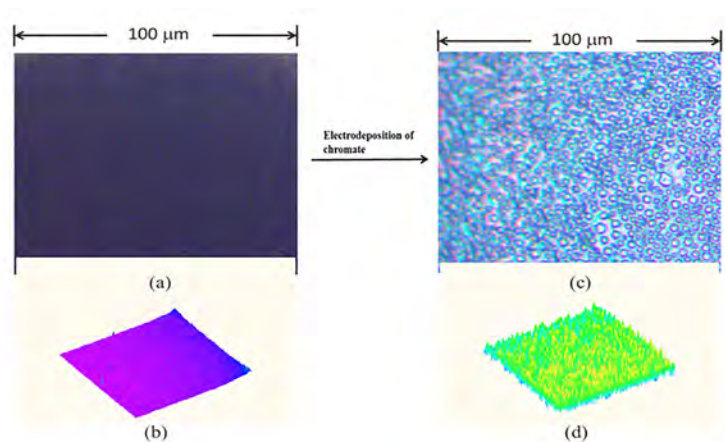


Figure 7. (a) Optical micrograph of polished GC surface, (b) 3D image of polished GC surface, (c) optical micrograph of chromium coated GC surface, (d) 3D image of the coated GC surface.

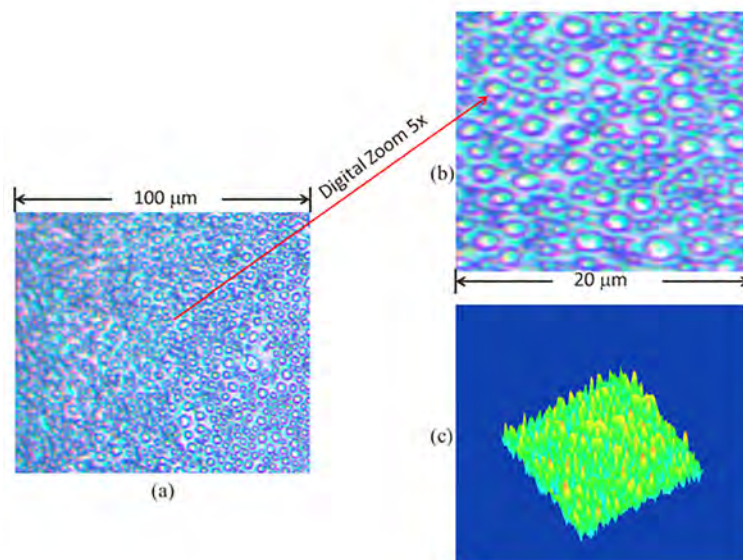


Figure 8. (a) Optical micrograph of chromium coated GC surface, (b) 5X digitally magnified image of the micrograph, (c) 3D image of the magnified micrograph.

the GC surface partially coated with chromate which blocks the electron transfer from or to GC surface. After deposition, some parts of the GC surface remain uncoated and let electrons pass. The voltammetric behaviors of the two surfaces are different (Figure 9b). As seen from Figure 9b, the partially coated GC surface shows steady-state voltammetric behavior corresponding to the radial diffusion regime while the voltammetric response is dominating by planar diffusion regime at bare GC surface. This steady-state response of chromate coated GC surface is similar to that of a single nanopore electrode [22].

4. CONCLUSION

The preparation and electrochemical characterization of carbon nanopore electrode ensemble was described. It was concluded that the chromate solution could be used as partly insulating agent for carbon surface and thus to prepare a carbon nanopore electrode ensemble. The electrochemical coating technique was also affective on the thickness of coating and number of holes act as nanopore electrode. Two different electrochemical techniques were examined as coating method and

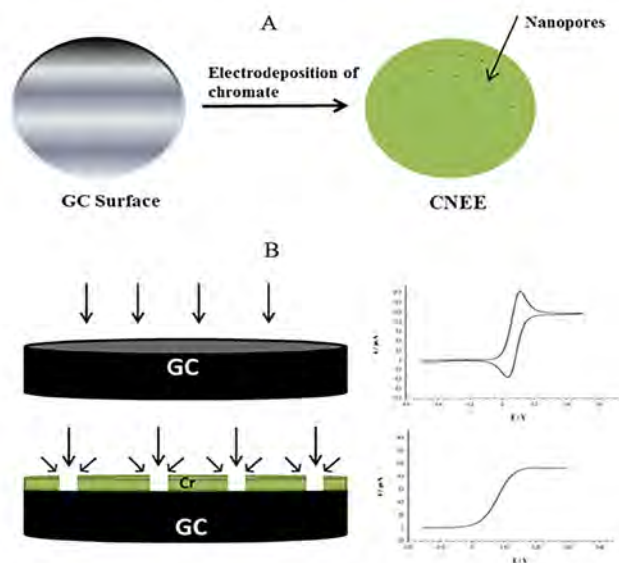


Figure 9. Scheme of a CNEE prepared by electrochemical chromate deposition of GC electrode. (A) preparation of the CNEE, (B) two different diffusion regimes and corresponding voltammetric responses at bare-GC and chromate coated GC. Note: Some dimensions are only indicative and not in scale.

compared for determining optimum preparation conditions. The CV technique was found useful to form a thinner and more homogenous partly insulating film on GC surface in shorter experiment time. On the other hand the BE method could also be used at coating step for different purposes.

ACKNOWLEDGEMENTS

This study was supported by Hitit University Scientific Research and Development Office and by The Scientific and Technological Research Council of Turkey, 2209-Undergraduate Scholarship Programme.

REFERENCES

1. Michael AC, Wightman RM. Microelectrodes. In *Laboratory Techniques in Electroanalytical Chemistry*, 2nd ed. Kissinger PT, Heineman WR. Eds. Ch. 12. New York: Marcel Dekker. 1996.
2. Zoski CG. In *Modern Techniques in Electroanalysis*, Vanisek P. Eds. Ch. 6. New York: Wiley. 1996.
3. Wightman RM. Voltammetry with Microscopic Electrodes in New Domains. *Science* 240 (1988) 415–420.
4. Pons S, Fleischmann M. The Behavior of Microelectrodes. *Analytical Chemistry* 59 (1987) 1391A–1399.
5. Arrigan DWM. Nanoelectrodes, nanoelectrode arrays and their applications. *Analyst* 129 (2004) 1157–1165.
6. Wightman RM, Wipf DO. Voltammetry at Ultramicroelectrodes. In *Electroanalytical Chemistry*, ed. A. J. Bard, Marcel Dekker, New York, 15 (1989) 267–353.
7. Bond AM. Past, Present and Future Contributions of Microelectrodes to Analytical Studies Employing Voltammetric Detection. *Analyst* 119 (1994) R1–R21.
8. Forster RJ. Microelectrodes–New Dimensions in Electrochemistry. *Chemical Society Reviews* 23 (1994) 289–297.
9. Zoski CG. Ultramicroelectrodes: Design, Fabrication, and Characterization. *Electroanalysis* 14 (2002) 1041–1051.
10. Feeney R, Kounaves SP. Microfabricated Ultramicroelectrode Arrays: Developments, Advances, and Applications in Environmental Analysis. *Electroanalysis* 12 (2000) 677–684.
11. Stulik K, Amatore C, Holub K, Maracek V, Kutner W. *Pure and Applied Chemistry* 72 (2000) 1483–1492.
12. Szunerits S, Thouin L. Microelectrode Arrays. In *Handbook of Electrochemistry* ed. Zoski CG, Elsevier, Oxford, Ch. 10 (2007) 391–428.
13. Clark WJ, McCreery RL. Inhibition of Corrosion–Related Reduction Processes via Chromium Monolayer Formation. *Journal of The Electrochemical Society*, 149 (2002) B379–B386.
14. Wehmeyer KR, Wightman RM. Scan Rate Dependence of the Apparent Capacitance at Microvoltammetric Electrodes. *Journal of Electroanalytical Chemistry and Interfacial Electrochemistry* 196 (1985) 417–421.
15. Kovach PM, Deakin MR, Wightman RM. Electrochemistry at Partially Blocked Carbon Fiber Microcylinder Electrodes. *The Journal of Physical Chemistry* 90 (1986) 4612–4617.
16. Hurley BL and McCreery RL. Raman Spectroscopy of Monolayers Formed from Chromate Corrosion Inhibitor on Copper Surfaces. *Journal of The Electrochemical Society* 150 (2003) B367–B373.
17. Ugo P, Moretto LM, Vezza F. Ionomer–Coated Electrodes and Nanoelectrode Ensembles As Electrochemical Environmental Sensors: Recent Advances and Prospects. *Chemphyschem* 3 (2002) 917–925.
18. Penner RM, Martin CR. Preparation and Electrochemical Characterization of Ultramicroelectrode Ensembles. *Analytical Chemistry* 59 (1987) 2625–2630.
19. Menon VP, Martin CR. Fabrication and Evaluation of Nanoelectrode Ensembles. *Analytical Chemistry* 67 (1995) 1920–1928.
20. Hulteen JC, Menon VP, Martin CR. Template Preparation of Nanoelectrode Ensembles. Achieving the ‘pore–radial’ Electrochemical Response Limiting Current. *Journal of Chemical Society–Faraday Transactions* 92 (1996) 4029–4032.
21. Zhang B, Zhang Y, White HS. The Nanopore Electrode. *Analytical Chemistry* 76 (2004) 6229–6238.
22. Zhang B, Zhang Y, White HS. Steady–State Voltammetric Response of the Nanopore Electrode. *Analytical Chemistry* 78 (2006) 477–483.

On Critical Buckling Loads of Euler Columns With Elastic End Restraints

Musa Başbük¹, Aytekin Eryılmaz¹, Safa B. Coşkun² and Mehmet Tarık Atay³

¹ Nevşehir Hacı Bektaş Veli University, Department of Mathematics, Nevşehir, TURKEY

² Kocaeli University, Department of Civil Engineering, Kocaeli, TURKEY

³ Abdullah Gul University, Department of Mechanical Engineering, Kayseri, TURKEY

ABSTRACT

In recent years, a great number of analytical approximate solution techniques have been introduced to find a solution to the nonlinear problems that arised in applied sciences. One of these methods is the homotopy analysis method (HAM). HAM has been successfully applied to various kinds of nonlinear differential equations. In this paper, HAM is applied to find buckling loads of Euler columns with elastic end restraints. The critical buckling loads obtained by using HAM are compared with the exact analytic solutions in the literature. Perfect match of the results veries that HAM can be used as an efficient, powerfull and accurate tool for buckling analysis of Euler columns with elastic end restraints.

Article History:

Received: 2015/11/11

Accepted: 2016/04/18

Online: 2016/06/30

Correspondence to: Aytekin Eryılmaz,
Nevşehir Hacı Bektaş Veli University,
Faculty of Science and Arts, Department
of Mathematics, Nevşehir, TURKEY
Tel: +90 (384) 215 3900/1320
Fax: +90 (384) 2153948
E-Mail: erylilmazaytekin@gmail.com

Key Words:

Homotopy analysis method (HAM); Euler column; Buckling load; Elastic restraint.

INTRODUCTION

Many phenomena in science and engineering involve nonlinear problems. However, the majority of these nonlinear problems have no exact analytical solutions since it is generally dicult to solve nonlinear equations analytically. In recent years, these nonlinear equations have been solved by analytical approximate solution techniques, such as perturbation and nonperturbation techniques. Perturbation techniques usually depend on small/large physical parameters. Although non-perturbation techniques do not depend on small/large physical parameters, these methods cannot ensure the convergence of the solution series. In fact, neither perturbation methods nor nonperturbation techniques can adjust or control the convergence region and the rate of the approximation series. On the other hand, the homotopy analysis method (HAM) which is proposed by Liao [1, 2] is an analytic approach to obtain series solution of various types of linear and nonlinear differential equations, such as ordinary differential equations, partial differential equations, integro-differential equations, difference equations, differential-difference equations, integro-differential difference equations [1, 2, 3, 4, 5, 6] and it provides a convenient way to adjust and control the

convergence region and the rate of the approximation series by an auxiliary parameter \hbar and auxiliary function $H(x)$ [2]. Since HAM is independent of small/large physical parameters, it can be applied to many nonlinear problems whether there exist small/large physical parameters or not. One of the most important advantages of HAM is the freedom to choose the so-called auxiliary operator L , the auxiliary parameter \hbar and auxiliary function $H(x)$, the initial approximations and the set of base functions [1, 2]. One of the important topics of the elds of structural, mechanical and aeronautical engineering has been the stability analysis of the commonly used basic structural elements; namely columns. There are various studies on elastic stability of columns. However, it is not easy to determine exact analytical solutions for many kinds of buckling problems. Many researchers successfully applied analytical approximate solution techniques to stability analysis of uniform and nonuniform Euler columns and beams with various end conditions. Atay and Coskun investigated the elastic stability of homogenous and non-homogenous Euler columns by using variational iteration method and homotopy perturbation method [7, 8, 9, 10, 11, 12, 13]. Pinarbasi

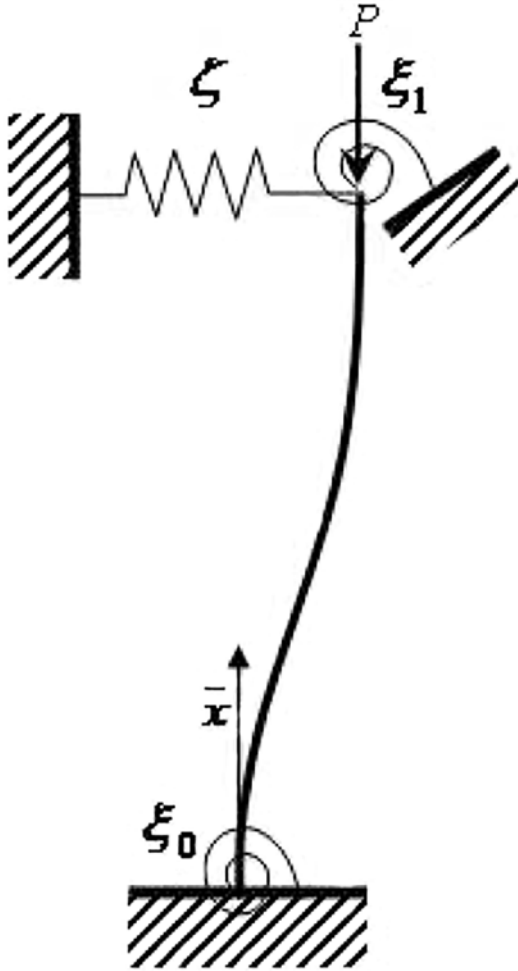


Figure 1. Column with elastic end restraints.

et al. studied on elastic buckling behavior of nonuniform rectangular beams [14, 15], nonuniform columns with elastic end restraints [16] and stepped columns [17, 18] using variational iteration method and homotopy perturbation method. By transforming the governing equation with varying coefficients to linear algebraic equations and by using various end boundary conditions, critical buckling loads of beams with arbitrarily axial inhomogeneity is solved by Huang and Luo [19]. Recently, Yuan and Wang [20] applied a new differential quadrature based iterative numerical integration method to solve post-buckling differential equations of extensible beam-columns with six different cases. By using HAM, Eryilmaz et al. investigated the buckling loads of Euler columns with continuous elastic restraint [21] and Basbuk investigated buckling loads of elastic columns with constant cross-section [22]. These studies showed that HAM has been efficiently used in such stability problems. In this study HAM is used to find the buckling loads of Euler columns with elastic end restraints.

BUCKLING OF ELASTIC COLUMNS

The general case of a uniform column with elastic restraints is shown in Fig. 1. The moment-displacement relation according to the Euler-Bernoulli beam theory is given by

$$M = \frac{d^2 \bar{w}}{dx^2} \quad (2.1)$$

where x is the longitudinal coordinate measured from the column base, w is the transverse displacement and M is the bending moment [23]. Bazant and Cedolin stated the equilibrium equations as follows [24]:

$$\frac{dM}{dx} = Q \quad (2.2)$$

$$\frac{dQ}{dx} = P \frac{d^2 \bar{w}}{dx^2} \quad (2.3)$$

where Q is the shear force normal to the deflected column axis. By substituting equations (1) and (2) into equation (3) yields the following governing Euler column buckling equation:

$$\frac{d^4 \bar{w}}{dx^4} + \alpha \frac{d^2 \bar{w}}{dx^2} = 0, \quad \alpha = \frac{PL^2}{EI} \quad (2.4)$$

where $w = w=L$ and $x = x=L$. The boundary conditions of a column with elastic end restraints has the form,

$$w(0) = 0, \quad (2.5)$$

$$\left[\xi_0 \frac{dw}{dx} - \frac{d^2 w}{dx^2} \right] \Big|_{x=0} = 0, \quad (2.6)$$

$$\left[\xi_1 \frac{dw}{dx} + \frac{d^2 w}{dx^2} \right] \Big|_{x=L} = 0, \quad (2.6)$$

$$\zeta w(1) + \left[\alpha \frac{dw}{dx} + \frac{d^3 w}{dx^3} \right] \Big|_{x=L} = 0, \quad (2.7)$$

where, ξ_0 and ξ_1 represent the rotational spring constants, ζ denotes the translational spring constant against sideways [25].

BASIC IDEA OF HOMOTOPY ANALYSIS METHOD (HAM)

Liao introduced the Homotopy Analysis Method (HAM)

in [1, 2]. To demonstrate the method, let us consider the following differential equation

$$\mathcal{N}[w(x)] = 0 \tag{3.1}$$

where \mathcal{N} is a nonlinear operator, x denotes the independent variable and $w(x)$ is an unknown function. Liao [2] constructs the so-called zero-order deformation equation as follows:

$$(1 - q)\mathcal{L}[\phi(x; q) - w_0(x)] = q\hbar H(x)\mathcal{N}[\phi(x; q)] \tag{3.2}$$

where $q \in [0; 1]$ is the embedding parameter, \hbar is an embedding parameter, $H(x)$ is nonzero auxiliary function, $w_0(x)$ is the initial guess to $w(x)$, \mathcal{L} is an auxiliary linear operator and $(x; q)$ is an unknown function. As q increases from 0 to 1, $(x; q)$ varies from the initial guess $w_0(x)$ to the exact solution $w(x)$. By expanding $(x; q)$ in a Taylor's series with respect to q , one has

$$\phi(x; q) = w_0(x) + \sum_{m=1}^{\infty} w_m(x)q^m, \tag{3.3}$$

$$w_m(x) = \frac{1}{m!} \left. \frac{\partial^m \mathcal{N}[\phi(x; q)]}{\partial q^m} \right|_{q=0}. \tag{3.4}$$

If the initial guess $w_0(x)$, auxiliary linear operator \mathcal{L} , embedding parameter \hbar and auxiliary function $H(x)$ are properly chosen, the series in equation (11) converges at $q = 1$, then we have

$$w(x) = w_0(x) + \sum_{m=1}^{\infty} w_m(x) \tag{3.5}$$

Now, let's define the vector

$$\vec{w}(x) = w_1(x), w_2(x), \dots, w_m(x) \tag{3.6}$$

Differentiating equation (10) m -times with respect to q and then setting $q = 0$ and finally dividing by $m!$, Liao has the so-called m th order deformation equation

$$\mathcal{L}[\phi(x; q) - \chi_m w_{m-1}(x)] = q\hbar \mathcal{H}(x) \mathcal{R}[\vec{w}_{m-1}(x)] \tag{3.7}$$

where

$$\mathcal{R}[\vec{w}_m(x)] = \frac{1}{m!} \left. \frac{\partial^m \mathcal{N}[\phi(x; q)]}{\partial q^m} \right|_{q=0}, \tag{3.8}$$

$$\chi_m = \begin{cases} 1, & m > 1, \\ 0, & \text{else.} \end{cases} \tag{3.9}$$

NUMERICAL RESULTS AND HAM FORMULATION OF THE PROBLEM

Due to the boundary conditions (5)-(8), the rule of solution

$$w_0(x) = ax^3 + bx^2 + cx + d, \tag{4.1}$$

is straightforward to choose

$$\mathcal{L}[\phi(x; q)] = \frac{\partial^4 \mathcal{N}[\phi(x; q)]}{\partial q^4}, \tag{4.2}$$

$$\mathcal{L}[c_0 + c_1x + c_2x^2 + c_3x^3] = 0,$$

with the property

$$\mathcal{L}[c_0 + c_1x + c_2x^2 + c_3x^3] = 0, \tag{4.3}$$

To solve equation (4) by means of homotopy analysis

$$\mathcal{N}[\phi(x; q)] = \frac{\partial^4 \mathcal{N}[\phi(x; q)]}{\partial x^4} + \alpha \frac{\partial^2 \mathcal{N}[\phi(x; q)]}{\partial x^2} \mathcal{N}[\phi(x; q)] \tag{4.4}$$

as follows

$$\mathcal{H}(x) = 1 \tag{4.5}$$

Let \hbar denote a nonzero embedding parameter and

$$(1 - q)\mathcal{L}[\phi(x; q) - w_0(x)] = q\hbar \mathcal{H}(x)\mathcal{N}[\phi(x; q)] \tag{4.6}$$

an auxiliary function. Then, we construct the zero-order deformation equation

$$\mathcal{L}[\phi(x; q) - \chi_m w_{m-1}(x)] = q\hbar \mathcal{H}(x)\mathcal{N}[\phi(x; q)] \tag{4.7}$$

The high order deformation equation is as follows

$$\mathcal{L}[\phi(x; q) - \chi_m w_{m-1}(x)] = q\hbar \mathcal{H}(x)\mathcal{N}[\phi(x; q)] \tag{4.8}$$

$$w_m(x) = \chi_m w_{m-1}(x) + \hbar \int_0^x \int_0^\tau \int_0^\zeta \int_0^\psi [w_{m-1}^{iv}(\xi) + \alpha w_{m-1}''(\xi)] d\xi d\psi d\zeta d\tau \tag{4.8}$$

By substituting equations (19), (21) and (22) into equation (24) the high order deformation equation takes the form where $w^{(4)}$ and w'' denote the fourth and second derivatives with respect to ξ respectively. Starting with initial approximation $w_0(x)$, we successively obtained $w_i(x)$,

$$w(x) = w_0(x) + \sum_{m=1}^{\infty} w_m(x) \quad \text{high-order deformation is of the form} \tag{4.9}$$

Since the governing equation (4) is a fourth order differential equation we choose the initial approximation as $w_0(x) = ax^3 + bx^2 + cx + d$; i.e., a polynomial of third

degree with four unknown coefficients a; b; c; d. Then we

$$W_{10}(x, \hbar) = \sum_{m=0}^{10} w_m(x) = w_0(x) + w_1(x) + \dots + w_{10}(x)$$

obtained $w_i(x)$, $i = 1; 2; 3; \dots$ as follows

After ten iterations, W_{10} is obtained as follows (4.10)

By substituting equation (27) into the boundary conditions, we obtained four homogeneous equations. By representing these equations in the matrix form by

$$[C(\alpha, \xi_0, \xi_1, \zeta, \hbar)] [a \ b \ c \ d]^T = [0 \ 0 \ 0 \ 0]^T$$

coefficient matrix $[C(\alpha, \xi_0, \xi_1, \zeta, \hbar)]$, we obtained the

$$\begin{aligned} w_1(x) &= \frac{1}{12}bx^4\alpha\hbar + \frac{1}{20}ax^5\alpha\hbar \\ w_2(x) &= \frac{1}{12}bx^4\alpha\hbar + \frac{1}{20}ax^5\alpha\hbar + \frac{1}{12}bx^4\alpha\hbar^2 + \frac{1}{20}ax^5\alpha\hbar^2 + \frac{1}{360}bx^6\alpha^2\hbar^2 \\ &\quad + \frac{1}{840}ax^7\alpha^2\hbar^2 \\ w_3(x) &= \frac{1}{12}bx^4\alpha\hbar + \frac{1}{20}ax^5\alpha\hbar + \frac{1}{6}bx^4\alpha\hbar^2 + \frac{1}{10}ax^5\alpha\hbar^2 + \frac{1}{180}bx^6\alpha^2\hbar^2 \\ &\quad + \frac{1}{420}ax^7\alpha^2\hbar^2 + \frac{1}{12}bx^4\alpha\hbar^3 + \frac{1}{20}ax^5\alpha\hbar^3 + \frac{1}{180}bx^6\alpha^2\hbar^3 \\ &\quad + \frac{1}{420}ax^7\alpha^2\hbar^3 + \frac{bx^8\alpha^3\hbar^3}{20160} + \frac{ax^9\alpha^3\hbar^3}{60480} \\ w_4(x) &= \frac{1}{12}bx^4\alpha\hbar + \frac{1}{20}ax^5\alpha\hbar + \frac{1}{4}bx^4\alpha\hbar^2 + \frac{3}{20}ax^5\alpha\hbar^2 + \frac{1}{120}bx^6\alpha^2\hbar^2 \\ &\quad + \frac{1}{280}ax^7\alpha^2\hbar^2 + \frac{1}{4}bx^4\alpha\hbar^3 + \frac{3}{20}ax^5\alpha\hbar^3 + \frac{1}{60}bx^6\alpha^2\hbar^3 + \frac{1}{140}ax^7\alpha^2\hbar^3 \\ &\quad + \frac{bx^8\alpha^3\hbar^3}{6720} + \frac{ax^9\alpha^3\hbar^3}{20160} + \frac{1}{12}bx^4\alpha\hbar^4 + \frac{1}{20}ax^5\alpha\hbar^4 + \frac{1}{120}bx^6\alpha^2\hbar^4 \\ &\quad + \frac{1}{280}ax^7\alpha^2\hbar^4 + \frac{bx^8\alpha^3\hbar^4}{6720} + \frac{ax^9\alpha^3\hbar^4}{20160} + \frac{bx^{10}\alpha^4\hbar^4}{1814400} + \frac{ax^{11}\alpha^4\hbar^4}{6652800} \\ &\quad \vdots \end{aligned} \tag{4.13}$$

following equation:

$$(4.11)$$

where a; b; c and d are the unknown constants of initial approximation $w_0(x)$. For nontrivial solution, the

$$Det[C(\alpha, \xi_0, \xi_1, \zeta, \hbar)] = 0. \text{ matrix } [C(\alpha, \xi_0, \xi_1, \zeta, \hbar)]$$

must vanish. Then, the problem takes the following form (4.12)

The smallest positive real root of the equation (29) is the critical buckling load. The equation (29) depends on the stability parameter the rotational spring constants 120 and 121, the translational spring constant and the

$W(\alpha, \xi_0, \xi_1, \zeta, \hbar) = Det[C(\alpha, \xi_0, \xi_1, \zeta, \hbar)]$ define the function $W(\alpha, \xi_0, \xi_1, \zeta, \hbar)$ as follows:

Then, we plot the \hbar -curves of the $W(\alpha, \xi_0, \xi_1, \zeta, \hbar)$ and

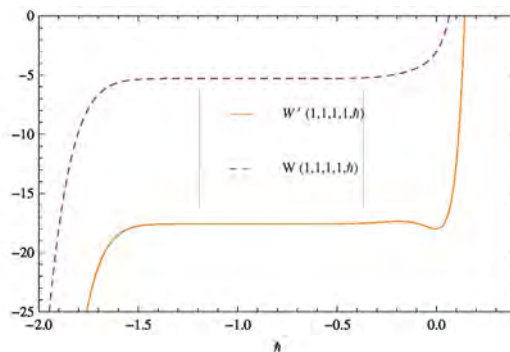


Figure 2. The \hbar curves of \hbar -curves of $W(\alpha, \xi_0, \xi_1, \zeta, \hbar)$ and $W'(\alpha, \xi_0, \xi_1, \zeta, \hbar)$.

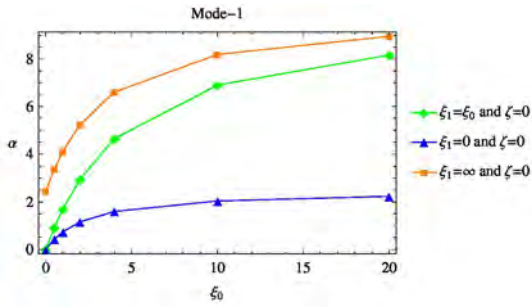


Figure 3. Critical buckling loads for columns with the top end free to slide laterally ($\zeta = 0$) for various values of ξ_0 and ξ_1 .

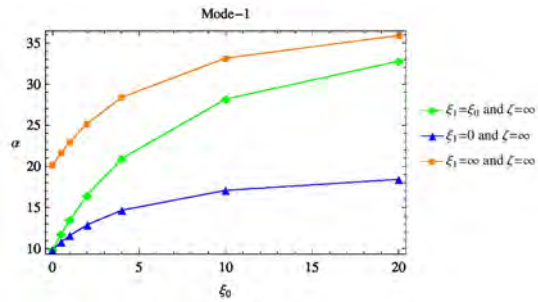


Figure 4. Critical buckling loads for columns with the top end free to slide laterally ($\zeta = \infty$) for various values of ξ_0 and ξ_1 .

$W_0(\alpha, \xi_0, \xi_1, \zeta, \bar{h})$ in order to find the convergence region of \bar{h} . The \bar{h} -curves of $W(\alpha, \xi_0, \xi_1, \zeta, \bar{h})$ and $W_0(\alpha, \xi_0, \xi_1, \zeta, \bar{h})$ are obtained in Figure 2. The valid region of \bar{h} which corresponds to the line segments nearly parallel to the horizontal axis is about $-1.4 < \bar{h} < -0.6$.

Finally the critical buckling loads are obtained from the equation (29) for $\bar{h} = -0.99$. Figure 3 and Figure 4 show the nondimension-alized values of the rst mode buckling loads for columns with the top end free to slide laterally ($\zeta = 0$) and for the columns with only end rotational restraints ($\zeta = 1$) for various values of ξ_0 and ξ_1 , respectively. Table 1. compares HAM solutions with the exact solutions given by Wang et al. [36].

CONCLUSION

In this work, a reliable algorithm based on the homotopy analysis method (HAM) is used to determine the buckling load of Euler columns with elastic end restraints. Several cases are studied to illustrate the validity and accuracy of this procedure. The series solution of equation (4) by HAM contains the auxiliary parameter \bar{h} . By means of the so-called \bar{h} -curve, it is straightforward to choose a proper value of \bar{h} which ensures that the series solution is convergent. Figure 2 shows the \bar{h} -curves obtained from the 10th-order HAM approximation solutions. Figure 3 and Figure 4 show the critical buckling loads for various values of ξ_0 ; ξ_1 and ζ obtained by HAM. The approximate solutions obtained by HAM and the exact solutions given in [25] are compared. The exact match of the results verify that HAM is an efficient, powerful and accurate tool for buckling loads of columns with elastic end restraints.

Table 1. Comparison of critical buckling loads for various values of ξ_0 , ξ_1 , ζ computed from exact [25] and HAM solutions

		ξ_0							
ξ_1		0	0.5	1	2	4	10	20	∞
<i>Columns with only end rotational restraints ($\zeta = \infty$)</i>									
ξ_0	Exact	π^2	11.772	13.492	16.463	20.957	28.168	30.355	$4\pi^2$
	HAM	9.8686	11.772	13.492	16.463	20.957	28.168	32.782	30.478
0	Exact	π^2	10.798	11.598	12.894	14.660	17.076	18.417	20.191
	HAM	9.8688	10.798	11.598	12.894	14.660	17.076	18.417	20.191
∞	Exact	20.191	21.659	22.969	25.182	28.397	33.153	35.902	$4\pi^2$
	HAM	20.191	21.659	22.969	25.182	28.397	33.153	35.902	39.478
<i>Columns with the top end free to slide laterally ($\zeta = 0$)</i>									
ξ_0	Exact	0	0.9220	1.7071	2.9607	4.6386	6.9047	8.1667	π^2
	HAM	0	0.9220	1.7071	2.9607	4.6386	6.9047	8.1667	9.8686
0	Exact	0	0.4268	0.7402	1.1597	1.5992	2.0517	2.2384	$\pi^2/4$
	HAM	0	0.4268	0.7402	1.1597	1.5992	2.0517	2.2384	2.4674
∞	Exact	$\pi^2/4$	3.3731	4.1159	5.2392	6.6071	8.1955	8.9583	π^2
	HAM	2.4674	3.3731	4.1159	5.2392	6.6071	8.1955	8.9583	9.8686

REFERENCES

1. S. Liao, The proposed homotopy analysis technique for the solution of nonlinear problems, Ph.D. thesis, Shanghai Jiao Tong University (1992).
2. S. Liao, Beyond perturbation: introduction to the homotopy analysis method, Chapman and Hall/CRC Press, Boca Raton, 2004, pp. 23–61.
3. M. Basbuk, A. Eryilmaz, The approximate solutions of first order difference equations with constant and variable coefficients, *Sop Transactions On Applied Mathematics* 1 (2014) 1–12.
4. A. Bataineh, M. Noorani, I. Hashim, Solutions of time-dependent Emden–Fowler type equations by homotopy analysis method, *Physics Letters A* 371 (2007) 72–82.
5. S. Karakoc, A. Eryilmaz, M. Basbuk, The approximate solutions of Fredholm integrodifferential–difference equations with variable coefficients via homotopy analysis method, *Mathematical Problems in Engineering* (2013) 2013 1–7.
6. Z. Wang, L. Zou, H. Zhang, Applying homotopy analysis method for solving differential difference equation, *Physics Letters A* 369 (2007) 77–84.
7. M. Atay, S. Coskun, Elastic stability of Euler columns with a continuous elastic restraint using variational iteration method, *Computers and Mathematics with Applications* 58 (2009) 2528–2534.
8. M. Atay, S. Coskun, Determination of buckling loads of tilted buckled column with varying exural rigidity using variational iteration method, *International Journal of Nonlinear Sciences and Numerical Simulation* 11 (2010) 97–103.
9. M. Atay, Determination of critical buckling loads for variable stiffness Euler columns using homotopy perturbation method, *International Journal of Nonlinear Sciences and Numerical Simulation* 10 (2009) 199–206.
10. S. Coskun, M. Atay, Determination of critical buckling load for elastic columns of constant and variable cross-sections using variational iteration method, *Computers and Mathematics with Applications* 58 (2009) 2260–2266.
11. S. Coskun, Determination of critical buckling loads for Euler columns of variable exural stiffness with a continuous elastic restraint using homotopy perturbation method, *International Journal of Nonlinear Sciences and Numerical Simulation* 10 (2009) 191–197.
12. S. Coskun, Analysis of tilt–buckling of Euler columns with varying exural stiffness using homotopy perturbation method, *Mathematical Modelling and Analysis* 15 (2010) 275–286.
13. F. Okay, M. Atay, S. Coskun, Determination of buckling loads and mode shapes of a heavy vertical column under its own weight using the variational iteration method, *International Journal of Nonlinear Sciences and Numerical Simulation* 11 (2010) 851–857.
14. S. Pinarbaşı, Lateral torsional buckling of rectangular beams using variational iteration method, *Lateral torsional buckling of rectangular beams using variational iteration method*, *Scientific Research and Essays* 6 (2011) 1445–1457.
15. S. Pinarbaşı, Stability analysis of nonuniform rectangular beams using homotopy perturbation method, *Mathematical Problems in Engineering* (2012) 2012 1–18.
16. S. Pinarbaşı, Buckling analysis of nonuniform columns with elastic end restraints, *Journal of Mechanics of Materials and Structures* 7 (5) (2012) 485–507.
17. S. Pinarbaşı et al., Analytical, numerical and experimental studies on stability of three segment compression members with pinned ends, in: S. Coskun (Ed.), *Advances in Computational Stability Analysis*, InTech, 2012, pp. 673–9.
18. S. Pinarbaşı et al., Stability analysis of two–segment stepped columns with different end conditions and internal axial loads, *Mathematical Problems in Engineering* 2013 (2013) 1–9.
19. Y. Huang, Q. Luo, A simple method to determine the critical buckling loads for axially inhomogeneous beams with elastic restraint, *Computers and Mathematics with Applications* 61 (2011) 2510–2517.
20. Z.X. Yuan, X.W. Wang, Buckling and post–buckling analysis of extensible beam–columns by using the differential quadrature method, *Computers and Mathematics with Applications* 62 (2011) 4499–4513.
21. A. Eryilmaz et al., Buckling of Euler columns with a continuous elastic restraint via homotopy analysis method, *Journal of Applied Mathematics* 2013 (2013) 1–8.
22. M. Basbuk, M. Atay, A. Eryilmaz, Numerical solutions for buckling loads of elastic columns with constant cross-section, *Transaction on IoT and Cloud Computing* 2 (2014) 1–13.
23. J. Reddy, *Energy Principles and Variational Methods in Applied Mechanics*, John–Wiley, New York, 2002.
24. Z. Bazant, L. Cedolin, *Stability of Structures: Elastic, Inelastic Fracture and Damage Theories*, World Scientific Publishing, Singapore, 2010.
25. C.M. Wang, C.Y. Wang, J.N. Reddy, *Exact Solutions for Buckling of Structural Members*, CRC Press, Florida, 2005, pp. 22–24.

Synthesis and Thermal Characterization of *p*-Coumaric Acid Complexes of Co^{II}, Ni^{II}, Cu^{II} and Zn^{II} Metal Cations and Biological Applications

Sineray Koç¹, Dursun Ali Köse¹, Emre Avcı², Kazım Köse³

¹ Hitit University, Department of Chemistry, Corum, TURKEY

² Hitit University, Department of Molecular Biology and Genetics, Ulukavak, Corum, TURKEY

³ Hitit University, Scientific Technical Research and Application Center, Corum, TURKEY

ABSTRACT

The phenolic compound used in this study is *p*-coumaric acid, which is the derivative of phenolic acid playing a role in giving color, odor and taste to the plants. The *p*-coumaric acid is an organic compound derived from cinnamic acid. There are three isomers of this structure as ortho-, meta- and para- depending on the location of the hydroxyl group within the structure. In this study, metal complexes of *p*-coumaric acid ligand with the transition metal cations (Co^{II}, Ni^{II}, Cu^{II}, Zn^{II}) were synthesized. The structure of the synthesized complexes was studied via elemental analysis, infrared and ultraviolet-visible spectroscopy, magnetic measurements, melting point and thermal analysis. Furthermore the biological properties of these new molecules were studied.

Article History:

Received: 2015/11/17

Accepted: 2016/01/15

Online: 2016/06/30

Correspondence to: Dursun Ali Kose,
Hitit University, Faculty of Science and
Arts, Department of Chemistry, Corum,
TURKEY

Tel: +90 (364) 2277000/1635

Fax: +90 (364) 2277005

E-Mail: dalikose@hitit.edu.tr

Key Words:

p-coumaric Acid; Metal Complexes; Thermal Analysis; Spectroscopy; Biological Activity.

INTRODUCTION

Phenolic compounds or polyphenols are the chemical compounds with the hydroxyl bounded benzene ring, which exist in large amounts in plants, give color to fruits and flowers and provide protection against environmental stress [1-3]

Phenolic substances constitute the most important group of natural antioxidants. These substances are common in plant foods such as fruits, vegetables, spices, cereals and drinks. In addition, they are also known as free radical scavenger and chain breakers [4,5].

The antioxidant effects of the phenolic compounds comes from the resonance stability of phenol radical and from features such as scavenging free-radicals, forming compounds with metal ions (metal chelating) and preventing or reducing the formation of singlet (radical) oxygen. These compounds are capable of releasing hydrogen of hydroxyl groups in the aromatic rings present in the structure to prevent the oxidation of lipids and other

biomolecules (e.g. proteins, carbohydrates, nucleic acids) by free radicals [6-8]. Antioxidants convert chain-forming radicals into less reactive species by acting as a hydrogen atom transmitter. The antioxidant radical formed in this way is stabilized by displacing the oxygen atom with unpaired electrons on the aromatic ring. Therefore, the molecules with the antioxidant feature often carry a functional phenolic group in the structure [9-12].

These compounds are also called flavonoids. They have positive effects on nutrition physiology, regulate the permeability of the capillary circulatory system and lower blood pressure [13].

The subject in this study was *p*-coumaric acid within the group of phenolic acids giving color, odor and taste to the plants. The *p*-coumaric acid is a phenolic compound derived from cinnamic acid has three isomers depending on the bonding position of the hydroxyl group in the structure as ortho-, para- and meta- has the molecular formula of C₉H₈O₃ and

the molecular weight of 164.15 g.mol⁻¹, has melting point of 210-213°C. Exists much in orange [14], cherry, coffee, chocolate and wine [15]. The ability to kill tumor cells, the oxidative damage of p-coumaric acid on DNA was reported. It shows the toxic effects when taken in high amounts [16]. It is also known that the p-coumaric acid is particularly effective against gastric cancer [17].

P-coumaric acid has the capability to fight against antibacteria, antifungal and also parasites [18]. The p-coumaric acid the most important derivatives of the cinnamic acid is among the notable pharmaceuticals with the properties such as reducing high blood pressure, preventing stroke (antiaggregant) and being an anti-tumor agent [19].

The structural characterization of p-coumaric acid complexes with transition metals such as lanthanum [20], europium [21], cerium [22], zinc [23], manganese [24],

(Cu(NO₃)₂·3H₂O), zinc (II) nitrate heptahydrate (ZnSO₄·7H₂O), sodium bicarbonate (NaHCO₃) and p-coumaric acid, all bought from Sigma-Aldrich, were used.

As the first step in the synthesis of the complexes, p-coumaric acid and sodium bicarbonate, 0.02 moles each, were dissolved separately in the medium of 50:50 (v/v) EtOH:H₂O and reacted with each other. The reaction medium was stirred continuously up to all carbon dioxide formed during the reaction fully removed from the environment. Related metal salts were added on the sodium p-coumarate salt remaining purely in the solution media in the ratio of 1:2 mole (metal: ligand) and stirred on a hot plate at 60°C to obtain clear solution. The solution obtained at the end of the process was kept at reflux for about a day at 75°C. The samples were allowed to crystallize at room temperature for 3 to 6 weeks, and filtered after crystallization to dry at the same condition.

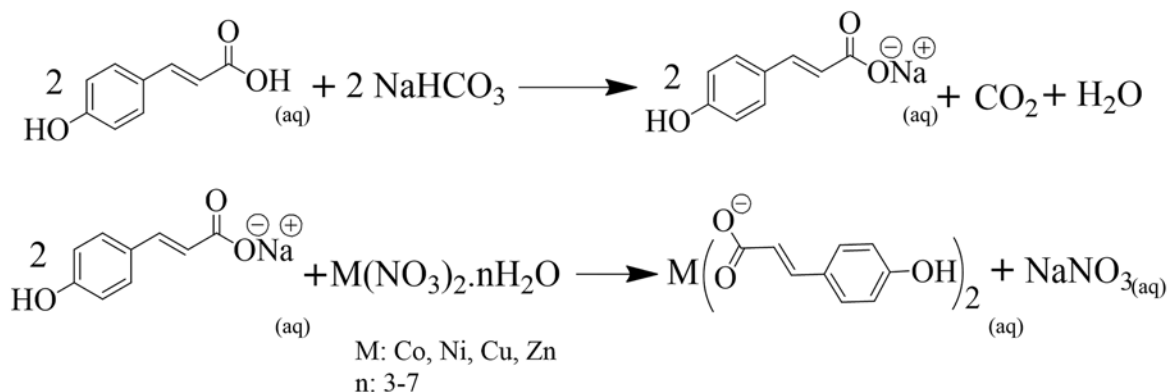


Figure 1. Synthesis reaction.

copper [24] and cadmium [24,25] and various chemical and physicochemical properties with alkali metals (Li, Na, K, Rb) [26] were studied in the literature.

In this study, metal complexes of p-coumaric acid ligand with the transition metal cations (CoII, NiII, CuII, ZnII) were synthesized. The structure of the synthesized complexes was studied via elemental analysis, infrared and ultraviolet-visible spectroscopy, magnetic measurements, melting point and thermal analysis. Furthermore the biological properties of these new molecules were studied.

MATERIAL AND METHOD

Synthesis

In the synthesis of complexes, cobalt (II) nitrate hexahydrate (Co(NO₃)₂·6H₂O), nickel (II) nitrate hexahydrate (NiSO₄·6H₂O), copper (II) nitrate trihydrate

Synthesis reaction was shown in Figure 1.

Determination of Antimicrobial and Total Antioxidant Capacity

Escherichia coli (ATCC 25922), *Staphylococcus aureus* (ATCC 25923), *Enterococcus faecalis* (ATCC 29212), *Pseudomonas aeruginosa* (ATCC 27853), *Candida albicans* (ATCC 10231) were used as test microorganisms. All strains were obtained from the culture collection at Hitit University, Faculty of Science and Arts, Department of Molecular Biology and Genetics, Molecular Microbiology and Biotechnology Research Laboratory. The antimicrobial activities were evaluated by disc-diffusion method. The total antioxidant capacity (TAC) was determined using an automated colorimetric measurement method.

RESULTS AND DISCUSSION

In this study, metal complexes of p-coumaric acid ligand

Table 1. The elemental analysis data of complexes.

Complex	MW g/mol	Yield	Contents % Found (calc.)		Color	d.p. °C	μ_{eff} BM
			C	H			
$[\text{Co}(\text{C}_9\text{H}_7\text{O}_2)_2(\text{H}_2\text{O})_2]\text{H}_2\text{O}$ $\text{C}_{26}\text{H}_{20}\text{CoO}_9$	439.28	91	49,84 (49,22)	5,32 (4,59)	pink	186	3,77
$[\text{Ni}(\text{C}_9\text{H}_7\text{O}_2)_2(\text{H}_2\text{O})_2]2\text{H}_2\text{O}$ $\text{C}_{38}\text{H}_{32}\text{NiO}_{10}$	457.05	87	48,11 (47,30)	4,17 (4,85)	green	191 decomp	2,65
$[\text{Cu}(\text{C}_9\text{H}_7\text{O}_2)_2(\text{H}_2\text{O})_2]$ $\text{C}_{26}\text{H}_{20}\text{CuO}_9$	425,88	93	51,63 (50,76)	4,57 (4,26)	blue	189	1,62
$[\text{Zn}(\text{C}_9\text{H}_7\text{O}_2)_2(\text{H}_2\text{O})_2]\text{H}_2\text{O}$ $\text{C}_{26}\text{H}_{20}\text{ZnO}_9$	445.73	81	49,13 (48,50)	3,97 (4,52)	white	186	Dia.

with the transition metal cations (Co^{II} , Ni^{II} , Cu^{II} , Zn^{II}) were synthesized. The structure of the complexes synthesized was studied via the elemental analysis, infrared and ultraviolet-visible spectroscopy, magnetic measurements, melting point and thermal analysis. Theoretical and experimental results summarized in Table 1 showing chemical composition analysis are consistent with each other. Magnetic susceptibilities of complexes in terms of the Bohr Magneton are also consistent with octahedral structures [27].

Infrared Spectroscopy

The infrared spectra of complexes recorded at 450-4000 cm^{-1} is given in Figure 2. For *p*-coumaric acid, the strong and broadband at 3000-2900 cm^{-1} corresponds to -OH group, in the same way the other spectra data obtained can be given as; C=O group originating from carboxylic acid at 1688 cm^{-1} , supportive C-O peaks at 1260-1100 cm^{-1} and the aromatic C-H stretching at 2879 cm^{-1} . In addition, the peak at 973 cm^{-1} refers to the -OH substituent at the para position. The strong and the broad band obtained at 3600-3000 cm^{-1} for the complexes obtained is originating from -OH group of water included in the structure. In our complex, there are stretching vibrations at 2590 and 2860 cm^{-1} corresponding aromatic C-H bands. The C=O group originating from carboxylic acid in Co^{II} , Ni^{II} , Cu^{II} and Zn^{II} metal complexes gives valence vibrations at 1635, 1632, 1613 and 1638 cm^{-1} , respectively. The asymmetric and symmetric absorption bands of COO^- in carboxylic acid correspond to stretching vibration at 1505-1515 cm^{-1} and 1385-1398 cm^{-1} . The absorption bands corresponding to the M-O bindings underlying the complex have stretching vibrations at 510 and 531 cm^{-1} for Co^{II} complex; at 514 and 535 cm^{-1} for Ni^{II} complex; at 499 and 571 cm^{-1} for Cu^{II} complex; at 515 and 533 cm^{-1} for Zn^{II} complex. Some stretching and bending vibrations of the complexes are summarized in Table 2.

Thermal Analysis

It can be determined from the differential thermogravimetric (DTG) analysis of the complexes between Co^{II} and *p*-coumaric acid ligand that

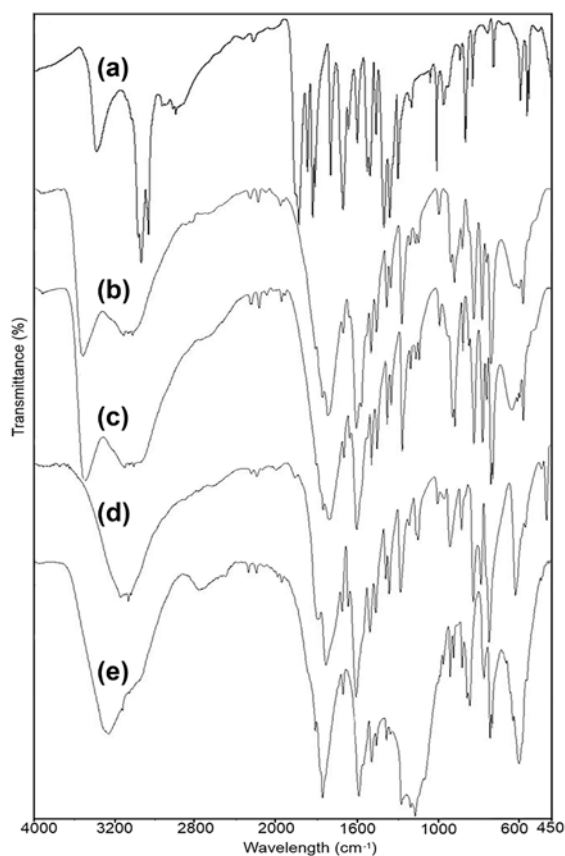
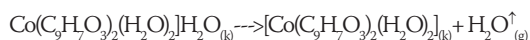


Figure 2. The infrared spectra of *p*-coumaric acid (a) and Co^{II} (b), Ni^{II} (c), Cu^{II} (d) ve Zn^{II} (e) complexes.

it decomposes at four stages corresponding to maximum temperatures of 58, 84, 228, 314°C. The first decomposition step is the removal of 1 mole of crystal water from the structure.



It is the complete removal of 2 moles of water molecules of ligand within the coordination sphere from the structure at the decomposition step of 84°C within the temperature range of 79-152°C.

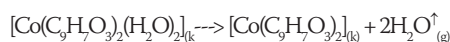


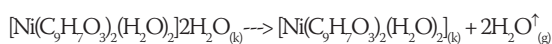
Table 2. The infrared spectra peaks of complexes containing *p*-coumaric acid.

Groups	<i>p</i> -coumaric acid	Co ^{II}	Ni ^{II}	Cu ^{II}	Zn ^{II}
$\nu(-OH)_{H_2O}$	-	3600-3000	3600-3000	3600-3000	3600-2900
$\nu(-OH)_{carboxyl}$	3000-2900	-	-	-	-
$\nu(CH_2)$	2879,2685	2830,2665	2812,2611	2860,2591	2808,2698
$\nu(C=O)_{carboxyl}$	1688	1635	1632	1613	1638
$\nu(COO)_{asym.}$	-	1513	1515	1505	1511
$\nu(COO)_{sym.}$	-	1385	1396	1398	1385
$\Delta\nu_{asym-sym}$	-	128	119	107	126
$\nu(C-C)_{ring}$	1597,1478	1562,1437	1552,1444	1577,1475	1545,1450
$\nu(C-O)_{carboxyl}$	1260-1100	1244-936	1247-953	1261-947	1246-940
$\delta(-OH)_{carboxyl}$	973	-	-	-	-
$\nu(M-O)_{carboxyl}$	-	510,531	514,535	499,571	515,533

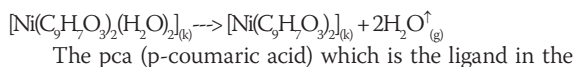
The pca (*p*-coumaric acid) which is the ligand in the complex was removed from the medium by decomposing at the temperature range of 155-385°C. The black colored compound of CoO was remained as the decomposition products.



It can be determined from the DTG curve of the complexes between Ni^{II} and *p*-coumaric acid ligand that it decomposes at four stages corresponding to maximum temperatures of 76, 139, 219 and 398; 775°C. The first decomposition step is the removal of 2 moles of crystal water from the structure.



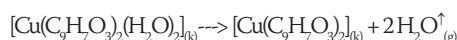
It is the complete removal of 2 moles of aqua ligand within the coordination sphere from the structure at the decomposition step of 139°C within the temperature range of 130-162°C.



complex was removed from the medium by decomposing at the temperature range of 164-790°C. The black colored compound of NiO was remained as the decomposition products.



It can be determined from the DTG curve of the (VII) complexes between Cu^{II} and *p*-coumaric acid ligand that it decomposes at three stages corresponding to maximum temperatures of 83, 223; 260, 856°C. The first decomposition step is the removal of 2 moles of ligand water from the structure.



The pca (*p*-coumaric acid) which is the ligand in the complex was removed from the medium by decomposing at the temperature range of 138-871°C. The black colored compound of CuO was remained as the decomposition products.

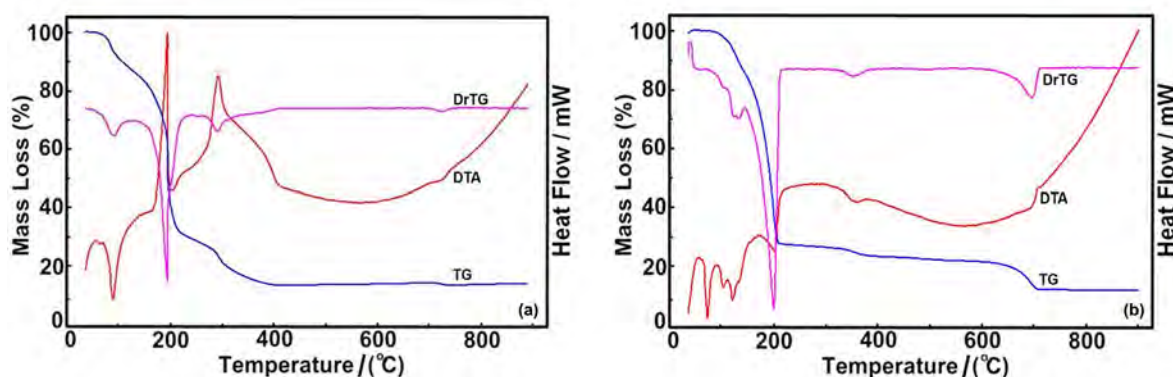
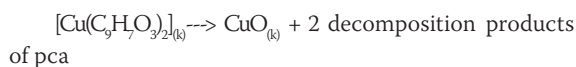


Figure 3. The thermal analysis curves for the complexes of (a) Co^{II} and (b) Ni^{II}.

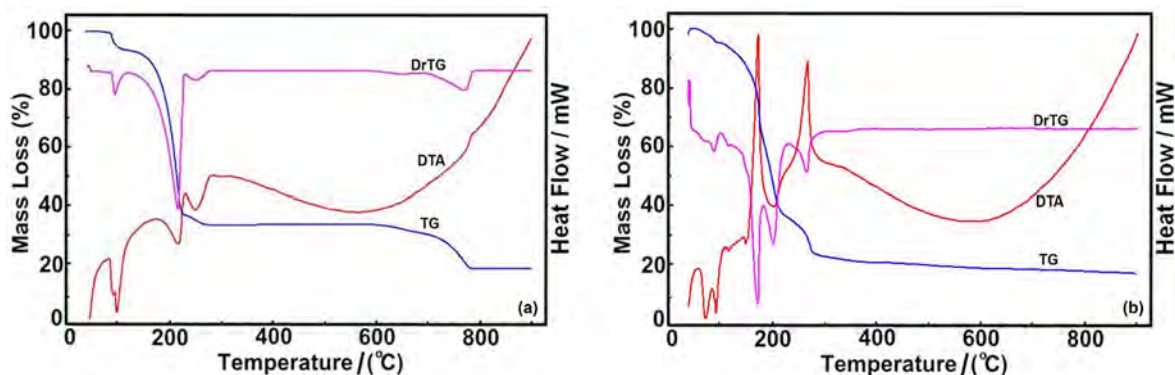
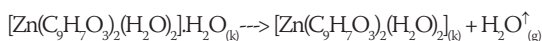
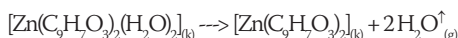


Figure 4. The thermal analysis curves for the complexes of (a) Cu^{II} and (b) Zn^{II}.

It can be determined from the DTG curve of the (VIII) complexes between Zn^{II} and p-coumaric acid ligand that it decomposes at four stages corresponding to maximum temperatures of 62; 86, 113; 150, 178, 285°C. The first decomposition step is the removal of 1 mole of crystal water from the structure.



It is the complete removal of 2 moles of aqua ligand within the coordination sphere from the structure at the decomposition step of 113; 150°C within the temperature range of 91-152°C.



The pca (p-coumaric acid) which is the ligand in the complex was removed from the medium by decomposing at the temperature range of 153-442°C. The grey colored compound of ZnO was remained as the decomposition products.



Complex decomposition steps and decomposition products are summarized in detail in Table 3.

Solid-State UV-vis Spectroscopy

The electronic transition values of complexes obtained according to the visible region spectroscopy (UV-vis)

Table 3. The thermal analysis data for complexes with the ligand of p-coumaric acid.

Complex	Temp. Range(°C)	DTA _{max} (°C)	Leaving Group	Mass Loss(%)		Remnant(%)		Decomp. Prod.	Color
				Exp.	Theoretical	Exp.	Theoretical		
<i>[Co(C₉H₇O₃)₂(H₂O)₂] · H₂O</i>									
439,28 g/mole	1	47-78	58	H ₂ O _(hydrate)	4.09	4.20			Pink
	2	79-152	84	2H ₂ O _(crystal)	8.41	8.40			
	3	155-262	228	2C ₈ H ₈ O	55.12	54.22			
	4	265-385	314	2CO	11.82	12.76	16.33	15.74	
<i>[Ni(C₉H₇O₃)₂(H₂O)₂] · 2H₂O</i>									
457,05 g/mole	1	55-127	76	2H ₂ O _(hydrate)	6.93	7.88			Green
	2	130-162	139	2H ₂ O _(crystal)	8.26	7.88			
	3	164-253	219	2C ₈ H ₈ O	53.63	52.08			
	4	331-790	398;775	2CO	12.63	12.25	16.97	16.35	
<i>[Cu(C₉H₇O₃)₂(H₂O)₂]</i>									
425,88 g/mole	1	70-136	83	2H ₂ O _(hydrate)	4.62	4.23			Blue
	2	138-290	223;260	2C ₈ H ₈ O	57.31	56.33			
	3	660-871	856	2CO	12.98	13.15	19.12	18.66	
<i>[Zn(C₉H₇O₃)₂(H₂O)₂] · H₂O</i>									
445,73 g/mole	1	52-90	62;86	H ₂ O _(hydrate)	4.32	4.22			White
	2	91-152	113;150	2H ₂ O _(crystal)	8.51	8.41			
	3	153-255	178	2C ₈ H ₈ O	54.12	55.61			
	4	256-442	285	2CO	12.50	13.01	20.12	19.02	

Table 4. The *in vitro* antimicrobial activity of complexes synthesized.

Complexes	Strains (Inhibition zones \pm SD)				
	<i>S. aureus</i> ATCC 25923	<i>E. faecalis</i> ATCC 29212	<i>E. coli</i> ATCC 25922	<i>P. aeruginosa</i> ATCC 27853	<i>C. albicans</i> ATCC 10231
<i>p</i> -coumaric acid					
+Co	-	-	-	-	9,0 \pm 1,0
+Ni	-	-	-	-	11,5 \pm 0,5
+Cu	-	-	7,5 \pm 0,5	8,0 \pm 2,0	10,0 \pm 0,1
+Zn	-	-	11,0 \pm 1,0	10,5 \pm 1,5	11,5 \pm 0,5

(*: no inhibition, the amount of complex used: 25 μ L)

of compounds recorded in the interval of 900-200 nm were deduced from the spectral pattern (Figures 4.23 - 4.26). According to these data; d-d transitions could be related to the Co^{II} (V) complexes that were observed at the wavelength of 564.12 nm (⁴T_{1g} → ⁴T_{2g}) (F) and 509.61 nm (⁴T_{1g} → ⁴T_{1g}) (P) (Figure 4.23). The three spin-allowed *d-d* transition belonging to the Ni^{II} (VI) complex were corresponded to the wavelengths of 836.35 nm (³A_{2g} → ³T_{1g}) (P), 641.24 nm (³A_{2g} → ³T_{1g}) (F) and 397.72 nm (³A_{2g} → ³T_{2g}) (F). Therefore, these transition bands confirmed the splitting of *d* orbitals of Ni²⁺ metal cation supporting the octahedral (Figure 4.24). The multiple absorption bands of Cu^{II} (VII) are formed by overlapping peaks and had a broaden shape in a wide range corresponding to the interval of 837.95 - 527.37 nm (Figure 4.25). In the light of these spectral data, it can be thought that Cu²⁺ metal cation confirms “pseudo-octahedral” structure under the influence of the Jahn-Teller effect. The maximum adsorption band of broaden spectrum owned by Cu^{II} (VII) complex corresponded to the wavelength of approximately 677.49 nm (²E_g → ²T_{2g}) [28,29]. There was no any *d-d* electronic transition for an octahedral splitting possible to occur because fully occupied *d* orbitals in the last orbit of Zn^{II} (VIII) complex with the diamagnetic feature as seen from the magnetic susceptibility data (Figure 5) [30-32].

Biologic Applications

The antimicrobial activity and the total antioxidant activity (TAA) of the complexes synthesized are given in Table 4 and 5 respectively.

The antioxidant activity of metal complexes were shown in Table 5. Although the antioxidant values were found to very close to each other, Co^{II} containing molecule has the lowest and the Zn^{II} containing molecules had the highest value. In the case of evaluation of the antimicrobial activities of the complexes (Table 4), it was determined that the most effective metal is zinc. In addition, the metal complexes were found to be effective especially on yeasts and gram negative bacteria according to the inhibition zones obtained for the complexes between transition metal cations (Co^{II}, Ni^{II}, Cu^{II}, Zn^{II}) and *p*-coumaric acid, especially

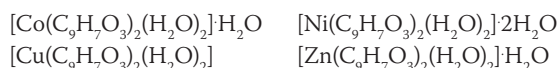
Table 5. The total antioxidant activity results of complexes synthesized.

Metal Complexes	Total Antioxidant Values (mmol Trolox Eq./L)
Co ^{II} (V) complex	0,79
Ni ^{II} (VI) complex	0,84
Cu ^{II} (VII) complex	0,81
Zn ^{II} (VIII) complex	0,89

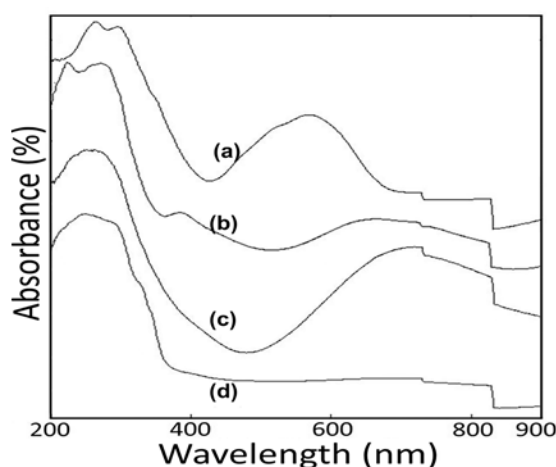
yeasts and gram-negative bacteria appears to be effective.

CONCLUSION

It was determined as a result of the elemental analysis of the complexes synthesized that the metal: ligand ratio was 1:2 for single ligand and 1:2:2 for multi ligand complexes. According to the elemental analysis results (Table 1), the formula of the complexes were determined to be as follows.



It is estimated that the complexes have metal cation coordination sphere in the shape of octahedral geometry. The complexes obtained from transition metal cations of Co^{II}, Ni^{II}, Cu^{II} and Zn^{II} synthesized have the infrared spectrum (Table

**Figure 5.** The UV-vis spectrum of [Zn(C₉H₇O₃)₂(H₂O)₂] \cdot H₂O complex.

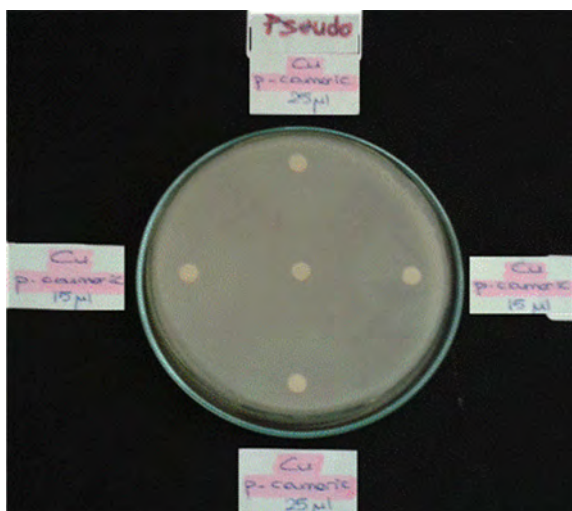


Figure 6. The effect of the Cu^{II} (VII) complex on some microorganisms.

2) in concordance with the binding model proposed in this study. It was determined from symmetric and asymmetric stretching vibrations of carboxylic acid that the binding of p-coumaric acid providing the charge balance of complexes is monoanionic bidentate binding [29,33]. The differences between the symmetric and asymmetric stretching vibrations of the COO⁻ group were obtained as 128 cm⁻¹ for Co^{II}, 119 cm⁻¹ for Ni^{II}, 107 cm⁻¹ for Cu^{II} and 128 cm⁻¹ for Zn^{II} complexes. The differences between symmetric and asymmetric stretching vibrations belonging to the COO⁻ group of p-coumaric acid sodium salt is 145 cm⁻¹ and thus the binding is monoanionic bidentate for the p-coumaric acid containing transition metal complexes.

The estimated structural formula of the complexes, with respect to the results of analysis and similar metal complexes stated previously in the literature [11,29] was proposed as follows:

ACKNOWLEDGEMENTS

We are thankful to Assoc. Prof. Gulcin ALP AVCI of Hitit University for cultivation of bacteria used in

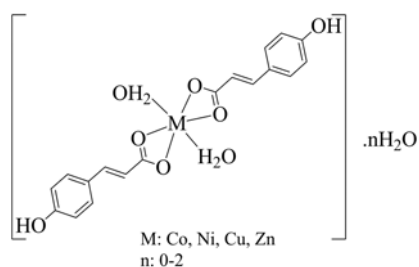


Figure 8. The expected structural formula of complexes.

this study. This research was supported by the Science Research Department of Hitit University (Project no: FEF.19004.13.002).

REFERENCES

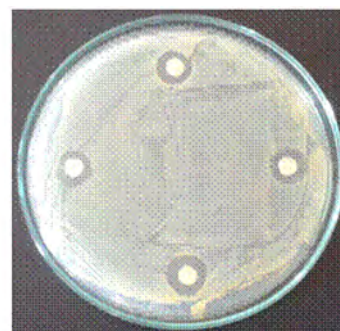
1. Balasundram N, Sundram K, Samman S. Phenolic compounds in plants and agriindustrial by-products: Antioxidant activity, occurrence, and potential uses. *Food Chemistry*, 99 (2006) 191-203.
2. Swiśtocka R, Kowczyk-Sadowy M, Kalinowska M and Lewandowski W. Spectroscopic (FT-IR, FT-Raman, ¹H and ¹³C-NMR) and theoretical studies of p-coumaric acid and alkali metal p-coumarates. *Spectroscopy* 27 (2012) 35-48.
3. Kalinowska M, Swiśtocka R and Lewandowski W. *Journal of Molecular Structure* 834-836 (2007) 572-580.
4. Salameh D, Brandam C, Medawar W, Lteif R and Strehaiano P. *Food Chemistry* 107 (2008) 1661-1667.
5. Nizamlioğlu NM, Nas S. The Phenolic Compounds in Vegetables and Fruit; Structures and Their Importance. *Electronic Journal of Food Technologies* 5(1) (2010) 20-35.
6. Halvorsen BL, Holte K, Myhrstad MC, Barikmo I, Hvattum E, Remberg SF, Wold AB, Haffner K, Baugerød H, Andersen LF, Moskaug Ø, Jacobs DR Jr, Blomhoff R. A systematic screening of total antioxidants in dietary plants. *The Journal of Nutrition* 132(3) (2002) 461-471.
7. Cotellet N, Bernier JL, Catteau JP, Pommery J, Wallet JC, Gaydou EM. Antioxidant properties of hydroxy-flavones. *Free Radical Biology and Medicine* 20(1) (1996) 35-43.
8. Maure A, Cruz JM, Franco D, Dominguez M, Sineiro J, Nunez MJ, Parajo JC. Natural antioxidants from residual sources. *Food Chemistry* 72 (2001) 145-171.



Candida albicans



P.aeruginosa



S.aureus

Figure 7. The effect of the Zn^{II} (IV) complex on some microorganisms

9. Jayaprakasha GK, Selvi T, Sakariah KK. Antibacterial and antioxidant activities of grape (*Vitis vinifera*) seed extracts. *Food Research International* 36 (2003) 117-122.
10. Nandita S, Rajini PS. Free radical scavenging activity of an aqueous extract of potato peel. *Food Chemistry* 85 (2004) 611-616.
11. Köse DA, Öztürk B, Şahin O, Büyükgüngör O. Mixed ligand complexes of coumarilic acid/nicotinamide with transition metal complexes. Synthesis and structural investigation. *Journal of Thermal Analysis and Calorimetry* 115(2) (2014) 1515-1524.
12. Rice-Evans C, Miller NJ, Paganga G. Structure-antioxidant activity relationships of flavonoids and phenolic acids. *Free Radical Biology & Medicine* 20 (1996) 933-956.
13. Moline J, Bukharovich IF, Wolff MS, Phillips R. Dietary flavonoids and hypertension: is there a link? *Medical Hypotheses* 55(4) (2000) 306-309.
14. Sousa WR, Rocha C, Cardoso CL, Silva DHS, Zanoni MVB. Determination of the relative contribution of phenolic antioxidants in orange juice by voltammetric methods. *Journal of Food Composition and Analysis* 17 (2004) 619-633.
15. Abdel-Kader MS. New ester and furocoumarins from the roots of *Pituranthos tortuosus*. *Journal of Chemical Education*, 14(1) (2003) 48-51.
16. Labieniec M, Gabryelak T, Falcioni G. Antioxidant and pro-oxidant effects of Tannins in digestive cells of the freshwater mussel *unio tumidus*. *Mutation Research Genetic Toxicology and Environmental Mutagenesis* 539 (2003) 19-28.
17. Kong CS, Jeong CH, Choi JS, Kim KJ, Jeong JW. Antiangiogenic effects of p-coumaric acid in human endothelial cells. *Phytotherapy Research* 27(3) (2013) 317-23.
18. Burt S. Essential oils: their antibacterial properties and potential applications in foods—a review. *International Journal of Food Microbiology* 94 (2004) 223-253.
19. Hertog MG, Kromhout D, Aravanis C, Blackburn H, Buzina R, Fidanza F, Giampaoli S, Jansen A, Menotti A, Nedeljkovic S. Flavonoid intake and long-term risk of coronary heart disease and cancer in the seven countries study. *Archives of Internal Medicine* 155 (1995) 381-386.
20. Hui Li, Chang Wen Hu. Novel one-dimensional lanthanide acrylic acid complexes: an alternative chain constructed by hydrogen bonding. *Journal of Solid State Chemistry* 177 (2004) 4501-4507.
21. Yan J, Guo Y, Li H, Sun X, Wang Z. Structural diversity and luminescent properties of europium(III) complexes with acrylic acid ligands. *Journal of Molecular Structure* 891 (2008) 298-304.
22. Deacon GB, Forsyth M, Junk PC, Leary SG, Lee WW. Synthesis and Characterisation of Rare Earth Complexes Supported by para-Substituted Cinnamate Ligands. *Zeitschrift für anorganische und allgemeine Chemie* 635 (2009) 833-839.
23. Biswick T, Park DH, Shul YG, Choy JH. P-coumaric acid-zinc basic salt nanohybrid for controlled release and sustained anti oxidant activity. *Journal of Physics and Chemistry of Solids* 71 (2010) 647-649.
24. Jia-Yuan Mao, Hong-Xin Fang, Qing-Feng Xu, Qiu-Xuan Zhou, Jian-Mei Lu, Zhang Y. Synthesis and structural characterization of complexes $[Cd(hca)_2(H_2O)_3] \cdot 2H_2O$ and $[Cu(hca)_2(phen)]$. *Chinese Journal of Inorganic Chemistry* 7 (2008) 1046-1050.
25. Kalinowska M, Laderiere B, Champagne P, Kowczyk-Sadowy M, Lewandowski W. Mn(II), Cu(II) and Cd(II) p-coumarates: FT-IR, FT-Raman, 1H and ^{13}C NMR and thermogravimetric studies. *Spectrochimica Acta Part A: Molecular and Biomolecular Spectroscopy* 103 (2013) 264-271.
26. Lewandowski W, Kalinowska M, Lewandowska H. The influence of metals on the electronic system of biologically important ligands. Spectroscopic study of benzoates, salicylates, nicotinate and isoorotates. *Journal of Inorganic Biochemistry* 99 (2005) 1407-1423.
27. Köse DA, Necefoğlu H, İçbudak H. Synthesis and characterization of N,N-diethylnicotinamide-acetylsalicylate complexes of Co(II), Ni(II), Cu(II) and Zn(II). *Journal of Coordination Chemistry* 61(21) (2008) 3508-3515.
28. Köse DA, Kaya A, Necefoğlu H. Synthesis and characterization of bis(N,N-Diethylnicotinamide) m-hydroxybenzoate complexes of Co(II), Ni(II), Cu(II) and Zn(II). *Russian Journal of Coordination Chemistry* 33(6) (2007) 422-427.
29. Köse DA, Necefoğlu H. Synthesis and characterization of bis(Nicotinamide) m-hydroxybenzoate complexes of Co(II), Ni(II), Cu(II) and Zn(II). *Journal of Thermal Analysis and Calorimetry* 93(2) (2008) 509-514.
30. Mihaylov Tz, Trendafilova N, Kostova I, Georgieva I, Bauer G. DFT modeling and spectroscopic study of metal-ligand bonding in La(III) complex of coumarin-3-carboxylic acid. *Chemical Physics*, 327 (2006) 209-219.
31. Patil SA, Unki SN, Kulkarni AD, Naik VH, Badami PS. Co(II), Ni(II) and Cu(II) complexes with coumarin-8-yl Schiff-bases: Spectroscopic, in vitro antimicrobial, DNA cleavage and fluorescence studies. *Spectrochimica Acta Part A: Molecular and Biomolecular Spectroscopy* 79 (2011) 1128-1136.
32. Köse DA, Necefoğlu H, Şahin O, Büyükgüngör O. Synthesis, structural, spectroscopic characterization and structural comparison of 3-hydroxybenzoate and nicotinamide/ N,N-diethylnicotinamide mixed ligand complexes with Zn(II). *Journal of Thermal Analysis and Calorimetry*, 110(3) (2012) 1233-1241.
33. Nakamoto K. (2009) *Infrared and Raman Spectra of Inorganic and Coordination Compounds, Part B, Applications in Coordination, Organometallic, and Bioinorganic Chemistry*. Wiley, ISBN: 978-0-471-74493-1.

Optimized Rearrangements of Turkish Q and F Keyboards by Means of Language-Statistics and Simple Heuristics

Asım Egemen Yılmaz and Emrah Çiçek

Ankara University, Department of Electrical and Electronics Engineering, Ankara, TURKEY

ABSTRACT

In this study, based on the language (particularly n-gram) statistics of Turkish extracted from a large corpus of meaningful written text of various categories, we try to propose some improvements, namely optimized rearrangements for the Turkish Q and F keyboards via some simple rules and heuristics. Our proposals result in more desirable and efficient keyboard layouts that increase the comfort and the speed of professional typists. The methods and procedures followed throughout this study can be extended and applied for any keyboard of other alphabets and languages.

Article History:

Received: 2016/02/09

Accepted: 2016/06/08

Online: 2016/06/30

Correspondence to: Asım Egemen

Yılmaz, Ankara University, Department

of Electrical-Electronics Engineering,

Gölbaşı, Ankara, TURKEY

Tel: +90 (312) 203 33 00/17 75

Fax: +90 (312) 212 54 80

E-Mail: aeyilmaz@eng.ankara.edu.tr

Key Words:

Language statistics; N-gram Statistics; Keyboard Design; Keyboard Layout; Optimization; Heuristics.

INTRODUCTION

The well-known Q (also known as QWERTY) keyboard has been the de-facto standard of typing machines (typewriters, computers) in majority of the world for more than a century. In the countries applying the Latin alphabet, this keyboard layout is used with minor modifications regarding the local character sets. Even though there exists no published evidence, there is a strong belief that the abnormal layout of the Q keyboard was intentionally preferred in order to decrease the speed of the typists and hence to avoid mechanical jams on the early typewriters. As a matter of fact, the key arrangement is so awkward that very infrequent letters “f” and “j” occupy the default positions of index fingers, namely the most valuable locations on the keyboard. Very frequent letters “a” and “e” seem to be hidden at locations accessible by the little and the middle fingers of the left hand, respectively [1]. Since the era of mechanical typewriters closed long ago, and there are currently no mechanical hurdles, more efficient keyboard designs are now realizable.

With this motivation, in this study, we investigate the possibilities of achievement of more efficient keyboard designs. For this purpose, in Section 2 we first try to formulate the design requirements for a keyboard, which are derived from ergonomic constraints. Then

in Section 3, we try to come up with suggestions for improvements in the Turkish F keyboard, which is the unarguable choice of professional typists in Turkey. In Section 4, we apply similar methodology for improvement to the more widely used Turkish Q keyboard. Discussions about the limitations and possible extensions of the current study together with the concluding remarks constitute the content of Section 5.

General requirements for keyboard design

Elimination of the weakness of the Q keyboard has been the concern of many researchers up to now. One of the most significant efforts was by Dvorak [2], who designed the so-called “American Simplified Keyboard” in 1932. The layout was patented in 1936 to the names of Dvorak and his brother-in-law Dealey [3]. Dvorak layout was aimed for professional typing in which 10 fingers are effectively used. For such usage, the areas of responsibilities for the hands and all fingers are as seen in Figure 1. As seen from the figure, the role and responsibility of each hand and each finger is strictly defined throughout the so-called “10-finger typing” technique. At this point, it is worth to state that despite the very common “10-finger typing” terminology, only 8 fingers are used effectively throughout this technique since both

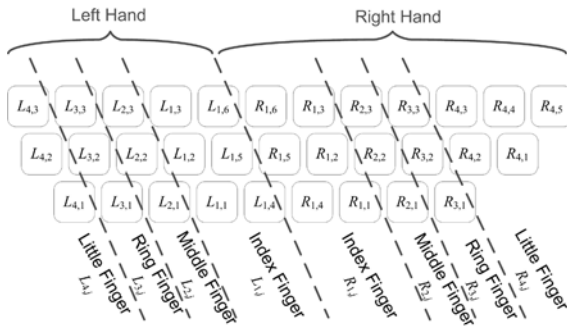


Figure 1. Figure 1. Finger placement and effort distribution for professional “10-finger typing” typing (which utilizes effective usage of only 8 fingers, since the thumbs are only used for pressing the space bar).

thumbs are used only for pressing the space bar.

Dvorak layout causes less finger motion, increases the typing speed and reduces the typing errors compared to the standard Q keyboard. Studying the letter frequencies in English and the human physiology (particularly the hands), Dvorak came up with the following principles for an ideal keyboard design [3]:

- There should be a balanced distribution between two hands (making the typing activity more rhythmic, increasing speed, reducing errors and fatigue).
- For maximum speed and efficiency, the most common letters and bigrams should be the easiest to type. This means that they should be on the home (i.e. the middle) row, which is where the fingers rest, and under the strongest fingers (As a matter of fact, about 70% of keyboard strokes on the Dvorak Simplified Keyboard are performed on the middle row).
- The least common letters should be on the bottom row, which is the hardest row to reach.
- The right hand should perform (slightly) more of the typing, because most people are right-handed.
- Bigrams should not be typed with adjacent fingers.
- Stroking should generally move from the edges of the board to the middle. An observation of this principle is that, for many people, when tapping fingers on a table, it is easier going from little finger to index than vice versa. This motion on a keyboard is called inboard stroke flow.

Meanwhile, Dvorak pointed out the major problems of the Q keyboard as follows (where the numerical figures of merit were not identified by Dvorak himself but some other researchers much later) [2]:

- Many common letter combinations require awkward finger motions.
- Many common letter combinations are typed with the same finger.

- Many common letter combinations require a finger to jump over the home row.
- Many common letter combinations are typed with one hand while the other stays in idle mode.
- Many common letter combinations are typed by adjacent fingers, which is slower than using other fingers.
- For an English text, about 56% of typing is performed with the left hand, which is the weaker hand for most people.
- For an English text, about 30% of typing is performed on the lower row, which is the slowest and most difficult row to reach.
- For an English text, about 52% of keyboard strokes are performed in the top row, requiring the fingers to travel away from the home row most of the time.

Table 1 summarizes the improvement of Dvorak layout compared to the standard Q keyboard (for English). It should also be noted that the Q keyboard causes an effort load of 56% for the left hand; whereas, Dvorak layout assigns 56% effort load to the right hand, which is stronger for majority of the people.

Table 1. Key stroke distributions for the Q and Dvorak simplified keyboards (per statistics of English).

Row	Original Q Keyboard	Dvorak Simplified Keyboard
Top	52%	22%
Middle	32%	70%
Bottom	16%	8%

As a matter of fact, trying to achieve more ergonomic key stroke distributions (considering the keyboard rows and attaining the highest load to the middle row; and also considering the effort loads of both hands) have so far constituted the main aim of some previous studies. In [4], Wagner et al. applied Ant Colony Optimization for re-arrangement of the standardized keyboards based on English, German and French keyboards, separately. Via simple rules and heuristics, Abbasov et al. applied a similar approach for an ideal keyboard arrangement for Azerbaijani Turkish in [1]; Dasgupta et al. conducted a similar study for Bangla language in [5]. Deshwal and Deb applied Genetic Algorithm for the solution of the same problem for Hindi language in [6]; meanwhile, Malas et al. applied it for Arabic in [7]. With the same motivation, in this study we try to achieve more-optimized rearrangements of Turkish F and Q keyboards. For this purpose, we use the statistics of Turkish and a simple heuristic to be described in the upcoming sections.

In the literature, there are also other sorts of studies regarding keyboard design:

- One of the major topics is achievement of the optimized industrial design of the keyboards with the concerns regarding the human posture and the positioning of wrists, fingers, tendons, etc.
- Another area of interest for many researchers is to achieve optimal arrangements for the so-called “Single Finger Keyboards”, which have evolved throughout the development of technology:
- In the last two decade, Single Finger Keyboards were in the form so that multiple characters were assigned to limited number of solid keys. The most common examples are the ones on the traditional phones and old-generation cellular phones (e.g. where the key “2” is attained to the letters “A”, “B” and “C”). The main concern was to find the ideal layouts for such keyboards to decrease the single finger (usually assumed to be the thumb of the right hand) in such studies.
- Especially after the development of the smart phones and tablet PCs, these keyboards evolved in a way that there are sufficient number of keys (compared to the number of letters in the alphabet) which are soft and reconfigurable. Again, the main concern in current studies is to find the ideal layouts for such keyboards to decrease the single finger (usually still assumed to be the thumb of the right hand).

Our study does not have any concerns regarding to human posture; it also does not deal with Single Finger Keyboards. Hence it should not be confused with studies of these sorts.

Improvement in Turkish F keyboard

Motivated from the fact that the Q keyboard is not appropriate for the statistics and characteristics of Turkish, and inspired from the methodology of Dvorak, Yener et al. conducted research for achievement of an optimum keyboard layout for Turkish between 1955-66 [8]. This layout, which is referred to as the “F keyboard”, has been the cult but unarguable choice of professional typists (or touch-typists, or 10-finger typists) such as secretaries, clerks, etc. The layout has been declared to be a national standard in 1974 [9]. It should also be noted that Marsan has initiated a similar study in France in order to achieve an optimum keyboard layout for French in 1970s, and the outcome of this study (so called “Marsan” keyboard) has been declared as a national standard in 1987 in France.

For the construction of the layout, Yener et al. performed a dictionary-based frequency analysis on 30,000 words; and identified the occurrence frequencies of each letter. Based on these statistics and using the guidelines of Dvorak (mentioned in Section II), they constructed the layout. An additional design decision was to distribute all

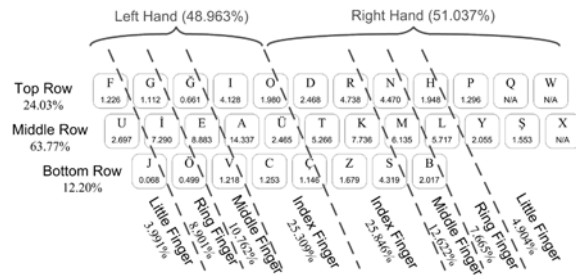


Figure 2. Layout of the original F keyboard (letter frequencies obtained from dictionary based analysis - adapted from [9]).

vowels inside the left hand’s area of responsibility. Since each syllable in Turkish has to include exactly one vowel, this yields a balanced distribution between the left and the right hands. The F keyboard layout is seen in Figure 2 together with the letter frequencies per dictionary-based analysis.

The F keyboard unarguably fits much better to Turkish compared to the Q keyboard, since:

- it increases the key stroke distributions in the home (middle) row,
- it decreases the responsibilities of weaker fingers (such as the little and ring fingers), and
- it assigns slightly much more responsibility to the right hand.

As a matter of fact, in organizations such as typing contests, F keyboard users have so far outperformed to the Q keyboard users numerous times. However, we identify a major deficiency in the design procedure of the F keyboard: dictionary based frequency analysis. In fact, in order to achieve an optimum keyboard layout, the letter statistics shall be extracted from a sufficiently large corpus of meaningful Turkish texts of various categories rather than a dictionary. The major reasons for this can be listed as follows:

- In daily life, a typist would deal with typing meaningful texts, not the words listed dictionary.
- In daily usage, the frequencies of the words are not identical; and hence considering them as equally-frequent (as in the dictionary based analysis) is misleading.
- Turkish is an agglutinative language, and the majority of the words in meaningful texts are inflected, not in their stem forms as in dictionaries. From this point of view, dictionary based analysis is again misleading.

In [10-11], we have performed such a text based analysis

Table 2. Letter frequencies in Turkish (results obtained via dictionary based analysis [9] and text based analysis [10-11]).

Letter	Dictionary Based Analysis [9]		Text Based Analysis [10-11]		Relative Frequency Change (%)
	Frequency	Order	Frequency	Order	
a	14.34%	1	11.46%	1	20.07%
b	2.02%	16	2.67%	15	-32.37%
c	1.25%	22	0.92%	25	26.58%
ç	1.15%	25	1.05%	23	8.73%
d	2.47%	13	4.60%	8	-86.39%
e	8.88%	2	9.07%	3	-2.11%
f	1.23%	23	0.49%	28	60.03%
g	1.12%	26	1.15%	20	-2.68%
ğ	0.66%	27	1.05%	22	-58.40%
h	1.95%	18	1.11%	21	43.02%
ı	4.13%	11	4.56%	9	-10.47%
i	7.29%	4	9.32%	2	-27.85%
j	0.07%	29	0.05%	29	26.47%
k	7.38%	3	4.65%	7	36.96%
l	5.72%	6	6.40%	6	-11.95%
m	6.14%	5	3.51%	11	42.79%
n	4.47%	9	7.42%	4	-66.00%
o	1.98%	17	2.58%	16	-30.30%
ö	0.50%	28	0.77%	27	-54.31%
p	1.30%	21	0.87%	26	32.87%
r	4.74%	8	7.04%	5	-48.59%
s	4.32%	10	3.15%	13	27.07%
ş	1.55%	20	1.53%	18	1.48%
t	5.27%	7	3.60%	10	31.64%
u	2.70%	12	3.14%	14	-16.43%
ü	2.47%	14	1.92%	17	22.11%
v	1.22%	24	1.01%	24	17.08%
y	2.06%	15	3.32%	12	-61.56%
z	1.68%	19	1.50%	19	10.66%

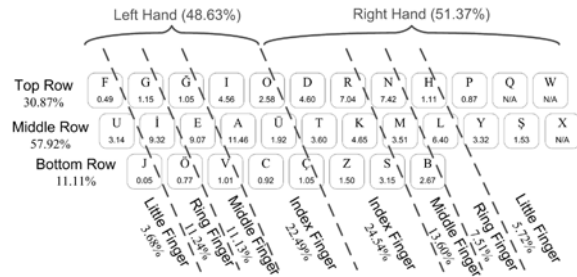


Figure 3. Layout of the original F keyboard (letter frequencies obtained from our text based analysis).

dictionary based analysis show that the most frequent 8 letters are “a, e, k, i, m, l, t, r”; whereas they are “a, i, e, n, r, l, k, d” for the text based analysis. The “relative frequency change” quantity seen in Table 2 is defined as follows:

$$\text{Relative Frequency Change} = 100 \times [(\text{Dictionary Based Analysis Frequency} - \text{Text Based Analysis Frequency}) / \text{Dictionary Based Analysis Frequency}]$$

where negative values express reduction in frequency, and positive values express increasing frequency.

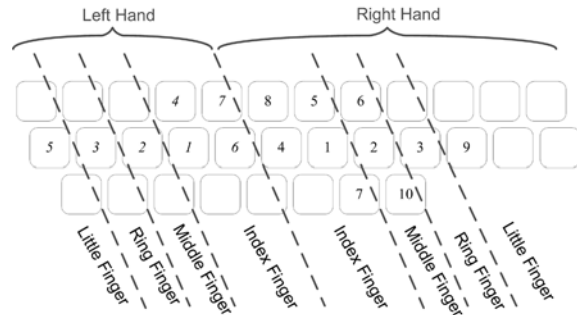


Figure 4. Procedure followed during the design of the original F keyboard: The numbers on the keyboard identify the “value” of the relevant position.

for evaluation of the *n*-gram statistics for Turkish; where the contents and details of the corresponding corpus used throughout the analysis can be found. As seen in Table 2, the letter frequencies are quite different compared to the results obtained via dictionary based analysis. Particularly,

Considering the letter frequencies per text based analysis, the performance of the F keyboard regarding the key stroke distributions seems to be degraded as seen in Figure 3. The usage rate of the top row is in fact 30.87% (not 24.03%); and the usage rate of the home (middle) row is

Table 3. Improvements in hand/finger and row usage rates for the F keyboards (original versus our modified version).

	Original F Keyboard			Modified F Keyboard		
	Left Hand	Right Hand	Total	Left Hand	Right Hand	Total
Finger						
Index	22.49%	24.54%	47.03%	22.49%	25.00%	47.49%
Middle	11.13%	13.60%	24.73%	11.38%	11.73%	23.11%
Ring	11.24%	7.51%	18.75%	10.99%	8.28%	19.27%
Little	3.68%	5.72%	9.40%	3.68%	5.55%	9.23%

Row	Original	Modified
	F Keyboard	F Keyboard
Top	30.87%	22.67%
Middle	57.92%	65.76%
Bottom	11.12%	11.48%

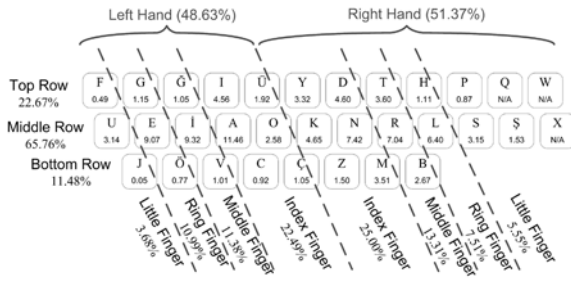


Figure 5. Layout of the modified F keyboard (letter frequencies obtained from text based analysis).

57.93% (not 63.77%). Hence, the layout shall be reconsidered by using the text based analysis results.

Even though not explicitly published, it can be deduced that Yener et al. followed the procedure pictorially depicted in Figure 4. The numbers on the keyboard in this figure identify the “value” of the relevant position. Namely, the number 1 denotes the most valuable position since it is the anatomically most accessible one. Hence, the more frequent a letter occurs, the more valuable of a position it gets. Inside the left hand’s area of responsibility, they have assigned the vowels (starting from the most frequent) to the positions seen in the figure. Similarly, they have assigned the consonants (starting from the most frequent) to the positions seen in the figure inside the right hand’s area of responsibility.

We implement a simple heuristic applying the same procedure, but this time relying on the text based statistics. This yields the layout given in Figure 5. With this layout, the home (middle) row usage rate is increased to 65.76%, and the top row usage rate is decreased to 22.67% keeping the bottom row usage rate at almost the same level. This layout also preserves the responsibilities of the left and the right hands and the fingers at reasonable levels. Compared results are summarized in Table 3.

Improvement in Turkish Q keyboard

Even though the Q keyboard is well known to be inefficient, it has dominated the market and economically outperformed all alternatives. Also in Turkey, a slightly modified version of it (by addition of the Turkish special characters) seen in Figure 6 is widely used.

In Germany, in order to increase the efficiency of the Q keyboard, the positions of the letters “z” and “y” was interchanged. In order to distinguish these two layouts, the original Q keyboard is referred to as the QWERTY layout, while the German-modified version of it is referred to as the QWERTZ layout. Inspired from this, we now try to improve the row usage rates and hand/finger responsibilities by

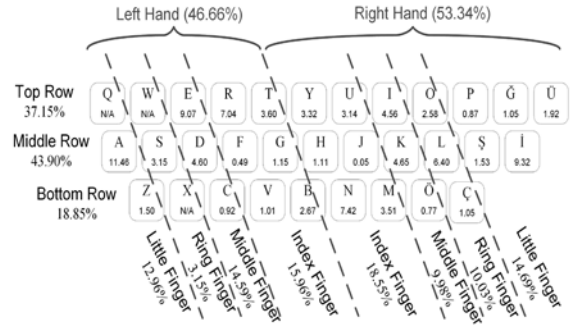


Figure 6. Layout of the original Turkish Q keyboard (letter frequencies obtained from text based analysis).

interchanging the positions of some particular letters.

As seen in Figure 6, the original Q keyboard layout yields quite high little finger usages (which is the weakest finger), quite low index finger usages (which is the strongest finger); almost same middle and top row usages, and quite high bottom row usage. The following observations can be made:

- “f” and “j” occupy the most valuable positions (middle row and index finger), even though they have quite low frequencies.
- “a” and “i” are at hardly accessible positions even though they have the highest frequencies.
- “e”, “r” and “n” have considerable frequencies, but they are not positioned at the middle row.
- “l” has a considerable frequency, but assigned to a relatively weak finger, the ring finger.

Hence for a new keyboard layout, the following letters are positionally interchanged: “a↔f”, “i↔j”, “e↔d”, “n↔h”, “r↔g”, “l↔k”; which yields the layout seen in Figure 7. By these modifications, the middle row usage rate is raised to 60.57% (from 43.90%), the top and bottom row usages rates are reduced to 26.79% (from 37.15%) and 12.54% (18.85%), respectively. Index finger usage rates are dramatically

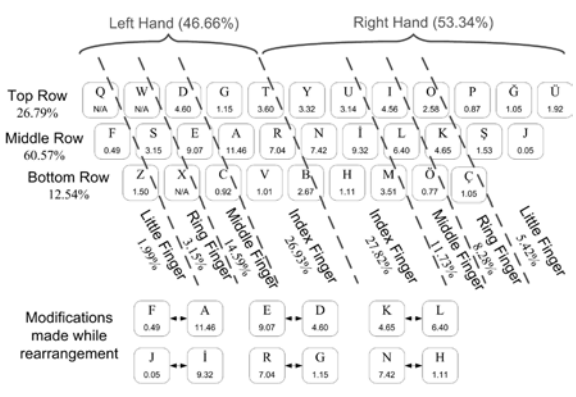


Figure 7. Layout of the original Turkish Q keyboard (letter frequencies obtained from text based analysis).

Table 4. Improvements in hand/finger and row usage rates for the Q keyboards (original versus our modified version)

	Original Turkish			Modified Turkish			Row	Original Turkish Q Keyboard	Modified Turkish Q Keyboard
	Q Keyboard		Total	Q Keyboard		Total			
	Left Hand	Right Hand		Left Hand	Right Hand				
<i>Finger</i>									
<i>Index</i>	15.96%	18.55%	34.51%	26.93%	27.82%	54.75%	Top	37.15%	26.79%
<i>Middle</i>	14.59%	9.98%	24.57%	14.59%	9.98%	24.57%	Middle	43.91%	60.57%
<i>Ring</i>	3.15%	10.03%	13.18%	3.15%	10.03%	13.18%	Bottom	18.85%	12.54%
<i>Little</i>	12.96%	14.69%	27.65%	1.99%	5.42%	7.41%			

increased, meanwhile the ring and the little finger usages are dramatically decreased with these modifications. Effects of the modifications are summarized in Table 4.

CONCLUSION

In this study, we demonstrated that it is possible to increase the effectiveness of the keyboard layout with a similar approach applied in [1, 4-7]. By using the language statistics, we tried to make improvement suggestions for both the Q and F keyboards. Our proposals seem to have more fair key stroke distributions (in terms of row usages and hand/finger responsibilities).

In fact, it is not desired to have the elements of popular bigrams positioned at the area of responsibility of the same finger. Such a requirement converts the keyboard design to a multiobjective optimization problem. In our ongoing research studies, we try to formulate the problem in this manner and try to find the Pareto fronts via metaheuristics such as Genetic Algorithms and Ant Colony Optimization algorithm by also considering the bigram statistics obtained for Turkish in [10-11].

ACKNOWLEDGEMENTS

The authors would like to express our gratitude to the anonymous reviewers for their precious time and effort spent throughout their careful examination and evaluation of the manuscript as well as their guidance and helpful comments for improvement.

REFERENCES

1. Abbasov A, Hajiyev A, Afandiyev G. Statistical approach for an optimal placement of the letters of different alphabets on a computer keyboard. *Applied and Computational Mathematics* 8 (2009) 36–41.
2. Cassingham RC. *The Dvorak Keyboard*, Freelance Communications, California (USA), 1986.
3. Dvorak A, Dealey W. *American simplified keyboard*. U.S. Patent Nr: 2,040,248, 1936.
4. Wagner MO, Yannou B, Kehl K, Feillet D, Eggers J. Ergonomic modelling and optimization of the keyboard arrangement with an ant colony algorithm. *Journal of Engineering Design* 14 (2003) 187–208.
5. Dasgupta T, Basu A, Das A, Mandal P. Design and evaluation of Bangla keyboard layouts. Paper presented at the IEEE Students' Technology Symposium, Kharagpur, India, 3–4 April. IEEE Publication Department, New York (NY), USA, pp. 248–254, 2010.
6. Deshwal PS, Deb K. Ergonomic design of an optimal Hindi keyboard for convenient use. Paper presented at the IEEE Congress on Evolutionary Computation, Vancouver BC, Canada, 16–21 July. IEEE Publication Department, New York (NY), USA, pp. 2187–2194, 2006.
7. Malas TM, Taifour SS, Abandah GA. Toward optimal Arabic keyboard layout using genetic algorithm. Paper presented at the 9th International Middle Eastern Multiconference on Simulation and Modeling (MESM 2008), 26–28 August. IEEE Publication Department, New York (NY), USA, pp. 1–4, 2008.
8. Anonymous. The struggle of the F keyboard (in Turkish). *Electrical Engineering* 431 (2007) 36.
9. Turkish Standards Institute. *Turkish standards - basic keyboard layout* (in Turkish). 1991.
10. Çiçek E, Yılmaz AE. A study on the n-gram and syllable based statistical properties of Turkish (in Turkish). Paper presented at the 3rd Engineering and Technology Symposium (MTS3), Ankara, Turkey, 24–25 April. Çankaya University Publications, Ankara, Turkey, pp. 68–77, 2010.
11. Çiçek E, Yılmaz AE. A new Morse code scheme optimized according to the statistical properties of Turkish. *Turkish Journal of Electrical Engineering and Computer Sciences* 21 (2013) 804–811.

Microstructural Analysis of Austempered Ductile Iron Castings

Barış Çetin¹, Halim Mecoc¹, Kemal Davut^{2,3}, Ebru Arslan³, Mustafa Can Uzun⁴

¹ FNSS Defense Systems Co. Inc., Engineering and Research Department, Ankara, TURKEY

² Atilim University, Metallurgical and Materials Engineering Department, Ankara, TURKEY

³ Atilim University, Metal Forming Center of Excellence, Ankara, TURKEY

⁴ TOBB University of Economics & Technology, Mechanical Engineering Department, Ankara, TURKEY

ABSTRACT

Austempered ductile iron (ADI) castings have a wide range of application areas in engineering designs due to their promising mechanical properties and lower cost. ADI has very good strength and toughness values at the same time its ductility is relatively high compared to most of the other cast irons. These promising mechanical properties originate from combination of specific graphite and matrix microstructure. The size, shape and fraction of graphite as well as the matrix microstructure influences the mechanical properties. In this paper the efforts regarding to a localization project of ADI is presented. In a more detailed manner, the first locally produced ADI which cannot satisfy the mechanical properties stated in ISO 17804 is compared with the original sample which is conform with the standard. The two pieces are inspected by mechanically and microstructurally by means of which necessary actions are detected for the local production. In other words the relation between the macro mechanical properties and the microstructural conditions are tried to be clarified.

Key Words:

Austempered Ductile Iron; Mechanical properties; Microstructure; Graphite; Nodularity.

INTRODUCTION

Austempered ductile iron (ADI) is a specific type of spheroidal graphite cast iron (SGCI) grade which has attractive mechanical properties such as high tensile, fatigue strength, toughness and relatively good ductility. The grey cast iron, which is a widely-used engineering material, can have maximum 400 MPa ultimate tensile strength (UTS) values due to flake type of graphite. The flakes promote notch-effect and reduce ductility as well [1]. However if the graphite shape can be changed to a spheroidal or nodular form with some special casting techniques the UTS may reach to 800 MPa [2]. Further improvement of mechanical properties is possible by applying heat treatments, such as austempering, that change the matrix microstructure. The excellent mechanical properties of ADI, in particular the favorable combination of high tensile strength, wear resistance and ductility, predestine this material to act as a substitute for forged or case-hardened materials and Ductile Iron (DI) [2].

ADI also offers some technical advantages on engineering components such as, being weightless and damping vibrations. According to these facts, the usage of ADI, in especially automotive, earth moving machines and defense system industries has been developed in recent years. The important components in automotive which can be replaced with ADI are crank shaft, connecting rod, cam shaft, timing gear set, piston, suspension, etc. There are several automobile components, where ADI has been recommended for replacement of forged components [2-7].

The chemical composition of ADI is similar to that of conventional nodular or ductile cast iron. However, some alloying elements such as nickel, molybdenum, and copper are usually added to increase its heat treatability [8], i.e. to delay the onset of the decomposition of austenite into pearlite, and allowing room for austempering.

Article History:

Received: 2016/05/04

Accepted: 2016/06/15

Online: 2016/06/30

Correspondence to: Barış Çetin, FNSS Defense Systems Co. Inc., Engineering and Research Department, Ankara, TURKEY

Tel: +90 (312) 4974619/1635

Fax: +90 (312) 4974301

E-Mail: cetin.baris@fnss.com.tr

Proper heat treatment will avoid the formation of unwanted microstructural constituents such as pearlite, martensite, or carbide [9].

The microstructure and properties of ductile iron castings have been subject of intense research since its discovery in 1948 [10], including the size, shape and distribution of graphite particles [11] as well as the fraction and morphology of matrix phases [12], including retained austenite [13]. The matrices of those materials are controlled via heat treatments [14]. The effect of ADI microstructure on fatigue strength [15], rolling contact fatigue resistance [16], machinability [17], wear resistance [18], toughness [19] and fracture toughness [20] have been studied. However, the combined effect of both nodularity and matrix phase composition has not been fully exploited. Moreover, most of the referred studies rely on laboratory scale productions. In the present study, all the tests were conducted on industrial scale productions, including local productions.

The present study aims at performing quantitative metallographic analysis on ADI samples from 2 different lots showing different tensile behavior. The graphite nodularity and matrix phase composition of the samples were determined via optical and scanning electron microscopes as well as X-ray diffraction; and then those results were correlated to the mechanical behavior obtained from simple tension and hardness tests. After understanding the correlation between microstructure and mechanical properties, the newly produced lots of ADI components satisfy the requirements.

PRODUCTION STEPS OF ADI

The basic production steps of ADI are austenizing, austempering and final quench to room temperature. The production process involves a first austenizing as cast sample in the temperature range of 871–982 °C for sufficient time to get a fully austenite (γ) matrix and then quenching it to an intermediate temperature range of 260–400 °C. The casting is maintained at this temperature for 1–4 h [21]. The microstructure of ADI depends on austempering temperatures and times. Because of this reason, a wide range of mechanical properties can be obtained. Especially by determining a specific process window for the whole heat treatment operation the appropriate combination of high yield strength (YS) and high toughness could be provided [22].

An exemplar time temperature transformation diagram (TTT curve) and heat treatment process of ADI are illustrated in Figure 1.

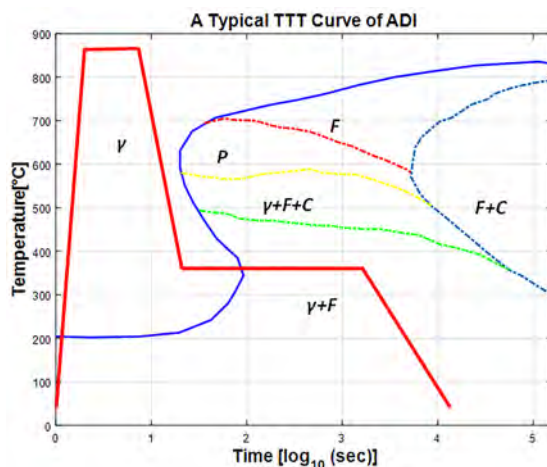


Figure 1. Schematic representation of TTT and a typical heat treatment cycle of ADI (adapted from [23])

MICRO STRUCTURAL CHARACTERIZATION STUDIES

In this study, two ADI samples exhibiting different mechanical properties were subjected to metallographic examination. As discussed, the mechanical properties of ADI are affected by the matrix composition and the characteristics of nodular graphites. The characteristics of graphite size, shape and distribution were investigated by quantitative analysis of optical micrographs taken with Nikon Eclipse LV 150 optical microscope using bright field illumination. The matrix microstructure was examined via Zeiss Evo LS 15 scanning electron microscope. For metallographic specimen preparation, firstly, the specimens were sectioned via Struers Secotom-10 precision cut-off machine and by electrical discharge machining (EDM) technique. Afterwards the specimens were subjected to 4 step grinding (240-400-600-1000 grit) with SiC papers and 3 step polishing (9 μ -3 μ -1 μ) with diamond paste. The optical micrographs were taken from the as-polished state of specimens to understand the quantify shape clearly. Afterwards the specimens were etched with picral (4 gr. Picric acid and 100 mL ethanol) solution. Nodularity analysis was performed on at least 10 micrographs per specimen using imageJ and Clemex Vision software solutions. The results of the characterization studies of two specimens are shown in Figure 2-6. It should be noted that the original sample has conform mechanical properties (YS: 700 MPa, UTS: 1000 MPa, Total Elongation: %6) with respect to ISO 17804 whereas the locally produced one did not satisfy the requirements [24].

The nodularity analyses are performed according to ASTM E2567 where [25]:

Table.1: Comparison of Nodularity Analysis of Two ADI Samples.

	Locally produced sample	Original Sample
Area Fraction of Graphite Particles	8.72 %	7.39 %
Area Fraction of Nodular Graphite Particles	7.51 %	6.55 %
% Nodularity by area	86.13 %	89.72 %
% Nodularity by number	58.56 %	78.47 %

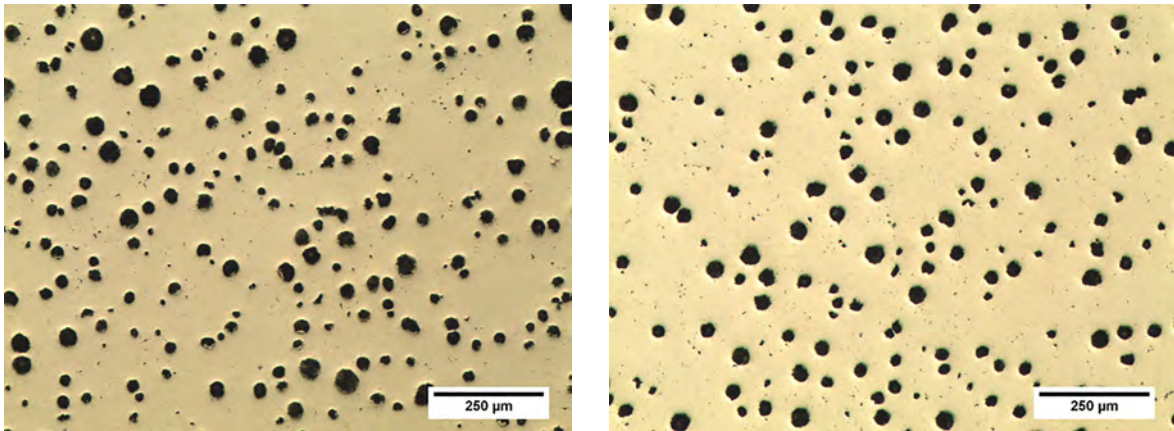


Figure 2. a) Optical micrograph of as-polished locally produced ADI sample (x50), b) Optical micrograph of as-polished original ADI sample (x50)

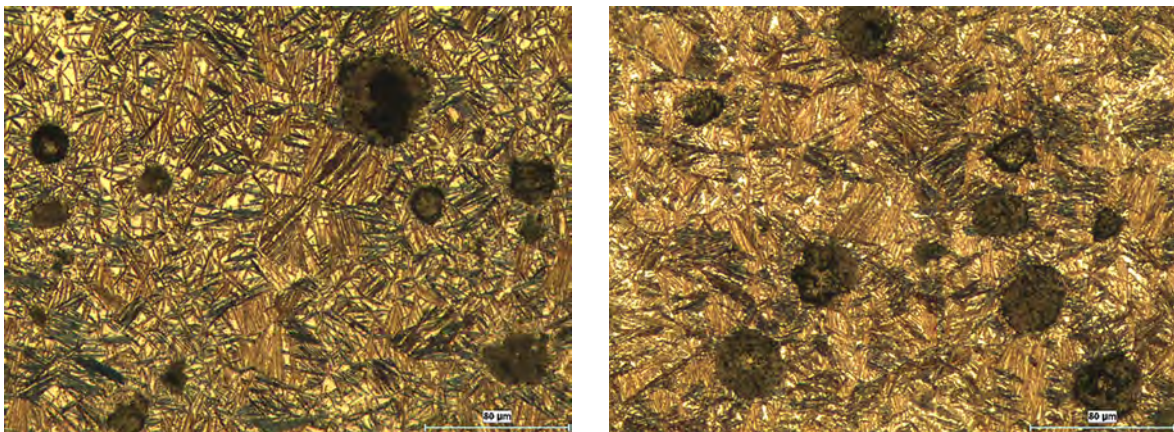


Figure 3. a) Optical micrograph of etched locally produced sample (x200), b) Optical micrograph of etched original sample (x200)

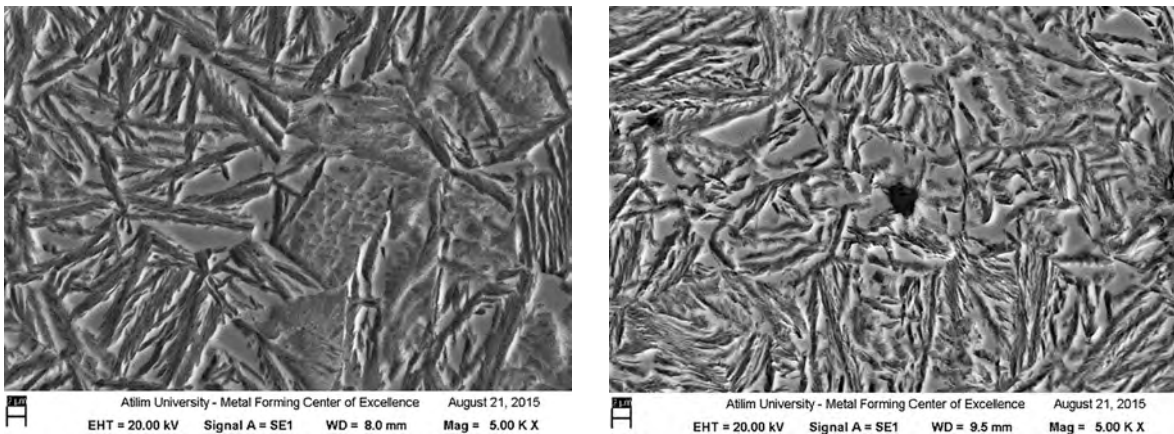


Figure 4. a) SEM micrograph of etched locally produced sample, showing its matrix (x5000), b) SEM micrograph of etched original sample showing its matrix (x5000)

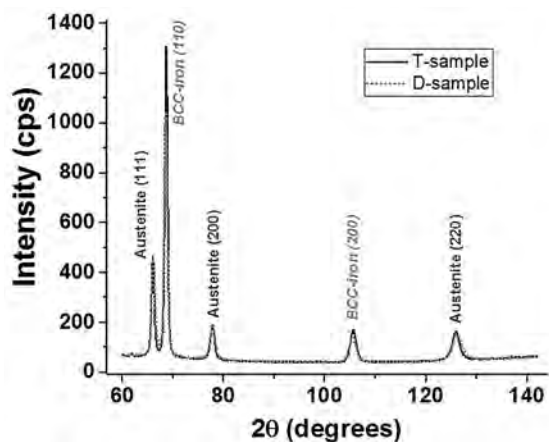


Figure 5. XRD spectra of locally produced (D) and original (T) samples shown comparatively. The peaks for austenite and BCC-iron phases used for quantification of phase fraction is also shown.

Area of reference circle = $\pi * (\text{Max. Feret Diameter})^2/4$

Shape Factor = Area of Graphite Particle / Area of Reference Particle

By the definition of ASTM E2567, the graphite particles whose shape factor are equal or greater than 0.60 is accepted as nodular. The others are treated as just graphite particle unless their max. Particles having a ferret diameter lower than 10 mm are excluded from the analysis. Therefore the percentage nodularities are calculated as follows:

%Nodularity by area = $100 * (\text{Area of Nodular Graphite Particles}) / (\text{Area of All Graphite Particles})$

%Nodularity by number = $100 * (\text{Quantity of Nodular Graphite Particles}) / (\text{Quantity of All Graphite Particles})$

The comparison of the two samples are illustrated in Table.1

The SEM micrographs in Figure 4 show different microstructures, indicating different matrix phase composition. In order to quantify the matrix phase compositions the amount of retained austenite in two samples were determined via X-Ray Diffraction analysis (XRD). XRD-analyses were performed with a GE-Seifert XRD 3003 PTS system, using Cr- K_{α} radiation. During the measurements χ -axis were oscillated and the Φ -axis were rotated in order to reduce the effects of crystallographic texture on results. The diffraction data was evaluated by the AutoQuan software. XRD analyses were illustrated in Figure 5. For each specimen an average hardness value was determined by measuring Vickers hardness at 10 different locations with Zwick / Roell ZHV 10 instrument using a load of 19.61 N applied at a speed of 25 mm/s.

The quantification of the XRD spectra shown in Figure 5 revealed phase fractions. It should be mentioned that, the BCC-iron peaks in the XRD spectra are mainly coming from martensite, bainite and presumably from ferrite phase or phase mixtures. It has been found that the original sample has 29.5 vol. % (+1.7;-1.4) retained austenite in comparison to the locally produced sample whose retained austenite content is %34,9 (+3.4;-2.5), as shown in Figure 6. The austenite content was calculated using the ratio of the integrated intensities of the corresponding peaks in Figure 6 and calculated R-values, in accordance with the ASTM-E975 standard [26]. The matrix hardness values are also shown and tabulated in Figure 6.

RESULTS and DISCUSSIONS

- It is observed that the quantity and the area based nodularity values of original sample is higher than locally produced one.
- When shape factor distribution is investigated it is stated that the original sample has a more stable (more likely to Gaussian normal distribution)

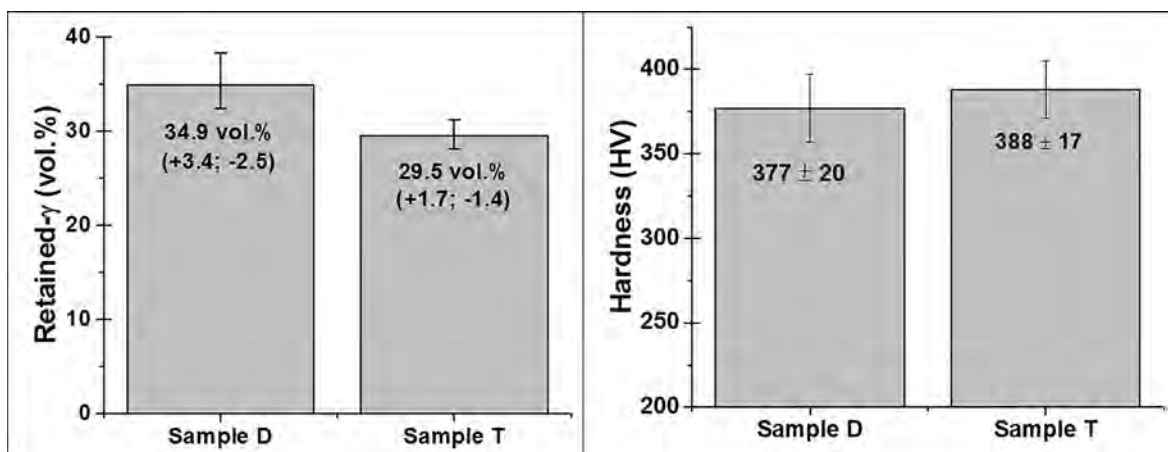


Figure 6. Comparison of retained austenite volume fraction (vol. %) and the matrix hardness values (HV) of the locally produced (D) and original (T) samples.

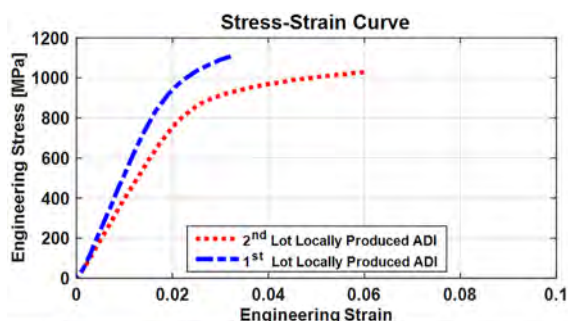


Figure 7. Tensile test results of the First and Second Lots

- dispersion compared to locally produced one.
- Both samples have relatively high nodularity values according to ASTM E 2567. It is concluded that the difference between the nodularity values is not sufficiently large to create reasonable changes in final mechanical properties.
- When the matrix structure is investigated individually, it is observed that the matrix is composed of nearly hundred percent of retained austenite and bainite for original sample. On the other hand the matrix structure of locally produced sample is composed of bainite, retained austenite and martensite. The retained austenite fraction is higher and it has a coarser microstructure for the locally produced sample.
- The hardness and strength of the original sample comes from the bainitic structure. The locally produced sample has a larger fraction of softer retained austenite, thus its strength and hardness comes from the martensite. As expected, the ductility of locally produced sample is lower due to martensite.
- The bainite structure of original sample is coarser than the locally produced sample.

In this study two ADI samples which are conform and unconform according to the mechanical properties designated in ISO 17804 are investigated microstructurally. As it is observed due to the bigger retained austenite and martensite content the locally produced sample has low ductility and uniform total elongation as expected. By performing detailed investigations and corrective actions especially on the heat treatment process (austempering temperature and duration) of locally produced one, a 2nd lot production is completed. In the second trial the locally produced sample could also satisfy the required mechanical properties. The tensile test results of the first and second lot of locally produced ADI material are shown in Figure 7. The second lot of the samples hardness drops slightly to 350 ± 14 . This shows that the 2nd sample has slightly softer and more ductile matrix. During deformation it can exhibit some degree of strain hardening and conform the tensile strength requirements.

CONCLUSION

The relation between microstructure and mechanical properties were studied in austempered ductile cast iron specimens. The fraction and nodularity of graphite particles were determined; the original sample has slightly better nodularity; however, the differences among the specimens were too small to explain the difference in tensile behavior. The matrix phase fractions and morphologies were determined by SEM and XRD studies. The locally produced sample has more retained austenite and martensite in its microstructure. Moreover the retained austenite and bainite structure appears coarser than the original sample. After taking measures in heat treatment process to decrease the amount of martensite and retained austenite the tensile properties of the 2nd lot of locally produced sample showed significant improvement for the uniform elongation while maintaining the required higher strength.

REFERENCES

1. ASM Handbook Volume 15: Casting, 2008, Materials Park, Ohio, USA
2. Cast Metals Development Ltd. Austempered Ductile-Iron Castings – Advantages, Production, Properties and Specifications. *Materials & Design* 13 5 (1992) 285–297.
3. F. Kolcke, Arft M, Lung D. Material-Related Aspects of the Machinability of Austempered Ductile Iron. *Springer*. 4 (2010) 433–411.
4. Putatunda S.K, Kesani S, Tackett R, Lawes G. Development of Austenite Free ADI (Austempered Ductile Cast Iron). *Materials Science and Engineering A* 435-436 (2006) 112-122.
5. Zimba J, Simbi D.J, Navara E. Austempered Ductile Iron: An Alternative Material for Earth Moving Components. *Cement & Concrete Composites* 25 (2003) 643-649.
6. Dhanasekaran S, Vadiraj A, Balachandran G, Kamaraj M. Mechanical Behaviour of an Austempered Ductile Iron. *63 5 (2010) 779-785*.
7. Guo X.L, Su H.Q, WU B.Y, LIU Z.G. Characterization of Microstructural Morphology of ADI by Electron Microscopy. *Microscopy Research and Technique* 40 (1998) 336-340.
8. Janowak J.F., Norton P.A. A Guide To Mechanical Properties Possible By Austempering, 1.5% Ni, 0.3% Mo Iron. *AFS Trans*. 88 (1985) 123-135.
9. Putatunda S.K. Development of Austempered Ductile Cast Iron (ADI) With Simultaneous High Yield Strength And Fracture Toughness By A Novel Two-Step Austempering Process. *Materials Science and Engineering A* 315 (2001) 70-80
10. Trudel A., Gagné M., "Effect of Composition and Heat Treatment Characteristics of Austempered Ductile Irons", *Canadian Metallurgical Quarterly: The Canadian Journal of Metallurgy and Materials Science* 36 (1997) 289 - 298
11. ASM Speciality Handbook: Cast Irons, Edited by Joseph R. Davis, ASM International 1996, Materials Park, Ohio, USA

12. Bahmani M., Elliott R., Varahram N., "The Austempering Kinetics and Mechanical Properties of an Austempered Cu-Ni-Mo-Mn alloyed Ductile Iron", *Journal of Materials Science* 32 (1997) 4783 - 4791
13. Aranzabal J., Gutierrez I., Rodriguez-Ibabe J.M., Urcola J.J., "Influence of the Amount and Morphology of Retained Austenite on the Mechanical Properties of an Austempered Ductile Iron", *Metallurgical and Materials Transactions A* 28A (1997) 1143-1156
14. Aranzabal J., Gutierrez I., Urcola J.J., "Influence of Heat Treatments on Microstructure of Austempered Ductile Iron", *Materials Science and Technology* 10 (1994) 728 - 737
15. Shanmugam P., Rao P.P., Udupa K.R., Venkataraman N., "Effect of Microstructure on the Fatigue Strength of an Austempered Ductile Iron", *Journal of Materials Science* 29 (1994) 4933 - 4940
16. Dommarco R.C., Bastias P.C., Dall'O H.A., Hahn G.T., Rubin C.A., "Rolling Contact Fatigue (RCF) Resistance of Austempered Ductile Iron", *Wear* 221 (1998) 69 - 74
17. Cakir C.C., Bayram A., Işık Y., Salar B., "The Effects of Austempering Temperature and Time on the Machinability of Austempered Ductile Iron", *Materials Science and Engineering A* 407 (2005) 147 - 153
18. Laino S., Sikora J.A., Dommarco R.C., "Development of Wear Resistant Carbide Austempered Ductile Iron (CADi)", *Wear* 265 (2008) 1 - 7
19. Eric O., Sidjanin L., Miskovic Z., Zec S., Jovanovic M.T., "Microstructure and Toughness of CuNiMo Austempered Ductile Iron", *Materials Letters* 58 (2004) 2707 - 2711
20. Putatunda S.K., Gadicherla P.K., "Influence of Austenitizing Temperature on Fracture Toughness of a Low Manganese Austempered Ductile Iron (ADI) with Ferritic as Cast Structure", *Materials Science and Engineering A* 268 (1999) 15 - 31
21. Kruthiventi S., Basavakumar K.G., Nambala S., Subramanyacharyulu G. Influence of Heat Treatment on Microstructural and Mechanical Properties of Nodular Cast Iron. *Journal of the Institution of Engineers: Series D* 95 (2014) 75 - 79
22. Kuş H, Akdemir A, Yazman Ş. Östemperleme Isıl İşleminin Ferritik Küresel Grafitli Dökme Demirin Aşınma Özellikleri Üzerine Etkisinin İncelenmesi. 14th International Materials Symposium, Denizli, Türkiye, October 2012
23. Keough JR, hayrynen KL, Pioszak GL. Designing with Austempered Ductile Iron. *Transactions of the American Foundry Society* 118 (2010) 503-517
24. ISO 17804:2005, Founding Ausferritic Spheroidal Graphite Cast Irons, Classification, ISO, Switzerland, www.iso.org
25. ASTM E2567-14, Standard Test Method for Determining Nodularity and Nodule Count in ductile Iron Using Image Analysis, ASTM International, West Conshohocken, PA, 2014, www.astm.org.
26. ASTM E975 -13, Standard Practice for X-Ray Determination of Retained Austenite in Steel with Near Random Crystallographic Orientation, ASTM International, West Conshohocken, PA, 2013, www.astm.org

Non-Enzymatic Phenol Determination in River Water Over Modified Electrode with Poly(3-methylthiophene)

Muammer Kavanoz, Ufuk Bük and Emine Ülker

Recep Tayyip Erdogan University, Department of Chemistry, Rize, TURKEY

ABSTRACT

This paper describes non-enzymatic phenol determination using poly(3-methylthiophene) coated Pt electrode. Modified electrode was prepared on Pt disc surface in dichloromethane medium containing 500 mM 3-methylthiophene (3MT) and 100 mM tetrabutylammonium perchlorate (TBAP). This electrode was used for amperometric determination of phenol in $\text{NaHSO}_4 / \text{Na}_2\text{SO}_4$ (SBS) solution at pH 2.0. For this purpose, 0.70, 0.80 and 0.90 V potentials were applied and results were compared. Limit of detection and linear range were found as 4.22×10^{-5} and $1.41 \times 10^{-4} - 4.00$ mM (with $R^2=0.9932$) at 0.90 V working potential, respectively. Repeatability of method was tested by using at least three modified electrode for 0.5, 1.0 and 2.0 mM phenol concentrations and relative standard deviation (RSD) were found as 2.49%, 1.92% and 2.75%, respectively. To test the accuracy of method and matrix effect, phenol determination was carried out for 1.0 and 2.0 mM phenol concentrations in artificially contaminated river water samples at optimum condition and recovery values were found as 96.44% and 99.60%, respectively. Proposed method was found as simple, rapid and economic for phenol determination.

Article History:

Received: 2016/04/19

Accepted: 2016/06/08

Online: 2016/06/30

Correspondence to: Muammer Kavanoz, Recep Tayyip Erdoğan University, Faculty of Science and Arts, Department of Chemistry, Rize, TURKEY
Tel: +90 (464) 2236226/1790
Fax: +90 (464) 2234092
E-Mail: muammer.kavanoz@erdogan.edu.tr

Key Words:

Phenol, Poly(3-methylthiophene), amperometric determination, non-enzymatic.

INTRODUCTION

Phenol is the simplest compound of benzene, and the main structure of phenolic compounds like hydroquinone and catechol. Phenol and its chemical derivatives are widely used in industrial area such as pharmaceutical drugs, cosmetic, pesticides, textile, dyes and petroleum refineries [1,2]. Phenol is released to the environment during its production, its use in phenolic resins, and organic synthesis [3]. Phenol is found in petroleum products, and it can be released by combustion of wood and auto exhaust [3]. Phenol is also released by the natural corruption of organic wastes including benzene. Phenol is a major metabolite of benzene [4], which is found widely in the environment, therefore, phenol may be occurred in the environment as a result of the natural corruption of benzene. Phenol and its vapors are toxic, and may give rise to harmful effects on the central nervous system and heart. Because of its toxicity and resistance to common microorganisms, detection of phenol is important in the environment [5]. A number of chromatographic [6,7] and spectrophotometric

[8] studies were reported for detection of phenol. However, these methods require sample preparation, expensive equipment and long analysis time. To overcome these problems, and for low-cost, simple and rapid determination of phenol, electrochemical methods attract attention. Especially, amperometric analysis based on modified electrode coated with conductive polymers [9], composite films [10,11], nanoparticles [12,13] and biosensors [14,15] is widely used for detection of phenol and its derivatives. .

Conductive polymer-based modified electrodes can easily be prepared on direct electrode surface by electrochemical methods. Poly (3-methylthiophene) (P3MT) is widely used conductive polymer for preparation of modified electrode. It was reported that P3MT was electrochemically synthesized on solid substrate material (Pt, Au, Glassy carbon) [16]. It was stated that P3MT films had electrocatalytic effect on phenolic compounds [17] and detection of phenolic compounds which using P3MT coated

electrodes give better responses compared to with bare electrodes [18]. P3MT-based modified electrode is used for detection of phenolic compounds due to its electronic [19] and optical properties, thermal stability [20], and electrocatalytic effect [17]. P3MT and its derivatives were electrochemically synthesized in dichloromethane [21], acetonitrile and acetonitrile-containing ferro sulfonic acid [22,23], chloroform [24] and perchloric acid solution [25]. Some studies were reported that P3MT-coated modified electrodes were used for determination of some phenolic compounds [26,27], riboflavin [28] and dopamine [17]. Also, polyaniline - poly(3-methylthiophene)-poly(3,3'-diaminobenzidine) (PANI - P3MT - PDAB) film for detection of dopamine [29], epinephrine [30] and PDAB - P3MT film for detection of catechol [31] were reported.

In a previous study, P3MT was synthesized in polymerization solution containing 500 mM 3MT and 100 mM TBAP [22] on Pt disc electrode in dichloromethane. In present study, this electrode was used for non-enzymatic phenol detection in SBS solution at pH 2.0 using amperometric I-t method. Also, real sample experiments in artificially contaminated river water samples were performed. Recovery values were calculated from the results of these studies.

MATERIAL AND METHODS

Reagent

3-methylthiophene monomer and phenol were purchased from Aldrich and Merck companies, respectively, and used without further purification. Electro-polymerization studies were carried out in dichloromethane medium containing TBAP as supporting electrolyte. TBAP was synthesized as mentioned in the literature [10]. Aqueous media studies were performed in sodium hydrogen sulfate (NaHSO_4) (Merck) and sodium sulfate (Na_2SO_4) (Merck) solution (SBS) of pH 2.0. Phenol solution was prepared in this solution at pH 2.0. All experiments were carried out in nitrogen atmosphere (Linde). Spiked sample assay was done for artificially contaminated river water samples with phenol. Before the experiment river water was adjusted to pH 2.0 by adding HCl.

Apparatus

All electrochemical experiments were performed with CH Instruments system, Model 1140B electrochemical analyzer. Conventional three-electrode electrochemical cell with Pt disc (area = $7.85 \times 10^{-3} \text{ cm}^2$) as working electrode, Pt wire as counter electrode and Ag/AgCl (for non-aqueous assay), and saturated calomel electrode (SCE) (for aqueous assay) as reference electrode were used. Before the experiments, Pt disc electrode was

cleaned with slurry of Cr_2O_3 with water, rinsed with triple distilled water, cleaned in the ultrasonic bath, washed with dichloromethane solution, and dried, respectively. All experiments were carried out in room temperature.

RESULTS AND DISCUSSION

Electrode preparation

In a previous study, P3MT was coated on Pt disc working electrode (P3MT/Pt) in dichloromethane medium containing 500 mM 3MT and 100 mM TBAP between -0.4V and 1.8V potential range vs. Ag/AgCl reference electrode (20 cycles) and washed with dichloromethane to remove the non-polymeric species [21]. In the present study, as prepared modified electrode was used for amperometric detection of phenol in SBS solution of pH 2.0 and river water artificially contaminated with phenol was used as analyte.

Electrochemical behavior of phenol over P3MT/Pt electrode

pH effect on modified electrode was investigated in SBS solution (pH 2.0 - 6.5) between 0.0 V and 0.9 V potential range vs. SCE. pH value in which the film has the most electroactivity was determined as 2.0. Therefore, electrochemical behavior of phenol was performed at pH 2.0 solution containing 5.0 mM phenol and results were compared with those of bare Pt electrode. Despite the oxidation potential of phenol was observed at about 0.87 V over bare Pt electrode (curve a), onset oxidation potential was measured at about 0.60 V over P3MT/Pt electrode (curve c) (Figure 1). Shifting the potential to smaller value is evidence of catalytic effect of P3MT film on Pt surface for the oxidation of phenol. Also, current value obtained over P3MT/Pt electrode in at pH 2.0 solution containing phenol is greater than obtained over bare Pt electrode. This can be explained with the fact that the interaction of P3MT film with phenol is greater than bare Pt electrode because of porous structure of the P3MT film [32].

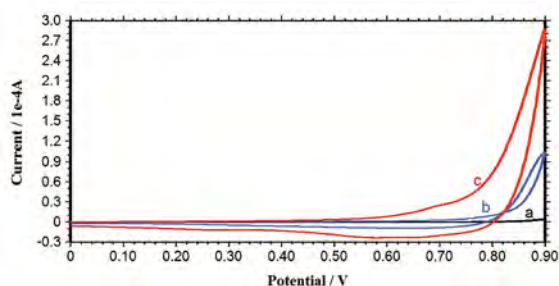


Figure 1. The cyclic voltammograms of (a) bare Pt electrode containing 5.0 mM phenol, (b) P3MT/Pt electrode and phenol free solution, (c) P3MT/Pt electrode containing 5.0 mM phenol in SBS solution at pH 2.0 (vs. SCE, $v = 100 \text{ mV s}^{-1}$)

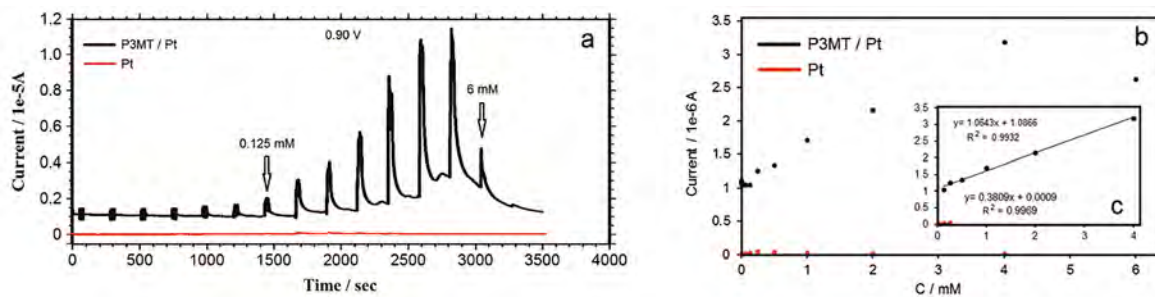


Figure 2. a) The current versus time curve for coated P3MT and uncoated Pt electrodes at 9.77×10^{-4} - 6.0 mM phenol concentration range b) current values versus phenol concentration and c) calibration graph (applied potential 0.90 V vs. SCE).

Amperometric phenol determination

For determination of phenol with amperometric I-t method in SBS of pH 2.0, P3MT film coated on Pt disc electrode between -0.4 V and 1.8 V potential was used. Initially, 0.70, 0.80 and 0.90 V potentials were separately applied on P3MT/Pt electrode about 1000 s to obtain steady-state current value. Afterwards, sufficient volume of stock phenol solution was added to attain the phenol concentration of 9.77×10^{-4} mM and the solution was stirred to obtain homogeneity. A typical current-time response was recorded with the successive addition stock phenol solution to the SBS solution for each potential and 0.90 V was determined as an optimum potential in which the maximum currents obtained. Figure 2 shows the amperometric I-t curves for an applied potential of 0.90 V (Figure 2a), current versus phenol concentration (Figure 2b) and calibration curves in linear scale (Figure 2c). In addition, same experiments were performed over uncoated Pt electrode and results were compared in Figure 2 (red). As seen in Figure 2a, current values increased as linearly until 4.0 mM phenol concentration. Over this concentration, the current values started to decrease. Limit of detection (LOD), limit of quantification (LOQ) and linear range values for P3MT/Pt electrode were calculated as 4.22×10^{-5} , 1.41×10^{-4} and 1.41×10^{-4} - 4.0 mM, respectively. 3 s/m and 10s/m equations were utilized for calculating of LOD and LOQ values [33] where s symbolizes the standard deviation calculated from the current values at the lowest concentration that generates a measurable current for three replicated measurements. Analytic parameters of different potentials over P3MT/Pt

and bare Pt electrode were summarized in Table 1.

Also, amperometric determination of phenol over P3MT/Pt electrode at optimum potential, and different pH solutions (2.0-6.5) was carried out. Typical current-time response was shown in Figure 3 (a) and it can be seen that results of pH 2.0 and pH 3.0 is competitive with each other. Therefore, response curve vs. phenol concentration obtained from amperometric I-t curve of pH 2.0 and pH 3.0 media and calibration graphs were compared in Figure 3 (b,c). According to Figure 3 (c), linear range obtained at pH 2.0 was longer than that of pH 3.0.

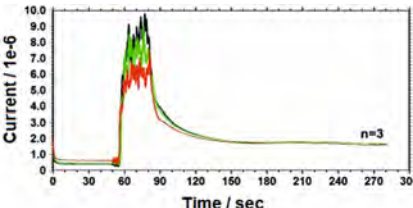
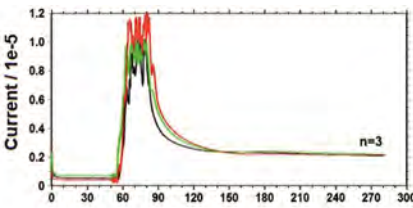
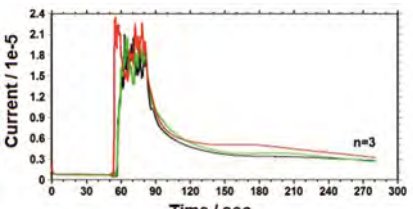
Repeatability studies

Repeatability of current values P3MT modified Pt electrode was investigated at pH 2.0 solution. Steady-state current values at the end of 200 s were recorded for each 0.50, 1.0 and 2.0 mM phenol concentrations after the electrolysis of P3MT/Pt electrode about 1600 s at 0.90 V. The results of repeatability experiment (amperometric I-t curves, current values, standard deviations, relative standard deviations and confidence intervals in 95% confidence level) for each phenol concentrations were shown in Table 2. To assess the accuracy, combined standard deviation was calculated as 0.1618 μ A using current values and it was used for calculating confidence interval. Standard deviations within the group were low and percent relative standard deviations were lower than 5% (Table 2). In addition, current values were close to each other in the group and they increased in proportion

Table 1. Analytic parameters for determination of phenol at different potentials over P3MT/Pt and bare Pt electrode

Applied Potential (V)	Electrode	LOD, (mM)	LOQ (mM)	Linear range (mM)	Equation	R ²
0.70	P3MT	2.69×10^{-4}	8.96×10^{-4}	8.96×10^{-4} - 20.0	$y = 0.0368x + 0.2601$	0.9847
	Pt	1.99×10^{-3}	6.64×10^{-3}	6.64×10^{-3} - 35.0	$y = 0.0005x + 0.0008$	0.9965
0.80	P3MT	1.44×10^{-5}	4.81×10^{-5}	4.81×10^{-5} - 1.0	$y = 0.7407x + 0.5136$	0.9781
	Pt	3.15×10^{-4}	1.05×10^{-3}	1.05×10^{-3} - 4.0	$y = 0.0122x + 0.0269$	0.9530
0.90	P3MT	4.22×10^{-5}	1.41×10^{-4}	1.41×10^{-4} - 4.0	$y = 1.0643x + 1.0866$	0.9932
	Pt	1.18×10^{-5}	3.94×10^{-5}	3.94×10^{-5} - 0.25	$y = 0.3809x + 0.0009$	0.9965

Table 2. Evaluation of the reliability of the results found from the repeatability experiment for detection of phenol over P3MT/Pt electrode.

C_{Phenol} (mM)	Amperometric I-t Curve	I μA	S μA	RSD %	$[\bar{X} \pm \frac{ts}{\sqrt{N}}]^{*,**}$ μA
0.50		1.650 1.681 1.600	0.0409	2.486	1.644±0.401
1.00		2.101 2.180 2.161	0.0412	1.920	2.147±0.401
2.00		2.782 2.641 2.756	0.0750	2.752	2.726±0.401

*95% confidence level was calculated.

**Confidence intervals were calculated using combined standard deviations.

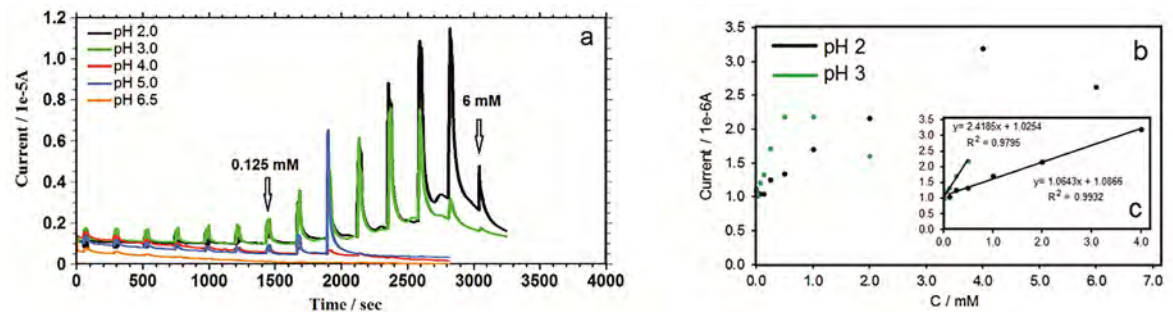


Figure 3. Calibration studies of phenol over P3MT/Pt electrode (a) Current-time responses for different pH values (b) current vs. phenol concentration for pH values of 2.0 and 3.0 (c) calibration graphs for pH 2.0 and pH 3.0 (applied potential 0.90 V vs. SCE).

to the concentration. These results supported the repeatability of the P3MT/Pt electrode.

Determination of phenol over P3MT/Pt electrode in artificially contaminated river water

In order to test applicability and matrix effect, detection of phenol over P3MT/Pt electrode was carried out in artificially contaminated river water in Rize, Turkey. Three samples were measured using three independently deposited electrodes. P3MT/Pt electrode prepared at optimum conditions was tested in spiked samples as described above for 1.0 and 2.0 mM phenol concentrations

and results were compared with standard 1.0 and 2.0 mM phenol concentrations (Table 2) and recovery values were calculated as 96.44% and 99.60%, respectively. Recovery values which are close to 100 % showed that the values obtained by the proposed P3MT/Pt electrode were in good agreement with the standard solutions. It is understood that the present electrode had great potential for practical application for the analysis in spiked samples.

Finally, obtained results were compared with previous studies. It was seen in Table 4, presented surface had better parameters compared to other modified electrode. Proposed

Table 3. Recovery results in artificially contaminated river water for phenol detection.

Samples	Added (C_{phenol}/mM)	Found (C_{phenol}/mM)	Recovery (%)
1	1.00	0.96	96.44
2	2.00	1.99	99.60

method was found simple, rapid and highly sensitive for phenol. Also, another advantage of the electrode was that it did not contain enzyme. This allows a lower-cost phenol determination.

CONCLUSION

Present study reported deposition of P3MT on Pt disc surface in dichloromethane solution for determination of phenol. Non-enzymatic phenol detection was successfully carried out in NaHSO₄ / Na₂SO₄ solution (at pH 2.0) applying 0.70, 0.80 and 0.90 V potentials. LOD, LOQ and linear range were found as 4.22×10^{-5} , 1.41×10^{-4} and 1.41×10^{-4} - 4.0 mM, respectively over the P3MT/Pt electrode. Also, to test availability for practical application, this electrode was used in artificially contaminated river water from Rize, Turkey and recovery values for 1.0 and 2.0 mM phenol concentrations were found as 96.44% and 99.60%, respectively. Proposed method was found simple, rapid, sensitive and low-cost for determination of phenol.

ACKNOWLEDGEMENTS

This research was supported by The Scientific and Technological Research Council of Turkey (TÜBİTAK) (Project no: 111T445)

REFERENCES

- Yang X, Zou R, Huo F, Cai D, Xiao D. Preparation and characterization of Ti/SnO₂-Sb₂O₃-Nb₂O₅/PbO₂ thin film as electrode material for the degradation of phenol. *Journal of Hazardous materials* 164 (2009) 367-373.
- Ma H, Zhang X, Ma Q, Wang B. Electrochemical catalytic treatment of phenol wastewater. *Journal of Hazardous materials* 165 (2009) 475-480.
- Wallace J. In Kirk-Othmer encyclopedia of chemical toxicology; Kroschwitz JI, Howe-Grant M, Eds.; John Wiley & Sons: New York, forth edition, pp. 592-602, 1996.
- Rothman N, Bechtold WE, Yin S-N, Dosemeci M, Li G-L, Wang Y-Z, Griffith WC, Smith MT, Hayes RB. Urinary excretion of phenol, catechol, hydroquinone, and muconic acid by workers occupationally exposed to benzene. *Occupational and Environmental Medicine* 55 (1998) 705-711.
- Švitel J. Development of Tyrosinase-Based Biosensor and Its Application for Monitoring of Bioremediation of Phenol and Phenolic Compounds. *Environmental Science & Technology* 32 (1998) 828-832.
- Vrsaljko D, Haramija V, Hadži-Skerlev A. Determination of phenol, m-cresol and o-cresol in transformer oil by HPLC method. *Electric Power Systems Research* 93 (2012) 24-31.
- Es-haghi A, Baghernejad M, Bagheri H. In situ solid-phase microextraction and post on-fiber derivatization combined with gas chromatography-mass spectrometry for determination of phenol in occupational air. *Analytica Chimica Acta* 742 (2012) 17-21.
- Zhao W, Liu W, Ge J, Wu J, Zhang W, Meng X, Wang P. A novel fluorogenic hybrid material for selective sensing of thiophenols. *Journal of Materials Chemistry* 21 (2011) 13561-13568.
- He K, Wang X, Meng X, Zheng H, Suye S-i. Amperometric determination of hydroquinone and catechol on gold electrode modified by direct electrodeposition of poly(3,4-ethylenedioxythiophene). *Sensors and Actuators B: Chemical* 193 (2014) 212-219.
- Kavanoz M, Pekmez NÖ. Poly(vinylferrocenium) perchlorate-polyaniline composite film-coated electrode for amperometric determination of hydroquinone. *Journal of Solid State Electrochemistry* 16 (2012) 1175-1186.
- Tehrani MAR, Ghadimi H, Ab Ghani S. Electrochemical studies of two diphenols isomers at graphene nanosheet-poly(4-vinyl pyridine) composite modified electrode. *Sensors and Actuators B: Chemical* 177 (2013) 612-619.
- Quynh BTP, Byun JY, Kim SH. Non-enzymatic amperometric detection of phenol and catechol using nanoporous gold. *Sensors and Actuators B: Chemical* 221 (2015) 191-200.
- Nurul Karim M, Lee HJ. Amperometric phenol biosensor based on covalent immobilization of tyrosinase on Au nanoparticle modified screen printed carbon electrodes. *Talanta* 116 (2013) 991-996.
- Çevik E, Şenel M, Baykal A, Abasıyanık MF. A novel amperometric phenol biosensor based on immobilized HRP on poly(glycidylmethacrylate)-grafted iron oxide nanoparticles for the determination of phenol derivatives. *Sensors and Actuators B: Chemical* 173 (2012) 396-405.

Table 4. Comparison of the analytical performance for the detection of phenol

Method	Electrode	LOD (mM ⁻¹)	Linear Range (mM)	R ²	Reference
Amperometry	Copper phtalocyanine and histidine on CPE	2.9×10^{-2}	0.040-0.350	-	[35]
Amperometry	HRP immobilised on silica gel modified with titanium oxide.	1×10^{-3}	1.0×10^{-2} - 5.0×10^{-2}	0.999	[36]
Amperometry	Tyrosinase immobilization on PAPCP/ITO	9×10^{-4}	1.8×10^{-3} -0.17	-	[37]
Amperometry	tyrosinase entrapped in polyacrylamide microgels	1.4×10^{-3}	5×10^{-3} - 2.2×10^{-2}	0.999	[38]
Amperometry	Con A and HRP thin films on a thiol-modified gold electrode	2×10^{-4}	$7,6 \times 10^{-3}$ - 6.84×10^{-2}	0.999	[39]
Amperometry	P3MT/Pt	4.22×10^{-5}	1.41×10^{-4} - 4.0	0.993	This work

15. Kulys J, Vidziunaite R. Amperometric biosensors based on recombinant laccases for phenols determination. *Biosensors and Bioelectronics* 18 (2003) 319–325.
16. Abacı S, Yildiz A. Electropolymerization of thiophene and 3-methylthiophene on PbO₂ electrodes. *Journal of Electroanalytical Chemistry* 569 (2004) 161–168.
17. Wang H-S, Li T-H, Jia W-L, Xu H-Y. Highly selective and sensitive determination of dopamine using a Nafion/carbon nanotubes coated poly(3-methylthiophene) modified electrode. *Biosensors and Bioelectronics* 22 (2006) 664–669.
18. Kelley A, Angolia B, Marawi I. Electrocatalytic activity of poly(3-methylthiophene) electrodes. *Journal of Solid State Electrochemistry* 10 (2006) 397–404.
19. Yadav K, Narula A, Singh R, Chandra S. Direct current conductivity studies on poly(3-methyl thiophene). *Applied Biochemistry and Biotechnology* 96 (2001) 119–124.
20. [20] Hanif M, Zuo L, Yan Q, Hu X, Shi M, Chen H. A novel electrochemically and thermally stable polythiophene for photovoltaic application. *Journal of Applied Polymer Science* 127 (2013) 161–168.
21. Kavanoz M, Bük U, Ülker E. Determination of hydroquinone using poly(3-methylthiophene) synthesized electrochemically on Pt electrode in methylene chloride. *Journal of Applied Polymer Science* 131 (2014).
22. Sato MA, Tanaka S, Kaeriyama K. Electrochemical preparation of highly conducting polythiophene films. *Journal of the Chemical Society, Chemical Communications* (1985) 713–714.
23. Udum YA, Pekmez K, Yildiz A. Electrochemical synthesis of soluble sulfonated poly(3-methyl thiophene). *European Polymer Journal* 40 (2004) 1057–1062.
24. [24] Kamat SV, Yadav JB, Puri V, Puri RK, Joo OS. Characterization of poly(3-methyl thiophene) thin films prepared by modified chemical bath deposition. *Applied Surface Science* 258 (2011) 482–488.
25. Bazzaoui EA, Aeiyaç S, Lacaze PC. Low potential electropolymerization of thiophene in aqueous perchloric acid. *Journal of Electroanalytical Chemistry* 364 (1994) 63–69.
26. [26] Wang J, Li R. Highly stable voltammetric measurements of phenolic compounds at poly(3-methylthiophene)-coated glassy carbon electrodes. *Analytical Chemistry* 61 (1989) 2809–2811.
27. Agüí L, Serra B, Yáñez-Sedeño P, Reviejo AJ, Pingarrón JM. Electrochemical Determination of Chlorophenols at Microcylinder Poly(3-methylthiophene) Modified Electrodes Based on a Previous Chemical Oxidation Using Bis(trifluoroacetoxy)iodobenzene. *Electroanalysis* 13 (2001) 1231–1236.
28. Zhang H, Zhao J, Liu H, Wang H, Liu R, Liu J. Application of Poly(3-methylthiophene) Modified Glassy Carbon Electrode as Riboflavin Sensor. *International Journal of Electrochemical Science* 5 (2010) 295–301.
29. Kavanoz M, Ülker E, Bük U. A Novel Polyaniline-Poly(3-Methylthiophene)-Poly(3,3'-Diaminobenzidine) Electrode for the Determination of Dopamine in Human Serum. *Analytical Letters* 48 (2015) 75–88.
30. Ülker E, Kavanoz M. Determination of Epinephrine in Human Serum over Polyaniline - Poly(3-methylthiophene) - Poly(3,3'-diaminobenzidine) Modified Pt electrode. *Canadian Journal of Chemistry* 93 (2015) 1239–1244.
31. Kavanoz M, Ülker E, Bük U. A New Modified Electrode Based on Poly(3,3'-diaminobenzidine) - Poly(3-methylthiophene) Copolymer Film for Amperometric Determination of Catechol. *Global Journal on Advances Pure and Applied Sciences* 1 (2013) 719–725.
32. Ülker E, Kavanoz M. Synthesis of Poly(Vinylferrocene) Perchlorate / Poly(3,3'-Diaminobenzidine) Modified Electrode in Dichloromethane for Electroanalysis of Hydroquinone. *Journal of the Brazilian Chemical Society* 26 (2015) 1947–1955.
33. Long GL, Winefordner JD. Limit of Detection A Closer Look at the IUPAC Definition. *Analytical Chemistry* 55 (1983) 712A–724A.
34. Del Pilar Taboada Sotomayor M, Tanaka AA, Kubota LT. Development of an enzymeless biosensor for the determination of phenolic compounds. *Analytica Chimica Acta* 455 (2002) 215–223.
35. Rosatto SS, Kubota LT, de Oliveira Neto G. Biosensor for phenol based on the direct electron transfer blocking of peroxidase immobilising on silica-titanium. *Analytica Chimica Acta* 390 (1999) 65–72.
36. Rajesh A, Kaneto K. A new tyrosinase biosensor based on covalent immobilization of enzyme on N-(3-aminopropyl) pyrrole polymer film. *Current Applied Physics* 5 (2005) 178–183.
37. Hervás Pérez JP, Sánchez-Paniagua López M, López-Cabarcos E, López-Ruiz B. Amperometric tyrosinase biosensor based on polyacrylamide microgels. *Biosensors and Bioelectronics* 22 (2006) 429–439.
38. Yang S, Chen Z, Jin X, Lin X. HRP biosensor based on sugar-lectin biospecific interactions for the determination of phenolic compounds. *Electrochimica Acta* 52 (2006) 200–205.

The Structural and Thermal Characterization of New Cu-Arginate Complex; Experimental and Simulated Hydrogen Adsorption Properties

Zarife Sibel Şahin¹, Zeynel Öztürk², Ömer Yurdakul³, Dursun Ali Köse³

¹ Sinop University, Department of Energy Systems Engineering, Sinop, TURKEY

² Hitit University, Department of Chemical Engineering, Corum, TURKEY

³ Hitit University, Department of Chemistry, Corum, TURKEY

ABSTRACT

The copper-arginate complex was synthesized and characterized by using FTIR, TG/DTA-DrTG, UV-Vis spectroscopy and elemental analysis methods. In addition, experimental and theoretical hydrogen storage capabilities were investigated. The unit cell of complex structure included that one mole CuII as centered cation and one mole of free NaI cation and one mole of NaSO_4^- as coordinated to arginine ligand and two moles of arginate ligands and one mole of aqua ligand as coordinated to NaSO_4^- . The CuII cation had square-pyramidal coordination sphere and the NaI metal cation had trigonal coordination scheme. The other sodium metal cation (Na2) was implemented in the released position as counter ion of NaSO_4^- . It was found that the arginine complex, synthesized in this work have 0.533 m^2/g BET surface area and 6.92E-3 wt. % hydrogen storage capacity at 77 K and 1 bar while simulated value was 3.27E-3 wt. % for the same conditions. .

Article History:

Received: 2016/05/03

Accepted: 2016/06/14

Online: 2016/06/30

Correspondence to: Dursun Ali Köse,
Hitit University, Faculty of Science and
Arts, Department of Chemistry, Corum,
TURKEY

Tel: +90 (364) 270 0000/1643

Fax: +90 (312) 270 0005

E-Mail: dalikose@hitit.edu.tr

Key Words:

Helix Structure; Arginate Complex; Transition Metal Complex; Thermal Decomposition; Electronic Spectra; Cu(II) Complex; X-Ray Diffraction Analysis.

INTRODUCTION

The amino acid molecules are strong Lewis acid base coordinating to metal cation centers. One of them, arginine (Arg), is a very significant amino acid that has guanidium group in side chain, which has basic character at large pH scale. Therefore, it operates as a biological identification site through directed hydrogen bonds [1,2].

The coordination compounds of amino acids or peptides with metal cations are also critical to be model systems for comprehension of biochemical processes in living organisms and some industrial process [3]. The coordination bonding between amino acids and metal cations is well known. This bonding is carried out via a chelate binding mode involving both carboxylate and amine groups, so it is very strong type. [4]. The metal cations support intermolecular coactions by coordinating the interacting molecules in suitable positions [5,6]. Recently, interest to coordination

compounds of amino acids with metal cations have been increased because they have confirmed to be useful for some biological applications and material applications for gas absorption [7-9]. Also, the complex compounds of metal cations with bioactive ligands are more influential than pure bioactive compounds most of the time [10,11]. It was explained enough that heterocyclic compounds took an important part in many biological systems [12-15]. Moreover, the anti-bacterial and anti-microbial effect of some drugs could be increased via chelation to center of a metal cation. Herewith, to obtain powerful anti-microbial species, it is very significant to identify about structure and bonding properties of coordination compounds. In many coordination structures of metal ions, carboxylic group bonds with monoanionic and monodentate or bidentate, electron donor amino group coordinates to metal as neutral and monodentate [16-18].

A kind of coordination complex which contain metal and organic building blocks named Metal-Organic Frameworks (MOFs), expressed by Yaghi et al. [19]. The most common application of MOFs is the gas adsorption, especially hydrogen [20]. 1, 2, or 3 dimensional coordination compounds, named MOFs, have advantages on hydrogen storage ability by adjustable pores and electrostatic potential distribution [21, 22]. Many MOFs which were reported previously, were mono ligand and less were mixed ligand complexes. However?, hydrogen storage application of modified mono or mixed ligand complexes have been investigating densely in recent years. Modification of MOFs could bein two ways, which are chemical modification and physical dispersion. Both methods may cause increment on hydrogen storage, that is why the partial charges and porosities of the host material changes by dopants [23]. Chemical modification of the MOFs was also reported as placement of inorganic groups inside the host complex. Chemically modified structures could have different crystal structures and chemical composition in comparison to the unmodified ones.

The possibility of using MOFs as hydrogen storage media have been investigated both experimentally and theoretically [24]. Both methods have advantages. For instance, the weaknesses of the theoretical methods could be solved by the experiments and also theoretical models could be validated by using experimental results. On the other hand, some details which are very hard to measure or analysis experimentally, could be collected theoretically by using simulation calculations. Many of theoretical simulation calculation for hydrogen storage capacity determination of adsorbents realized by using Monte Carlo [25] method. It is reported that the Grand Canonical Monte Carlo (GCMC) simulation calculations, which is an algorithm collection, had good correlation with the experimental results [26].

Synthesis and characterization of novel arginate complex of copper(II) metal cation studied in this work. In addition, some structural properties of the arginate complex such as molecular orbitals (HOMO; Highest Occupied Molecular Orbitals and LUMO; Lowest Unoccupied Molecular Orbitals) and density of states (DOS), and hydrogen adsorption simulation calculations realized. Molecular structure of arginine ligand was shown in Fig.1.

A similar copper complex of arginine reported

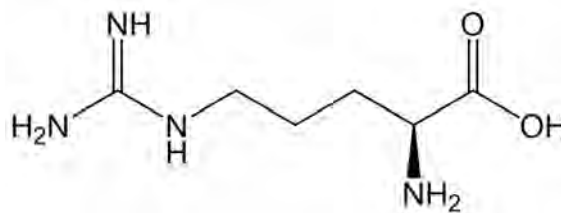


Figure 1. Arginine

previously [27]. The differences between the present work and previously reported one were the crystal structure. In the present arginine compound, free atomic sodium existed in addition to the coordinated one in the unit cell. Also the present crystal had one dimensional coordination chain while previous had molecular crystal with seconder interactions.

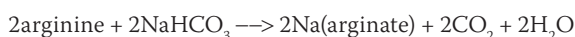
EXPERIMENTAL

Materials and measurements

The initial reactants used for synthesis were of reagent grade and CuSO₄.5H₂O, NaHCO₃ and L-arginine (Sigma-Aldrich) were used as received.

Synthesis

Firstly, sodium-arginate salt was obtained according to below reaction formula.



For the complex of copper-arginato, copper sulphate salt solution was added to salt-solution of Na-arginate and stirred for a day. The dark-blue precipitates were obtained after one month and they were filtered off and dried in air atmosphere. Chemical components of complex were summarized below in Table 1.

CuII complex contains two molecules of arginate moiety that are directly coordinated to metal ion and one mole NaSO₄⁻ that is coordinated to arginate ligand via oxygen atom of C=O group and one mole aqua ligand that is coordinated to Na(I) cation and one mole salt type free Na(I) cation. The square-planar coordination of Cu(II) metal ion was completed by two acidic carboxylic oxygen atoms and two amine nitrogen atoms from arginine. The magnetic data also support square-planar structure (Table 1).

Table 1. Analytical data of Cu(II)-complex.

Complex	MW g/mol	Yield	Contents found(calcd.) %				Color	d.p. °C	m _{eff} /BM
			C	H	N	S			
Na[Cu(Arg) ₂ NaSO ₄ (H ₂ O)] C ₁₂ H ₂₈ CuN ₈ Na ₂ O ₉ S	570	92	25.67 (25.28)	4.73 (4.96)	19.59 (19.66)	5.88 (5.62)	Dark-blue	165	1.57

Crystallography

Suitable crystal of copper complex was selected for data collection, which was performed on a STOE IPDS II diffractometer equipped with a graphite-monochromatic Mo-K α radiation ($\lambda = 0.71073\text{\AA}$) at 296 K. The structure was solved by direct-methods using SHELXS-97 [32] and refined by full-matrix least-squares methods on F2 using SHELXL-97 from within the WINGX [33] suite of software. All non-hydrogen atoms were refined with anisotropic parameters.

Water H atoms were located in a difference map and refined subject to a DFIX restraint of O-H = 0.83(2) \AA . Other H atoms were located from different maps and then treated as riding atoms with C-H distances of 0.97-0.98 \AA and N-H distances of 0.75-0.90 \AA . The following procedures were implemented in our analysis: program used for molecular graphics were as follow: MERCURY programs [34]; supramolecular analyses: PLATON [35]. Atomic coordinates have been deposited to the Cambridge Structural Database (<http://www.ccdc.cam.ac.uk>): CCDC 935805.

Hydrogen and nitrogen adsorption calculations

Hydrogen storage capacity of the arginine complex measured by using adsorption instrument (Quantachrome, Autosorb-IQ, Bayton Beach, FL) in different fugacity steps up to 1 relative pressure, experimentally. Also, the surface area and porosity calculated by using experimentally measured nitrogen adsorption data. Pore size distribution and surface area of the arginine complex calculated according to BJH method and BET theory, respectively. Then, the simulated hydrogen and nitrogen adsorption isotherms collected by using Monte Carlo methods in sorption module of Materials Studio software collection. Monte Carlo calculations realized in different 10 fugacity steps by using Metropolis method within 10 000 equilibration and production steps at 77 K. In addition, the force field, which was modified for the low temperature intermolecular interaction because of the quantum effects, used in the adsorption calculations. The details of the force field modification and the parameters explained deeply in our previous work [28,29]. The simulated model validated with the experimental surface area calculations by using Amorphous Cell module. In the amorphous cell calculations, 3*2*1 super cells dispersed in a new cubic unit to construct semi-crystalline amorphous repeated unit. The structure also been energy minimized while constructing the semi-crystalline amorphous cell

Table 3. The thermal analysis data of Cu(II)-complex.

	Na[Cu(arg) ₂ (NaSO ₄)(H ₂ O)]						Dark-Blue		
1	156-161	145	H ₂ O	4.21	3.50	Na[Cu(arg) ₂ NaSO ₄]			
2	163-810	180,207,234, 472	2 arg	65.34	67.19	CuO.Na ₂ SO ₄			
3	818-990	859	SO ₂	7.62	8.93	78.54	77.17	CuO.Na ₂ O	Black

Table 2. Some important FT-IR peaks of Cu(II)-complex.

Groups	Cu ^{II}
<i>n</i> (OH) _{H₂O}	3600-3000
<i>n</i> (NH ₂)	3417, 3149
<i>n</i> (NH ₂) _{bending}	1577
<i>n</i> (C=O) _{carbonyl}	1682
<i>n</i> (COO ⁻) _{asym}	1634
<i>n</i> (COO ⁻) _{sym}	1390
<i>Dn</i> _{as-s}	244
<i>n</i> (CH ₂)	2958
<i>n</i> (NaSO ₄ ⁻)	2877, 1121
<i>n</i> (C-N)	745-921
<i>n</i> (M-N)	469
<i>n</i> (M-O)	596

according to Monte Carlo method by using force field.

RESULTS AND DISCUSSION

Electronic Spectra

The magnetic moment, chemical composition and some properties of new product were given in Table 1. The elemental analysis indicated that complexes had two molecules of arginate ligands and one mole sulphate anion per mole formula unit. The Cu(II) complex structure has square planar geometry. High intensity peak was detected at 311 nm for CuII complex that attributed to the metal \rightarrow ligand charge transfer band. The results were agreeable to literature [14-18].

Infrared Spectra

The vibration bands of Cu(II) ion complex was summarized in Table 2. The asymmetric and symmetric stretching vibrations of aqua molecules were observed strong and broad absorption band in the range of 3600-3000 cm⁻¹. At the 3401-3149 cm⁻¹, bands were belonging to N-H stretches of primary amides. The two weak bands at the range of 2877 cm⁻¹ was attributed to the CH₂ and at the 2958 and 1121 cm⁻¹ peaks were belonging to NaSO₄⁻ group. The coordination carbonyl group, bonded to metal cations, exhibit strong bands in the region of 1682 cm⁻¹. The asymmetric vibration band of COO⁻ group was appeared at 1634 cm⁻¹, while the symmetric vibration band of COO⁻ group was at 1390 cm⁻¹. The shift (Δ) between of the ν_{asym} and ν_{sym} bands of COO⁻ group was at 244 cm⁻¹ and it was higher than monoanionic carboxylate group (158 cm⁻¹), so it could be suggested that the COO⁻ group was coordinated to metal(II) cation

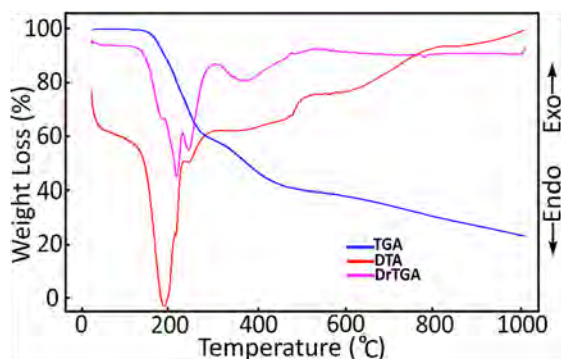


Figure 2. The TG/DTG and DTA curves of Cu(II)-complex.

as monoanionic-bidentate in this structure [30,31]. The vibration of Cu-N interaction was emerging at the 469 cm^{-1} , while ascribed to the Cu-O bands were observed at the 596 cm^{-1} [18].

Thermal Analysis

The vibration bands of Cu(II) ion complex was summarized in Table 2. The asymmetric and symmetric stretching vibrations of aqua molecules were observed strong and broad absorption band in the range of 3600–3000 cm^{-1} . At the 3401–3149 cm^{-1} , bands were belonging to N-H stretches of primary amides. The two weak bands at the range of 2877 cm^{-1} was attributed to the CH_2 and at the 2958 and 1121 cm^{-1} peaks were belonging to NaSO_4^- group. The coordination carbonyl group, bonded to metal cations, exhibit strong bands in the region of 1682 cm^{-1} . The asymmetric vibration band of COO^- group was appeared at 1634 cm^{-1} , while the symmetric vibration band of COO^- group was at 1390 cm^{-1} . The shift (Δ) between of the ν_{asym} and ν_{sym} bands of COO^- group was at 244 cm^{-1} and it was higher than monoanionic carboxylate group (158 cm^{-1}), so it could be suggested that the COO^- group was coordinated to metal(II) cation as monoanionic-bidentate in this structure [30,31]. The vibration of Cu-N interaction was emerging at the 469 cm^{-1} , while ascribed to the Cu-O bands were observed at the 596 cm^{-1} [18].

Crystallography

A summary of the crystal data, experimental details and refinement results were listed in Table 4. The crystal structure of complex with the atom labeling was shown in Fig. 3. The asymmetric unit of Cu(II) complex consisted of a Cu(II) ion, two Na(I) ions (one of them salt

Table 4. Crystal and refinement data for Cu(II)-complex.

Molecular formula	$\text{C}_{12}\text{H}_{26}\text{CuN}_8\text{Na}_2\text{O}_9\text{S}$
Molecular mass	570.00
Crystal system	Orthorhombic
Space group	$P2_12_12_1$
Unit cell parameters a, b, c, Å	7.0483(2), 12.9180(4), 25.4460(7)
V, Å ³	2316.86(12)
Z	4
ρ_{calc} g/cm ³	1.634
T, K	293
Radiation, λ, Å	MoK α ; 0.71073
Crystal size, mm	0.41x0.21x0.03
Reflections measured	22093
$\theta_{\text{min}}^{\text{max}}$ deg	1.6–27.2
Independent reflections	4495 [$R_{\text{int}} = 0.251$]
Parameters refined	290
Final R factor [$I > 2\sigma(I)$]	$R_1 = 0.104$, $wR_2 = 0.246$
GOOF	1.02
Residual electron density (min/max), e/Å ³	-0.75/0.78

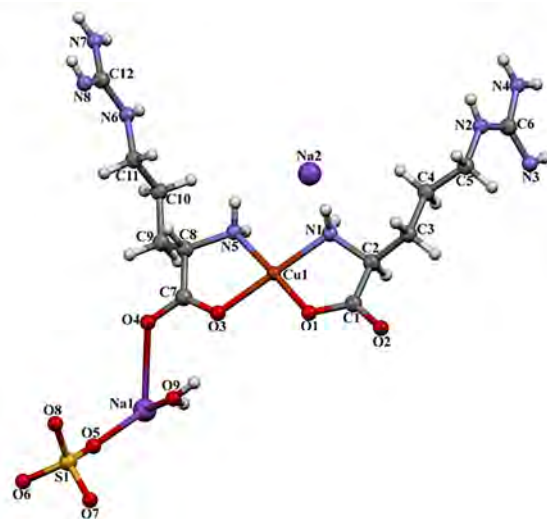


Figure 3. The molecular structure of Cu(II)-complex showing the atom numbering scheme.

type, other one is coordinated), two arginine ligands, one coordinated water molecule and one sulfate anion. The Cu1 exhibits penta-coordination with a distorted square pyramidal geometry. The equatorial coordination came from two oxygen atoms (O1 and O3) and two nitrogen atom (N1 and N5) of two different arginine ligands, while the apical position was occupied by one oxygen atom (O4ii) of different arginine ligand [(ii) $x+1/2, -y+3/2, -z+1$].

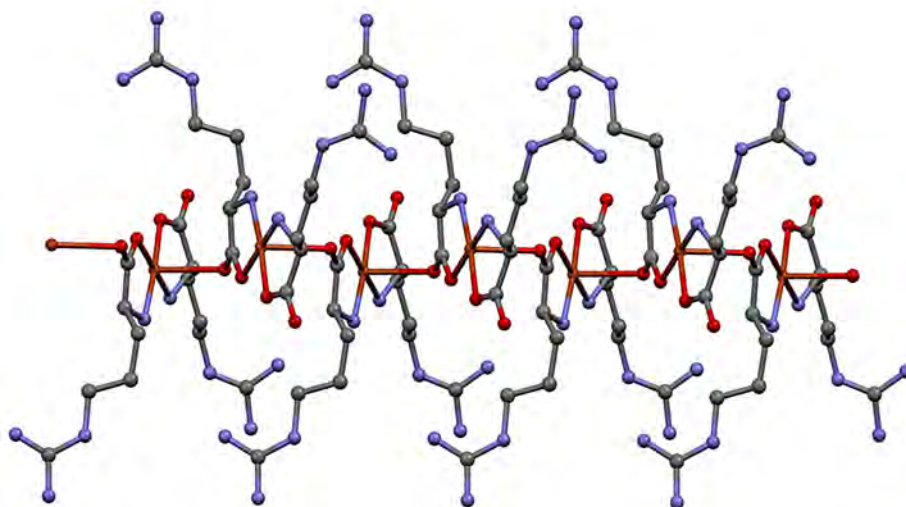
Table 5. Selected bond lengths (Å) and angles (°) for Cu(II)-complex.

Cu(1)-N(1)	1.964(10)	Cu(1)-N(5)	1.989(10)	Cu(1)-O(1)	1.931(8)
Cu(1)-O(3)	1.973(9)	Cu(1)-O(4) ⁱⁱ	2.482(8)	Na(2)-O(2)	2.755(17)
Na(1)-O(4)	2.62(3)	Na(1)-O(5)	2.84(3)	Na(1)-O(9)	2.86(3)
O(1)-Cu(1)-N(1)	84.2(4)	O(1)-Cu(1)-O(3)	93.8(3)	N(1)-Cu(1)-O(3)	177.1(4)
O(1)-Cu(1)-N(5)	175.8(4)	N(1)-Cu(1)-N(5)	98.0(4)	O(3)-Cu(1)-N(5)	84.0(4)

Symmetry codes: (i) $x+1/2, +y+1/2, +z+1$; (ii) $x+1/2, -y+3/2, -z+1$.

Table 6. Hydrogen bonds for Cu(II)-complex.

<i>D-H...A</i>	<i>D-H</i> (Å)	<i>H...A</i> (Å)	<i>D...A</i> (Å)	<i>D-H...A</i> (°)	Symmetry operations
<i>N</i> (1)- <i>H</i> (1 <i>A</i>)... <i>O</i> (5)	0.90	2.26	3.115 (14)	159	<i>x, y, z</i>
<i>N</i> (2)- <i>H</i> (2)... <i>O</i> (7)	0.86	2.05	2.900 (14)	168	$-x+1, y-1/2, -z+3/2$
<i>N</i> (3)- <i>H</i> (3)... <i>O</i> (7)	0.75	2.30	3.040 (13)	170	$-x+2, y-1/2, -z+3/2$
<i>N</i> (4)- <i>H</i> (4 <i>C</i>)... <i>O</i> (5)	0.86	2.48	3.268 (16)	153	$-x+2, y-1/2, -z+3/2$
<i>N</i> (4)- <i>H</i> (4 <i>C</i>)... <i>O</i> (7)	0.86	2.55	3.281 (15)	144	$-x+2, y-1/2, -z+3/2$
<i>N</i> (4)- <i>H</i> (4 <i>D</i>)... <i>O</i> (8)	0.86	2.05	2.890 (15)	165	$-x+1, y-1/2, -z+3/2$
<i>N</i> (5)- <i>H</i> (5 <i>C</i>)... <i>O</i> (8)	0.90	2.16	2.901 (14)	139	<i>x, y, z</i>
<i>N</i> (5)- <i>H</i> (5 <i>D</i>)... <i>O</i> (9)	0.90	1.99	2.89 (2)	178	<i>x, y, z</i>
<i>N</i> (6)- <i>H</i> (6)... <i>O</i> (6)	0.86	1.95	2.803 (18)	174	$-x+1, y+1/2, -z+3/2$
<i>N</i> (6)- <i>H</i> (6)... <i>S</i> (1)	0.86	2.81	3.526 (12)	142	$-x+1, y+1/2, -z+3/2$
<i>N</i> (7)- <i>H</i> (7 <i>B</i>)... <i>O</i> (5)	0.86	2.30	3.037 (17)	143	$-x+1, y+1/2, -z+3/2$
<i>N</i> (8)- <i>H</i> (8 <i>A</i>)... <i>O</i> (6)	0.75	2.28	2.98 (2)	156	$-x, y+1/2, -z+3/2$

**Figure 4.** An infinite 1D layer in Cu(II)-complex..

According to the Addison definition, the value of τ for Cu1 is 0.02 [$\tau = (177.10-175.80) / 60 = 0.02$], respectively ($\tau = 0$ for an ideal square-pyramid, $\tau = 1$ for an ideal trigonal-bipyramid) [36].

The Cu(II) ions were bridged by arginine ligands to generate 1D coordination polymer running parallel to the [100] direction (Fig. 4). The Cu1...Cu1ii separation was 5.778 Å. The interpenetration in Cu(II) complex was reinforced by N-H...O hydrogen bonds between the parallel 1D layers (Fig. 5.a). The Cu-N bond lengths of 1.964(10) and 1.989(10) Å were practically similar to those found in [Cu(L-Arg)₂](SO₄)·6H₂O (1.964(5) and 1.991(4) Å), [Cu(L-arg)₂(H₂O)₂](P₄O₁₂)·8H₂O (1.971(5) and 1.975(5) Å), [Cu(argininate)₂(H₂O)]CO₃·H₂O (1.977(4) and 1.991(4) Å) [37], but somewhat shorter than those found in {[Cu₂(L-arg)₂(Bpy)₂](μ2-ClO₄)₂·2ClO₄·4H₂O}n

(1.998(6) and 2.001(6) Å) [38] and [Cu₂(L-arg)₂(μ-HPO₄-O)(μ-HPO₄-O,O')(l-OH)]·(H₃O)+6H₂O (1.995(4) and 2.011(4) Å). The equatorial Cu-O bond distances (1.931(8) and 1.973(9) Å) were comparable corresponding distances found in [Cu(L-arg)₂(H₂O)₂](P₄O₁₂)·8H₂O (1.946(5) and 1.957(5) Å) [39], [Cu(argininate)₂(H₂O)]CO₃·H₂O (1.947(3) and 1.966(3) Å) [40] and trans-[Cu(l-Arg)₂(NO₃)]NO₃·3H₂O (1.936(4) and 1.956(4) Å) [41], while the axial Cu-O bond length (2.482(8) Å) was in agreement with the corresponding value in {cis-[Cu(L-Arg)₂](NO₃)₂·3H₂O}n (2.487(2) Å) [42]. Selected bond lengths and angles of structure were given in Table 5.

Atoms N2 and N4 in the molecule at (*x, y, z*) acts as hydrAtoms N2 and N4 in the molecule at (*x, y, z*) acted as hydrogen-bond donors, via atoms H2 and H4D, respectively, to atoms O7 and O8 at ($-x+1/2, -y+1, z+1/2$), so forming

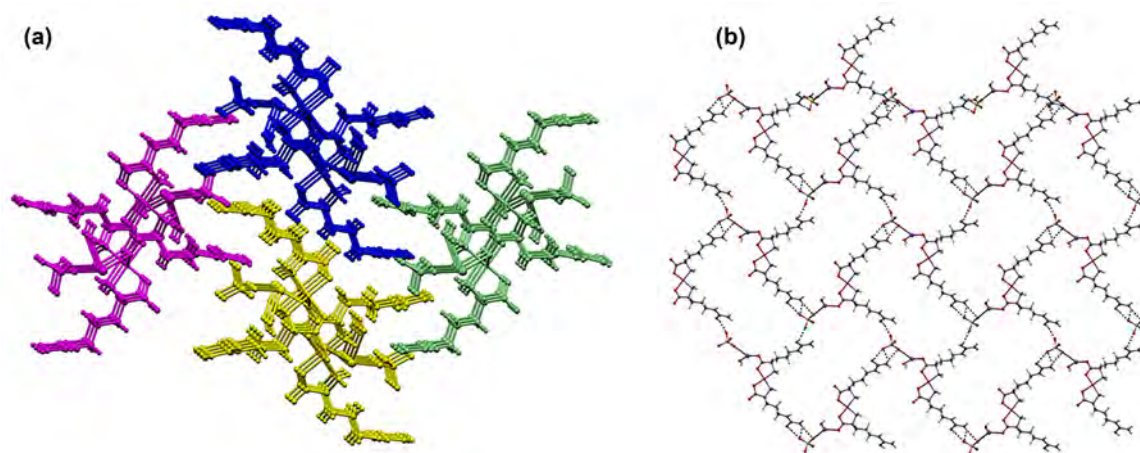


Figure 5. (a) The packing structure of Cu(II)-complex built by four interpenetrated, (b) part of the crystal structure of Cu(II)-complex, showing the N-H...O hydrogen bonds.

C(15) and C(17) [R22(8)] chains running parallel to the [001] direction. Similarly, atoms N3 and N4 in the molecule at (x, y, z) acted as hydrogen-bond donors, via atoms H3 and H4C, respectively, to atoms O7 and O5 at $(-x+3/2, -y+1, z+1/2)$, so forming C(15) and C(17) [R12(4)R21(6)] chains running parallel to the [001] direction. The combination of N-H...O hydrogen bonds produce R44(51) rings running parallel to the [111] direction (Fig. 5.b). The 1D coordination polymer was extended into a three-dimensional frameworks by N-H...O hydrogen bonds (Table 6).

Hydrogen and nitrogen adsorption capacities

BET surface area and pore size distribution of the arginine complex calculated and the plots given in Figure 6. Experimental and simulated nitrogen adsorption

isotherms showed Type-III isotherms according to IUPAC classification. The type of isotherms represented micro and meso-porosity existence, in addition adsorbed multilayer formation. Micro and meso-porosity were clearly shown in the pore size distribution plot in Figure 6b. It was also understood that the arginine complex have bigger meso-pores in comparison to micro-pores. Calculated BET surface area was $0.533 \text{ m}^2/\text{g}$ that could be approved as the structure had small porosity when the value compared to surface areas of the common MOFs.

The simulated and experimental nitrogen adsorption isotherms were similar. While constructing semi crystalline amorphous cell by using relaxed $2 \times 1 \times 1$ non-periodic super structure (Figure 7.a), different densities collected but the final structure with 1.3426 g/ml selected as the finest model, which represent the real complex. Crystal density of synthesized complex was 1.5824 g/ml , so the close densities investigated. Semi crystalline amorphous cell used because the crystal structure that was simulated by using cif (crystal information file) did not have any empty spaces. Hence the crystal structure was not able to adsorb both hydrogen and nitrogen. It was shown that the materials used for experimental gas adsorption measurements, had crystal cracks and deformed crystal structures. That is why, representing structure in amorphous cell with crystal building units was wise. Final structure that was used for gas adsorption calculations represented in Figure 7.b. Yellow dots in Figure 7.b represents the surfaces that the hydrogen molecules could be stored. It was also shown that the spaces which possibly uptake hydrogen molecules were small.

Hydrogen molecules in the amorphous cell after adsorption process simulated and given in Figure 8. Green ellipsoids represent the hydrogen molecules.

Hydrogen adsorption isotherms of arginine complex

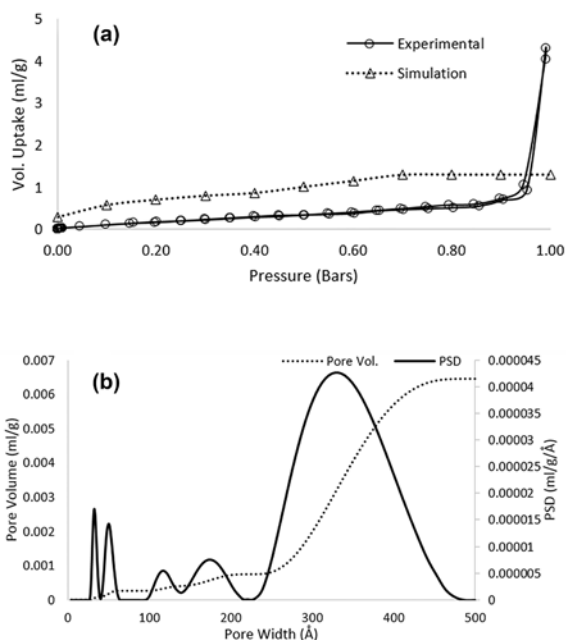


Figure 6. (a) Simulated and experimentally collected nitrogen adsorption isotherms and (b) pore size distribution of arginine complex.

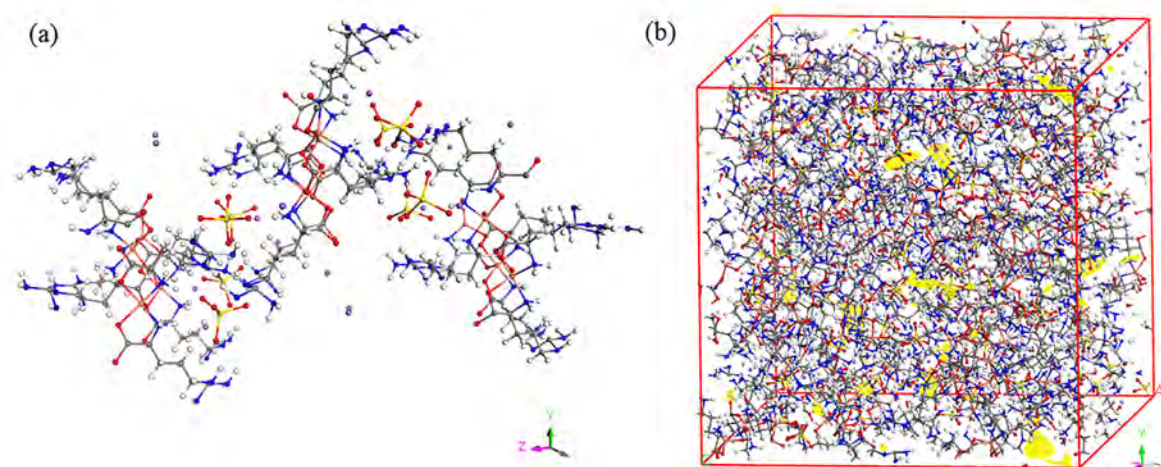


Figure 7. (a) 2x1x1 relaxed unit and (b) relaxed 10 unit included semi-crystalline amorphous cell.

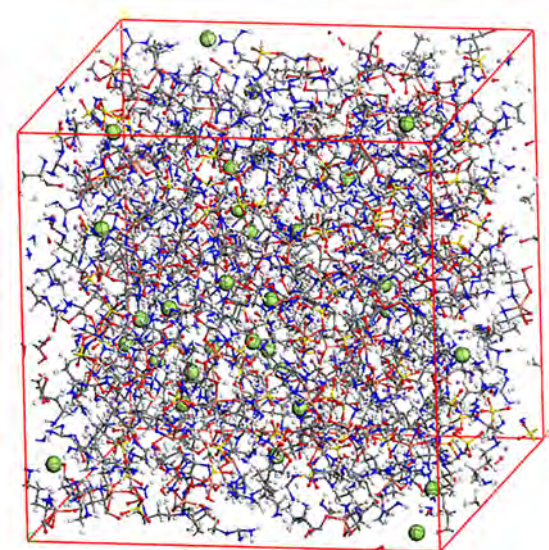


Figure 8. Hydrogen adsorbed arginine structure.

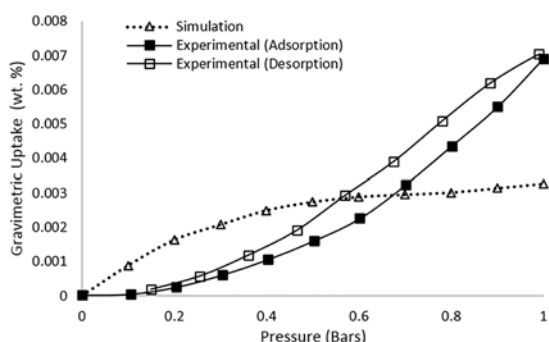


Figure 9. Experimental and simulated hydrogen adsorption isotherms.

both experimental and simulation was given in Figure 9. It was clear that the hydrogen storage adsorption isotherm types differed for simulation and experimental measurements. The main reason of the situation would be the possible residue in the experimental materials.

In addition, Monte Carlo calculation could be failed in such small porosity because the force field used for the calculations could not meet the cutoff accuracy for the calculations.

The final hydrogen storage capacity of the arginine complex was $6.92\text{E-}3$ wt. % at 77 K and 1 bar while simulated value was $3.27\text{E-}3$ wt. % for the same conditions. In the previous work, different arginine complex was synthesized and also the hydrogen storage capacity was measured. It was found that the previous arginine compound could be adsorbed approximately 0.8 wt. % hydrogen at 77 K and 1 bar pressure [28,29]. The value was 10 times bigger than the present work because the molecular spaces in the present work filled with the free and coordinated sodium and sulfite molecules.

CONCLUSION

The new arginine metal complex “sodium[(sodium(I) sulphate-monoaqua) (bisarginato- κ -O, κ -N) copper(II)]” was synthesized and characterized as structural. The unit cell of complex included two mole arginato and one mole aqua ligands, one mole sodium(I) and copper(II) cations, one mole sulphate anion. One mole sodium cation was settled outside of the unit cell as counter ion. The geometry of complex was square-planar so violence of electronic transitions was weak. The structure of complex was thermally stable until 165°C. The infrared results explained bonding properties of arginine ligands. Both experimental and simulation calculations showed that the hydrogen storage capability of the arginine complex decreased because the empty spaces filled free and coordinated sodium and sulfite molecules. In conclusion, other possible arginine complexes could be investigated to improve hydrogen storage capacity.

ACKNOWLEDGEMENTS

This research was supported by the Science Research Department of Hitit University (Project no: FEF03.12.05).

REFERENCES

1. Cotton FA, Day VW, Hazen EE Jr, Larsen S, Wong STK. Structure of bis(methylguanidinium) monohydrogen orthophosphate. Model for the arginine-phosphate interactions at the active site of staphylococcal nuclease and other phosphohydrolytic enzymes. *J. Am. Chem. Soc.* 96 (1974) 4471–4478.
2. Patthy L, Smith EL. Reversible modification of arginine residues. Application to sequence studies by restriction of tryptic hydrolysis to lysine residues. *J. Biol. Chem. Soc.* 250(2) (1975) 557–564.
3. Lippard SJ, Berg JM. Principles of bioinorganic chemistry, (University Science Books), Mill Valley, CA, 1994.
4. Stone DL, Smith DK, Whitwood AC. Copper amino-acid complexes—towards encapsulated metal centres. *Polyhedron* 23 (2004) 1709–1717.
5. Ohata N, Masuda H, Yamauchi O. Aromatic carboxylate-controlled self-organization of copper(II)-L-arginine complexes. *Inorg. Chim. Acta* 286(1) (1999) 37–45.
6. Hamilton AD. Supramolecular control of structure and reactivity, Wiley, Chichester, 1996.
7. Stanila A, Marcu A, Rusu D, Rusu M, David L. Spectroscopic studies of some copper(II) complexes with amino acids. *J. Mol. Struct.* 834–836 (2007) 364–368.
8. Iqbal MZ, Khurshid S, Iqbal MS. Antibacterial activity of copper-amino acid complexes. *J. Pak. Med. Assoc.* 40(9) (1990) 221–222.
9. Venelinov T, Arpadjan S, Karadjova I, Beattie J. Properties of the copper(II)-histidine complex obtained after dialysis of human plasma with histidine. *Acta Pharm.* 56 (2006) 105–112.
10. Sorensen JRJ, Sigel H. Metal Ions in Biological Systems, Marcel Dekker, New York, Vol. 14, p.77. 1982.
11. Kato M, Muto Y. Factors affecting the magnetic properties of dimeric copper(II) complexes. *Coord. Chem. Rev.* 92 (1988) 45–83.
12. Nagar R. Synthesis, spectral characterization and DNA bindings of tridentate N₂O donor Schiff base metal(II) complexes. *J. Inorg. Biochem.* 40 (1990) 349–356.
13. Cavigliolo G, Benedetto L, Boccaleri E, Colangelo D, Viano I, Osella D. Pt(II) complexes with different N-donor aromatic ligands for specific inhibition of telomerase. *Inorg. Chim. Acta* 305 (2000) 61–68.
14. Öztürkkan EF, Köse DA, Necefoglu H, Uzun I. Synthesis and characterization of bis(N,N-diethylnicotinamide) p-halogenobenzoate complexes of Co(II). *Asian J. Chem.* 19(6) (2007) 4880–4888.
15. Köse DA, Gökçe G, Gökçe S, Uzun I. bis(N,N-diethylnicotinamide) p-chlorobenzoate complexes of Ni(II), Zn(II) and Cd(II). *J. Therm. Anal. Cal.* 95(1) (2009) 247–251.
16. Köse DA, Ay AN, Şahin O, Büyükgüngör O. A mononuclear Zn(II) complex of mixed ligands with both fivefold- and sixfold- coordinations in the same framework. *J. Iran. Chem. Soc.* 9(4) (2012) 591–597.
17. Köse DA, Necefoglu H, Sahin O, Büyükgüngör O. Synthesis, spectral, thermal and structural study of monoaquabis(acetylsalicylato-κO)bis(nicotinamide-κN)copper(II). *J. Chem. Crystallogr.* 41 (2011) 297–305.
18. Köse DA, Zumreoglu-Karan B, Unaleroglu C, Sahin O, Buyukgungor O. Synthesis and characterization of transition metal-vitamin B13 complexes with a Co-vitamin. *J. Coord. Chem.* 789 (2006) 147–151.
19. Yaghi OM, Li H, Groy TL. Construction of porous solids from hydrogen-bonded metal complexes of 1,3,5-benzenetricarboxylic acid. *J. Am. Chem. Soc.* 118(38) (1996) 9096–9101.
20. Rosi NL, Eckert J, Eddaoudi M, Vodak DT, Kim J, O’Keeffe M, Yaghi OM. Hydrogen storage in microporous metal-organic frameworks. *Science* 300(5622) (2003) 1127–1129.
21. Seo JS, Whang D, Lee H, Im Jun S, Oh J, Jeon YJ, Kim K. A homochiral metal-organic porous material for enantioselective separation and catalysis. *Nature* 404(6781) (2000) 982–986.
22. Sagara T, Klassen J, Ganz E. Computational study of hydrogen binding by metal-organic framework-5. *J. Chem. Phys.* 121(24) (2004) 12543–12547.
23. Baykasoglu C, Ozturk Z, Kirca M, Celebi AT, Mungan A, To AC. Effects of lithium doping on hydrogen storage properties of heat welded random CNT network structures. *Int. J. Hyd. Energy* 2016, 41(19), 8246–8255.
24. Ozturk Z, Baykasoglu C, Kirca M. Sandwiched graphene-fullerene composite: A novel 3-D nanostructured material for hydrogen storage. *Int. J. Hyd. Energy* 41(15) (2016) 6403–6411.
25. Vlachy V, Ichiye T, Haymet ADJ. Symmetric associating electrolytes: GCMC simulations and integral equation theory. *J. Am. Chem. Soc.* 113(4) (1991) 1077–1082.
26. Pham T, Forrest KA, Hogan A, Tudor B, McLaughlin K, Belof JL, Eckert J, Space B. Understanding hydrogen sorption in In-soc-MOF: A charged metal-organic framework with open-metal sites, narrow channels, and counterions. *Cryst. Growth & Design* 15(3) (2015) 1460–1471.
27. Köse DA, Toprak E, Kaşarçı A, Avcı E, Avcı GA, Şahin O, Büyükgüngör O. Synthesis, spectral, thermal studies of Co(II), Ni(II), Cu(II) and Zn(II)-arginato complexes. Crystal structure of monoaquabis(arginato-κO, κN)copper(II). [Cu(arg)₂(H₂O)].NaNO₃, *J. Chin. Chem. Soc.* 61 (2014) 881–890.
28. Ozturk Z, Kose DA, Asan A, Ozkan G. Porous metal-organic Cu(II) complex of L-Arginine; synthesis, characterization, hydrogen storage properties and molecular simulation calculations. *Hittite J. Sci. & Eng.* 1(1) (2014) 1–5.
29. Ozturk Z, Ozkan G, Kose DA, Asan A. Experimental and simulation study on structural characterization and hydrogen storage of metal organic structured compounds. *Int. J. Hyd. Energy* 41(19) (2016) 8256–8263.

30. Köse DA, Necefoglu H, Icbudak H. Synthesis and characterization of N,N-diethylnicotinamide-acetylsalicylato complexes of Co(II), Ni(II), Cu(II), and Zn(II). *J. Coord. Chem.* 61(21) (2008) 3508–3515.
31. Köse DA, Necefoglu H. Synthesis and characterization of bis(nicotinamide) m-hydroxybenzoate complexes of Co(II), Ni(II), Cu(II) and Zn(II). *J. Therm. Anal. Cal.* 93(2) (2008) 509–514.
32. Farrugia LJJ. WinGX suite for small-molecule single-crystal crystallography. *Apply. Cryst.* 32 (1999) 837–838.
33. Sheldrick GM. A short history of SHELX. *Acta Cryst. A64* (2008) 112–122.
34. Mercury, version 3.0; CCDC, available online via ccdc.cam.ac.uk/products/mercury.
35. Spek AL. PLATON—a multipurpose crystallographic tool. Utrecht University, Utrecht (2005).
36. Addison AW, Rao TN, Reedijk J, Rijn JV, Verschoor GC. Synthesis, structure, and spectroscopic properties of copper(II) compounds containing nitrogen-sulphur donor ligands; the crystal and molecular structure of aqua[1,7-bis(N-methylbenzimidazol-2'-yl)-2,6-dithiaheptane] copper(II) perchlorate. *J. Chem. Soc. Dalton Trans.* (1984) 1349–1356.
37. Ohata N, Masuda H, Yamauchi O. Dianion-controlled supramolecular assembly of copper(II)-arginine complex ion. *Inorg. Chim. Acta* 749 (2000) 300–302.
38. Hemissi H, Nasri M, Abid S, Al-Deyab SS, Dhahri E, Hlil EK, Rzaigui M. Crystal structure, spectroscopic, magnetic and electronic structure studies of a novel Cu(II) amino acid complex $[\text{Cu}(\text{L-arg})_2(\text{H}_2\text{O})_2](\text{P}_4\text{O}_{12}) \cdot 8\text{H}_2\text{O}$. *J. Solid State Chem.* 196 (2012) 489–497.
39. Viera I, Torre MH, Piro OE, Castellano EE, Baran EJ. Structural and spectroscopic characterization of aqua-diargininate-copper(II)-carbonate monohydrate. *J. Inorg. Biochem.* 99(5) (2005) 1250–1254.
40. Zhou X, Yang C, Le X, Chen S, Liu J, Huang Z. Synthesis and crystal structures of one-dimensional ClO bridged coordination polymers: $\{[\text{Cu}(\text{Bpy})_2(\mu^2\text{-ClO}_4)] \cdot \text{ClO}_4\}_n$ and $\{[\text{Cu}_2(\text{L-arg})_2(\text{Bpy})_2(\mu^2\text{-ClO}_4)_2] \cdot 2\text{ClO}_4 \cdot 4\text{H}_2\text{O}\}_n$. *J. Coord. Chem.* 57(5) (2004) 401–409.
41. Santana RC, Carvalho JF, Vencato I, Napolitano HB, Bortoluzzi AJ, Barberis GE, Rapp RE, Passeggi MCG, Calvo R. Synthesis, crystal structure and magnetic properties of a new dinuclear copper(II) amino acid complex $[\text{Cu}_2(\text{L-arg})_2(\mu\text{-HPO}_4\text{-O})(\mu\text{-HPO}_4\text{-O,O}')(\mu\text{-OH})] \cdot (\text{H}_3\text{O})^+ \cdot (\text{H}_2\text{O})_6$. *Polyhedron* 26(17) (2007) 5001–5008.
42. Hu R, Yu Q, Liang F, Ma L, Chen X, Zhang M, Liang H, Yu K. Syntheses and crystal structures of cis- and trans-copper(II) complexes of L-arginine. *J. Coord. Chem.* 61 (2008) 1265–1271.

Experimental Analysis of Laminar Flow and Heat Transfer in a Multi-Port Finned Minichannel

Berk Çevrim¹, Almıla Güvenç Yazıcıoğlu², Sadık Kakaç¹

¹ TOBB University of Economics and Technology, Department of Mechanical Engineering Ankara, TURKEY

² Middle East Technical University, Department of Mechanical Engineering Ankara, TURKEY

ABSTRACT

Due to their high heat transfer rate, small scale channels have been a popular area of study for the past three decades, especially for heat exchangers. In this study, fluid flow and heat transfer in a multi-port finned minichannel with a rectangular cross section was investigated experimentally under the constant heat flux boundary condition. The minichannel, which has a length of 638 mm, consists of 16 ports, 14 of which are identical finned rectangular channels with a width of 2.10 mm and a height of 5.85 mm while the remaining two ports at the outer edges of the channel were considered to be identical with the other ports. Deionized water was used as the working fluid with Reynolds number ranging between 75 and 190 in a single port. In order to correctly evaluate local heat transfer and friction coefficient values, thermal entrance effects and varying thermo-physical properties of the working fluid were taken into consideration throughout the study. Local Nusselt number varying with dimensionless axial thermal length, friction factor and average Nusselt number values varying with Reynolds number, and temperature distribution along the wall were evaluated to study fluid flow and heat transfer of the finned minichannel. The results were compared to theoretical values and presented graphically. Local Nusselt number values indicated fairly good agreement with theory while friction factor was overestimated. This was considered to be due to the effect of fins. In addition, three correlations were suggested in order to evaluate friction factor, local Nusselt number and average Nusselt number for the minichannel in given ranges of parameters.

Article History:

Received: 2016/05/02

Accepted: 2015/06/23

Online: 2016/06/30

Correspondence to: Sadık Kakaç, TOBB

University of Economics and Technology,

Department of Mechanical Engineering

Ankara, TURKEY

Tel: +90 (312) 2924087

Fax: +90 (312) 292 4091

E-Mail: skakac@etu.edu.tr

Key Words:

Fin; Convective Heat Transfer; Laminar; Multi-Port; Nusselt Number

NOMECLATURE

A_c	channel port cross-section area, m ²	m	mass flow rate, kg/s
A_{ht}	channel heated area, m ²	Nu	Nusselt number
a	channel port width, m	P_w	wetter perimeter, m
b	channel port height, m	Pr	Prandtl number
C	constant	ΔP	total pressure difference, Pa
c	fin height, m	PEC	performance evaluation criteria
c_p	specific heat capacity, J/kg K	Q	total rate of heat gained by fluid, W
D	diameter, m	q	heat flux, W/m ²
d	fin width, m	R	indirectly measured parameter
e	port wall thickness	Re	Reynolds number
f	friction factor	T	Temperature, °C
G	volumetric flow rate, m ³ /s	u	velocity, m/s
Gz	Graetz number	x	axial distance, m
L	length, m	x^*	dimensionless thermal axial distance

γ directly measured parameter

Greek symbols

α aspect ratio (b/a)
 α_c aspect ratio (a/b)
 ε relative roughness
 μ dynamic viscosity, Pa s
 ρ density, kg/m³
 ω uncertainty

Subscripts

exp experimental
i inlet
f fluid
h hydraulic
m mean
o outlet
t thermal
theo theoretical
w wall
x local

INTRODUCTION

With the rapid development of MEMS (micro electro mechanical systems), high amounts of heat have to be dissipated from these systems. The initial studies began with Tuckerman and Pease [1], who tested their compact silicon substrate with an integral part and indicated that up to 790 W/cm² heat dissipation could be achieved. This encouraged researchers to investigate fluid flow and heat transfer characteristics in small scale channels. Consequently, those researches contributed to the area of heat exchangers. Even though there are numerous papers published about heat transfer in small scales, a few of them cover the gap of minichannels, which are neither micro- nor conventional channels, but in between [2,3].

Wang et al. [4] both experimentally and numerically investigated friction and heat transfer characteristics in a trapezoidal microchannel using deionized water with the constant heat flux boundary condition, neglecting axial heat conduction. They found good agreement between their experimental data and numerical predictions, showing that classical Navier-Stokes approach was valid in hydraulic diameters as low as 155 μm . Their numerical results also indicated that thermal entry length and fully developed Nusselt number for a trapezoidal cross sectional channel with bottom heating are $z = 0.15 \cdot \text{Re} \cdot \text{Pr} \cdot D_h$ and $\text{Nu} = 4.00$, respectively.

Gunnasegaran et al. [5] investigated the effects of geometric parameters on thermohydraulic performance of microchannel heat sinks with Reynolds number ranging

between 100-1000. Their study mainly focused on triangular, trapezoidal, and rectangular cross sectional geometries. Results showed that between these three geometries, the rectangular channel showed the highest friction factor and heat transfer rate, while the triangular channel had the lowest, with the trapezoidal channel in between. They specifically pointed out that width to height ratio of rectangular channels has a major influence on Poiseuille number. Moreover, for the rectangular channel, the smaller the hydraulic diameter gets, the greater the value of the heat transfer coefficient is.

Wu and Cheng [6] experimentally investigated laminar convective heat transfer and pressure drop of water flow in trapezoidal microchannels with various surface conditions. They found out that the Nusselt number values and friction coefficient greatly depends on geometrical parameters of the channel which is considered more important than surface roughness and surface hydrophilic property. Experimental results indicated that at low Reynolds numbers ($\text{Re} < 100$), Nusselt number increases sharply and is practically linear with Reynolds number, while the rate of Nu to Re gradually decreases as Reynolds number passes the value of 100. Afterwards, a numerical study was conducted by Zhuo et al. [7] to show the applicability of the former study by using field synergy principle. It was found that Navier-Stokes and energy equations with no-slip boundary condition can be used to predict thermohydraulic performances of fluid flow for hydraulic diameter as low as tens of micrometers with reasonable accuracy. They also indicated for the two microchannels they analyzed, fully developed Nusselt number increases with the increase of Reynolds number differing from conventional theory where fully developed Nusselt number is constant.

Hetsroni et al. [8,9] compared experimental data available in literature with theory and numerical results to investigate fluid flow and heat transfer characteristics in microchannel. In their fluid flow study, it was concluded that Poiseuille number is independent of Reynolds number for single phase fluid flow in smooth microchannels with hydraulic diameter varying from 15 to 4010 μm in laminar region. Additionally, flow behavior in microchannels with hydraulic diameters as small as 50 μm showed no difference from macroflow. Heat transfer studies indicated that axial conduction in both fluid and the wall has a significant effect on heat transfer in microchannels. Thus, it was suggested to use the exact model in numerical applications in order to evaluate correct variation of Nusselt number.

Lee et al. [10] conducted an experimental investigation to find out the validity of classical correlations used in conventional sized channels to evaluate thermal behavior of rectangular microchannels. Deionized water was used

as working fluid. Reynolds number and hydraulic diameter varied between 300-3500 and 318-903 μm . Numerical analysis was also carried out to verify their work. Numerical results showed good agreement with experimental data (average deviation of 5%), suggesting that classical continuum approach can be used to predict heat transfer behavior of microchannels with dimension in given range. The results also confirmed that instead of full 3D conjugate analysis, a simplified this wall analysis can be employed as an alternative to decrease computational time.

Also, several reviews were conducted by various researchers [11,12] about flow and heat transfer characteristics in small scale channels. Their research consist of vast amount of experimental and numerical data. They conclude that, although most of liquid flow investigations agree well with conventional theory, there are still numerous amount of studies that deviate significantly, either over or under predict, especially on friction coefficient. They predict that, due to improvement on manufacturing and measuring technology, therefore reduction on surface roughness and having control over hydraulic diameter, older studies might not provide accurate comparison as thermohydraulic properties of small scale channels greatly depend on geometry. Another review was done by Rosa et al. [13] which is focused on scaling effects in small scale channels. They recommended that, although classical theories are reliable to predict friction factor and heat transfer characteristics, scaling effects should be accounted for accurate results.

Considering the abovementioned literature review, more research should be done in small scale channels to further prove their applicability to the theory. Additionally, while most of the authors focused on simple geometries to clarify the approaches, a few of them considered the effects of fins. Therefore, an experimental investigation of heat transfer and fluid flow characteristics in a multi-port finned minichannel with rectangular cross section was conducted under various constant heat flux rates. Reynolds number ranged from 75 to 190 in a single port. In order to correctly evaluate local heat transfer and friction coefficient values, the effect of thermal entrance and varying thermo-physical properties of the working fluid were taken into consideration. Specifically, a finned multiport rectangular channel was chosen due to their applicability in industry, therefore, experimental analysis of the channel would provide assistance for heat exchanger design.

EXPERIMENTAL SETUP

Test Facility

A schematic illustration of the test facility, which is

composed of a cooling bath (Cole Parmer®, KH-13500-30), a by-pass line, a control valve, a gear pump (Cole Parmer®, KH-74014-55), a flowmeter (Flowtech®, DK800S-6), thermocouples (Cole Parmer®, KH-08542-04, T type), resistance temperature detectors (Cole Parmer®, KH-08117-80), a differential pressure transmitter (Validyne®, 1-N-1-28-S-4-A) and the test section, is given in Fig. 1a.

The working fluid is stored and cooled in constant temperature cooling bath. Cooling bath consists of its own pump, which extends the maximum flowmeter limit. Thus, a by-pass line was implemented to the circuit from the outlet to the inlet of the bath in order to reduce the flow rate. Joint use of control valve and gear pump is used to stabilize fluid pressure in addition to adjusting the flow rate to the desired value by manually increasing or decreasing the flow area and rpm, respectively. Once the fluid passes the flowmeter, where adjusted flow rate is visually measured, it reaches test section.

Test Section

The test section consist of heating layer and test channel.

Heating Layer

The heating layer can be seen in Fig. 1c. The test section is designed to apply constant heat flux on the minichannel. In order to achieve this condition, a thin bronze bar was wrapped with dielectric tape and resistance wire was stationed on it. Thus, electric current was ensured not to flow through bronze bar. Figure 1b. shows the thermocouple locations along the channel. They are 70 mm apart from one another except the first one at the inlet, which is 25 mm apart from the channel edge. As they were likely to get affected by the temperature of bronze bar and give inaccurate results, a thin mica layer was placed between the bronze bar and the minichannel. This whole process posed small gaps between layers, hence increased thermal resistance. In order to prevent this problem, a wooden stock was put on top of the heating section, then compressed with clamps and the whole system was isolated. Table 1 lists the material properties in the heating layer.

Table 1. Material properties in heating layer

Materials	Thickness[mm]	k[W/m K]
Glass Wool	30	0.031
Wooden Stock	15	0.13
Resistance Wire	0.5	[-]
Bronze Bar	1	401
Mica	0.5	0.3
Minichannel	0.44	237

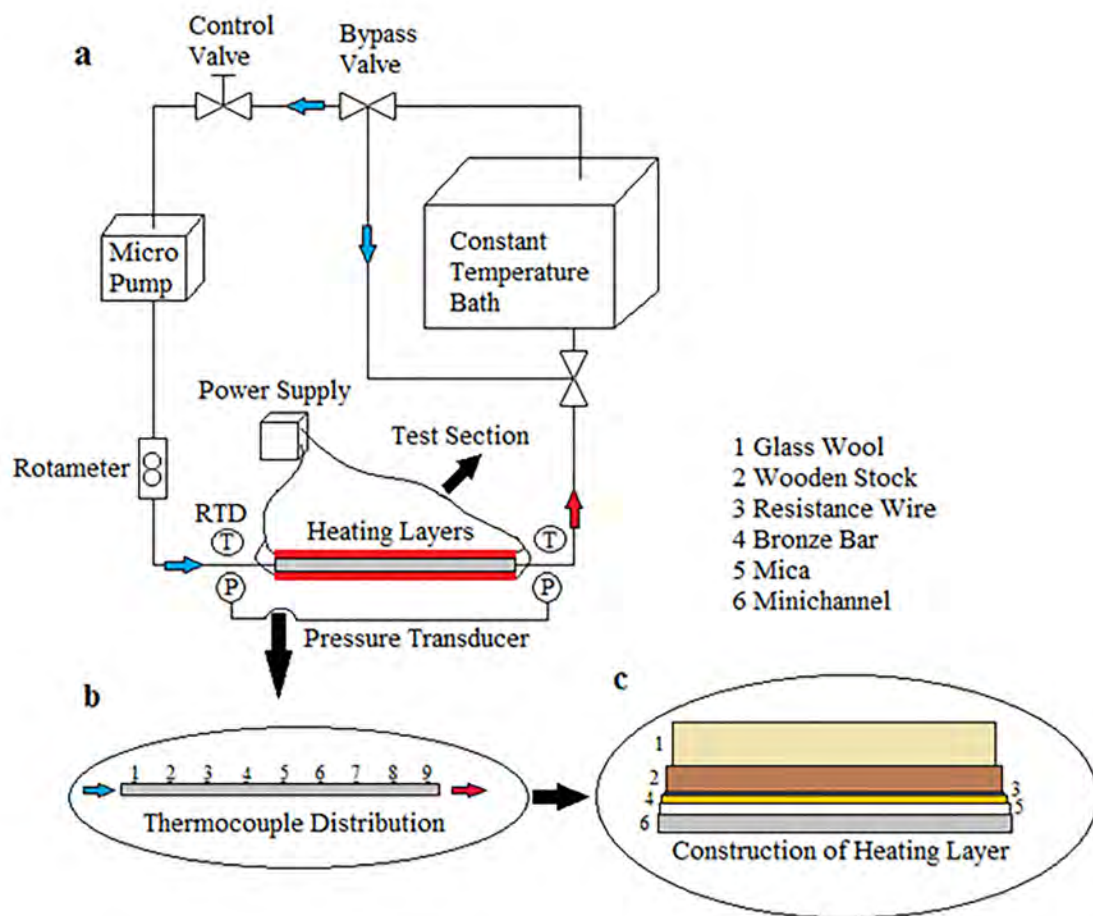


Figure 1. (a) Schematic representation of test facility (b) Thermocouple distribution along test channel wall (c) Heating layer materials and construction

Test Channel

A visual representation of the minichannel cross section is given in Fig. 2. The minichannel consists of 16 ports, 14 of which are identical to each other. The remaining 2

ports at the outer edges are considered to be similar to the others for convenience. Geometrical specifications of the channel are provided in Table 2.

Manifold design is stated as an important problem considering the working fluid is desired to flow in each port with equal velocity [14]. Therefore, manifolds are designed by means of FLUENT®. Average axial velocity at the ports on the edge of microchannel inlet have relative error of 13%.

Table 2. Geometrical specifications of the channel.

Parameters	Definitions	Values
L [mm]	Length of the channel	638
W [mm]	Width of the channel	38.05
H [mm]	Height of the channel	6.73
a [mm]	Width of the port	2.10
b [mm]	Height of the port	5.85
c [mm]	Height of the fin	0.87
d [mm]	Width of the fin	0.25
e [mm]	Channel port thickness	0.25

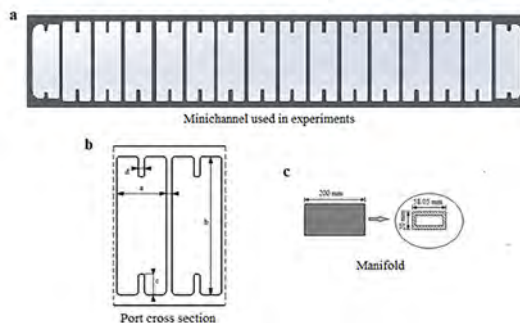


Figure 2. (a) Minichannel (b) Cross section of the port (c) Manifold

The reason behind this is that, those ports are not identical with inner ports, although they are assumed identical throughout the study. Remaining ports have average relative error of 3%, which is practical. In each manifold, 2 holes are drilled to implement differential pressure transducer and resistance temperature detectors. By doing so, pressure difference between inlet and outlet manifolds, inlet and outlet temperature of the fluid was measured.

Experimental Method

Before starting the experiments, data logger and power supply are turned on. The control valve is opened fully to allow the working fluid to flow through the test section. After preliminary preparations, constant temperature bath and micro pump are turned on. The fluid maintained in the constant temperature bath is cooled to the desired temperature by manually adjusting the bath setting. After fluid temperature stabilizes, control valve is gradually closed and flowmeter is constantly checked in order to ensure that desired flow rate value is approximately achieved. Afterwards, the micro pump is used to adjust the flow rate to the exact desired value by increasing or decreasing the flow rate by small amounts. Then, current and voltage values are adjusted from the power supply to initiate heating at the test section. Temperature and pressure readings are started visualized in the computer and recorded. In approximately 20 minutes, steady state is achieved. The temperature and pressure data are digitally recorded through the data acquisition unit every 10 seconds for 15 minutes. For each repeated experiment, above mentioned procedure is followed.

DATA ANALYSIS

Data Reduction

Calculations were performed using conventional equations [15,16]. Mass flow rate is calculated through the measured volume flow rate and water density.

$$m = G \cdot \rho \quad (1)$$

Average Reynolds number in one port is defined as below.

$$\text{Re} = \frac{1}{16} \frac{m \cdot D_h}{A_c \cdot \mu} \quad (2)$$

Where A_c is the cross sectional area of a channel port. Hydraulic diameter and aspect ratio is defined, respectively, as follows.

$$D_h = \frac{4 \cdot A_c}{P_w} \quad (3)$$

$$\alpha = \frac{b}{a}, \alpha_c = \frac{1}{\alpha}, 0 < \alpha_c < 1 \quad (4)$$

Hydrodynamic development length, thermal development length and dimensionless axial thermal development length for rectangular cross sectional channels in laminar region were calculated, respectively, as:

$$L_h = 0.05 \cdot D_h \cdot \text{Re} \quad (5)$$

$$L_t = 0.1 \cdot D_h \cdot \text{Re} \cdot \text{Pr} \quad (6)$$

$$x^* = \frac{x}{\text{Re} \cdot \text{Pr} \cdot D_h} \quad (7)$$

Friction factor was calculated including entrance and exit losses.

$$f = \frac{1}{2} \frac{D_h}{L} \frac{\Delta P}{\rho \cdot u_m^2} \quad (8)$$

ΔP is the pressure difference measured by the differential pressure transmitter. Heat transferred to the fluid, which is total heat transferred throughout the test section, is given as:

$$Q = m \cdot c_p \cdot (T_{f,o} - T_{f,i}) \quad (9)$$

$T_{f,i}$ and $T_{f,o}$ are the inlet and outlet temperature of the working fluid, which are measured by resistance temperature detectors. The heat flux is calculated by dividing by the channel heating area, A_{ht} :

$$q = \frac{Q}{A_{ht}} \quad (10)$$

Longitudinal temperature of the fluid in the test section is assumed to be varying linearly and calculated as follows:

$$T_f(x) = T_{f,i} + (T_{f,o} - T_{f,i}) \cdot \frac{x}{L} \quad (11)$$

The local heat transfer coefficient is defined as:

$$h(x) = \frac{q}{[T_w(x) - T_f(x)]} \quad (12)$$

Where, $T_w(x)$ are the temperature measurements along the wall via thermocouples. The local Nusselt number is defined as:

$$Nu(x) = \frac{h(x) \cdot D_h}{k_f(x)} \quad (13)$$

Average Nusselt number is calculated by taking the mean value of nine local Nusselt number values for each experiment.

$$Nu_m = \frac{1}{9} \sum Nu(x) \quad (14)$$

An add-in, which is generated using industrial standard IAPWS-IF97, is used to calculate thermophysical properties of the fluid at required temperatures. In order to validate the accuracy of the program, $k_f(x)$ values were compared with tabular values [17] and maximum relative difference was found to be %0.87 [18].

Uncertainty

In this study, uncertainty analysis is done according to reference [19].

$$R = R(y_1, y_2, y_3, \dots, y_n)$$

$$\omega_R = \left[\left(\frac{\partial R}{\partial y_1} \omega_1 \right)^2 + \left(\frac{\partial R}{\partial y_2} \omega_2 \right)^2 + \dots + \left(\frac{\partial R}{\partial y_n} \omega_n \right)^2 \right]^{1/2} \quad (15)$$

Where, ω_R is the uncertainty in the result, y_1, y_2, \dots, y_n are independent variables, and $\omega_1, \omega_2, \dots, \omega_n$ are uncertainties in the independent variable. Operating conditions of the system and uncertainty of major parameters are provided in Table 3.

As it can be seen in Table 3, uncertainties related to hydraulic performance of the flow are higher than usual. Geometrical parameters are the major cause of this phenomenon. Since the channel is miniscale, conventional measurements techniques are used to evaluate the parameters. However, increasing accuracy of measurement, for instance by using electron microscopy, will provide lower uncertainties, thus more accurate results.

RESULTS AND DISCUSSIONS

In this study, the flow is known to be in laminar region, since Reynolds number varied between 75 and 190 in a single port. In the graphically presented data, there were no significant slope changes in experimental data for friction factor and average Nusselt number before $Re = 190$. Therefore, only laminar flow evaluations are done for both friction and heat transfer characteristics.

In order to experimentally determine viscous heating, at first, inlet temperature of the test section was

maintained at 20°C without heating. It was observed that the temperature difference between the inlet and the outlet of the test section was less than 0.1°C, which indicated that viscous heating could be neglected throughout the study. Pressure drop experiments were conducted without heating as well since heat flux has no significant effect on friction factor in laminar region [20]. Experiments were repeated four times and the maximum relative error of repeated data and heat loss to exterior were less than 8% and %10, respectively. Overall heat loss reduced as Reynolds number increased.

Friction Characteristics

For fully developed laminar friction factor, Shah and London [21], Leon and Roman [22], Spiga and Morini [23] provided analytically solved equations for smooth rectangular ducts. Shah equation is given as:

$$f Re = 26(1 - 1.3553\alpha_c + 1.9467\alpha_c^2 - 1.7012\alpha_c^3 + 0.9564\alpha_c^4 - 0.2537\alpha_c^5) \quad (16)$$

Hydrodynamic development length is calculated using Eq. (5) and maximum development was found out as 25 mm, which corresponds to 3.9% of the channel. Therefore, hydrodynamic development effect inside the channel was ignored and results were presented with respect to fully developed friction factor throughout the study.

Figure 3 shows the plot of friction factor as a function of Reynolds number along with the results of Shah and London [21] for comparison. It can be seen that experimental data are found to be following the same trend with work of Shah and London [21], however higher. It is a well-known fact that roughness affects friction factor significantly and it has been researched widely. A recent numerical study of Pelevic and Meer [24] shows that an increase in

Table 3. Operating parameters and uncertainties

Parameters	Values	Uncertainties
G [t/h]	20 - 48	2.50 %
Q [W]	170 - 321	0.2 - 0.3 %
T_w [K]	295 - 311	± 0.5
T_f [K]	294 - 306	± 0.1
D_h [mm]	2.52	10 %
h_x [W/m ² K]	992-3242	8.4 - 13.1 %
Re	75 - 190	14 - 15.5 %
Nu	5.25 - 7.87	11.2 - 14.6 %
f	0.171 - 0.453	16.3 - 22.3 %

relative roughness by 2.93 % increases friction factor by 7 %. Correspondingly, the higher friction factor values are considered to be an accumulation of the presence of the

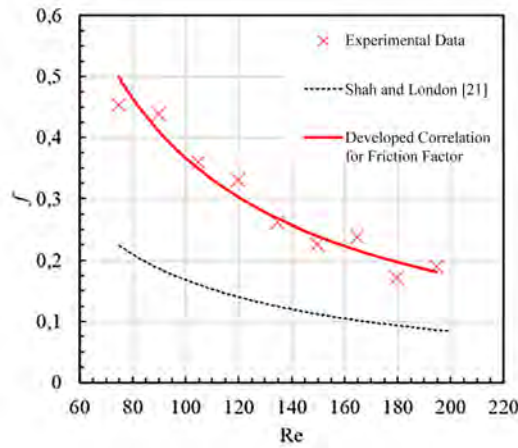


Figure 3. Friction factor versus Reynolds number

fins and possible roughness effect in this study. The aspect ratio was calculated ignoring the fin geometry and relative roughness is unknown for the channel.

While developing a correlation, as friction coefficient is known to be a function of Reynolds number, Eq. (17) is used. It is generalized formulation of laminar flow in ducts, given as:

$$f = \frac{C}{Re} \quad (17)$$

Where C is constant for different geometrical shapes. For example, C is 16 for smooth circular tubes while its value depends on aspect ratio for rectangular channels [25]. In this study, C was found as 37 and Eq. (18) is suggested to be utilized in the design of heat exchangers in the experimental range studied here.

$$f = \frac{37}{Re} \quad (18)$$

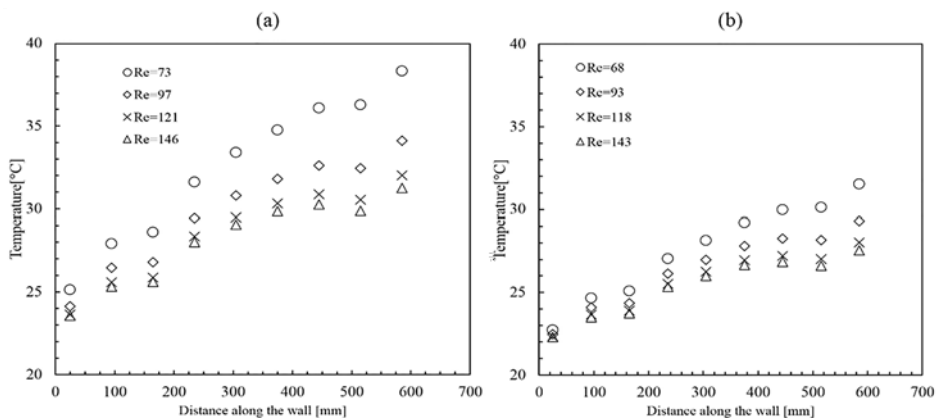


Figure 4. Temperature difference along the channel wall for heat fluxes (a) 5560 W/m²K (b) 3685 W/m²K

Heat Transfer Characteristics

In order to properly comprehend the effects of heat flux, two different heat flux rates, which are 3685 W/m²K and 5560 W/m²K, are used while conducting experiments. Figure 4 shows the effect of different heat flux rates on temperature along the wall. It can be seen from the figure that increasing heat flux increases the wall temperature and wall temperature difference between outlet and inlet of the channel. As Reynolds number increase, temperature difference between outlet and inlet of the channel reduces. This indicates that, in cooling applications, higher Reynolds numbers should be considered in laminar region for cooling applications. Theoretical Nusselt number for thermally developing flow is given for smooth rectangular cross sectional ducts with aspect ratios of 0.33 and 0.5, respectively, as [15]:

$$Nu_x = \frac{31.297 + 14867x^* + 622440x^{*2}}{1 + 2131.3x^* + 144550x^{*2} - 13297x^{*3}} \quad (19)$$

$$Nu_x = \frac{28.315 + 27038x^* + 1783300x^{*2}}{1 + 3049x^* + 472520x^{*2} - 35714x^{*3}} \quad (20)$$

As the current test channel has an aspect ratio of 0.359, a linear interpolation between Eq. (19) and (20) is done and the resulting equation is also provided in Fig. 5 along with the local Nusselt values of the experimental data varying with dimensionless thermal development length.

It can be seen in Fig. 5 that local Nusselt values show fairly good agreement and same trend with theory. However, before the flow converges into fully developed Nusselt value ($x^* < 0.1$), a distinct alteration occurs. While laminar developing theory shows a sharp change, experimental results are smoother. This is thought to be originating from the presence of the fins. Flow disturbances caused by fins further delays the formation of thermal boundary layer and increases heat transfer coefficient, correspondingly Nusselt

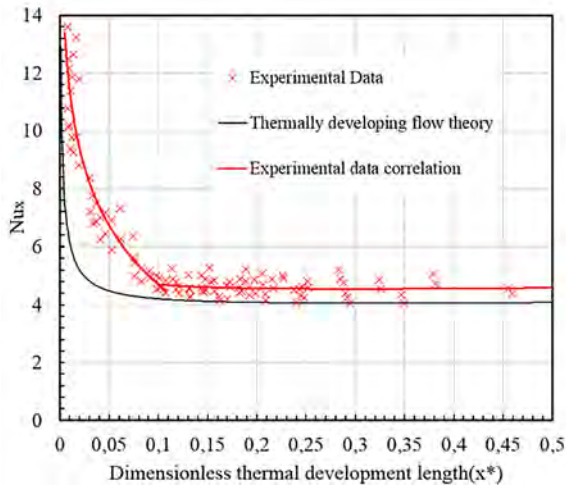


Figure 5. Local Nusselt number vs dimensionless thermal development length.

number. Therefore, in short channels where thermal development plays an important role, fin usage might be considered while designing small scale heat exchangers.

In order to determine local Nusselt values for the current channel, a new correlation is proposed considering the threshold is $x^* = 0.1$, as:

$$Nu_x = \begin{cases} Nu_x = -2.898 \ln(x^*) - 1.9606 & x^* < 0.1 \\ Nu_x = 4.71 & x^* > 0.1 \end{cases} \quad (21)$$

Figure 6 shows the average Nusselt number variation with Reynolds number with two Prandtl numbers (Pr). Thermal development length theory is plotted alongside with experimental results. It can be seen that both Reynolds number and Prandtl number enhance average Nusselt number as they increase. Study of Zhang et al [26] indicates the thermohydraulic performance of different multiport

microchannels with sawtooth fin structures. According to their conclusion, finned structures increase heat transfer rate as well as friction factor and fin geometry has a great impact on both characteristics. Experimental data of this study slightly overestimated thermal development theory. Bearing in mind the work of Zhang et al. and the results of the current study, the differences between experimental data and the theory can be due to the fins. In addition, as fluid temperature is assumed to be varying linearly along the channel, while it practically varies differently, this may be another reason of overestimation. It can also be concluded according to heat transfer results that, conventional theory is better used to predict heat transfer phenomenon in minichannels with hydraulic diameter as small as 2.519 mm.

General correlation form for thermally developing flow to predict Nusselt number in laminar flow is given as a function of Graetz number, which is defined as:

$$Gz = \frac{D_h}{L} Re Pr \quad (22)$$

Therefore, a new correlation is proposed to predict average Nusselt number in the given range of parameters, as:

$$Nu_m = 4.1 \left(Re Pr \frac{D_h}{L} \right)^{0.33} \left(\frac{\mu_f}{\mu_w} \right)^{0.14} \quad (23)$$

Performance Analysis

Experimental results of the fluid flow and heat transfer indicated the enhancement of heat transfer together with pressure drop. Therefore, in order to truly evaluate the usability of the channel, a performance evaluation criteria is defined as [27]:

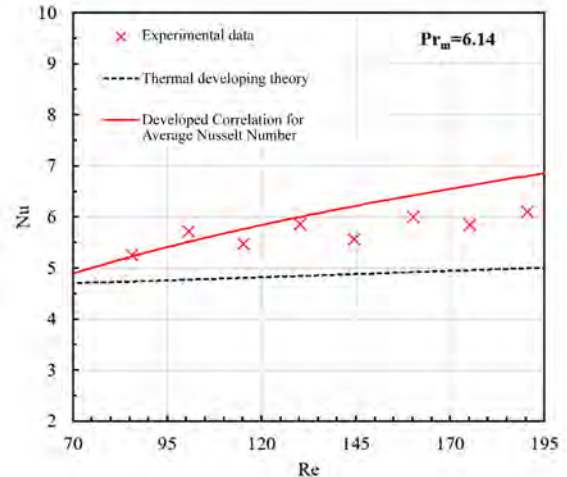
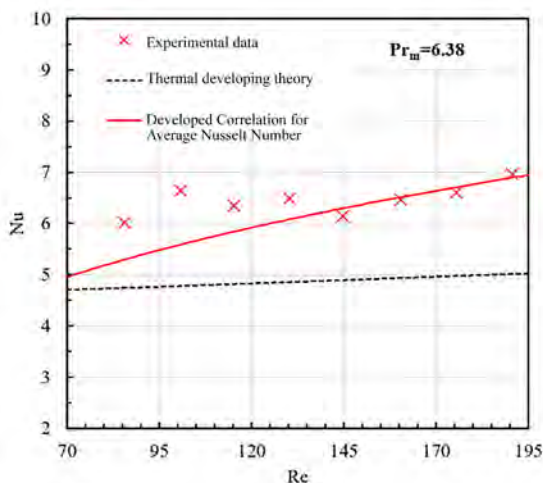


Figure 6. Average Nusselt number results in comparison with thermal development theory for (a) $Pr = 6.38$ (b) $Pr = 6.14$

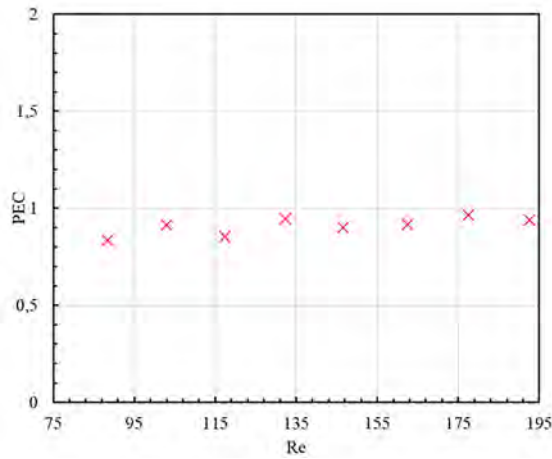


Figure 7. Performance evaluation criteria for the minichannel

$$PEC = \frac{Nu_{exp} / Nu_{theo}}{(f_{exp} / f_{theo})^{1/3}} \quad (24)$$

Since proposed correlations show the predictable values of thermohydraulic performance of the flow, in order to better visualize PEC values, those correlations were divided by theoretical values and used instead. Figure 7 shows the PEC values of the channel. As can be seen from the figure, PEC values are smaller than 1, which indicates that roughness and fin presence affect pressure drop more than they affect heat transfer rate.

CONCLUSION

Experimental investigation of laminar heat transfer and fluid flow analysis in a rectangular cross sectional multiport finned minichannel was conducted with constant heat flux boundary condition using deionized water. Reynolds number ranged between 70 and 190. Varying thermophysical properties of the working fluid and entrance effects were taken into consideration. Friction factor and convective heat transfer Nusselt numbers were calculated and compared with conventional and small scale correlations in literature and theory. Both friction factor and convective heat transfer Nusselt numbers showed higher values than theory. Three new correlations were developed to estimate friction factor, local Nusselt number and average Nusselt number in the given range of parameters. Performance evaluation criteria (PEC) analysis was conducted to assess the usability of the channel. Further studies should be done with similar channels without fins and with different fin geometries in order to fully comprehend the fin effect on minichannel.

ACKNOWLEDGMENTS

Authors are grateful to Turkish Academy of Sciences for their research support. Authors also thank to Mustafa Yalçın, technician at the department of mechanical engineering in Middle East Technical University, for his support in experimental setup and data measurement.

REFERENCES

1. Tuckerman DB, Pease RFW. High-Performance Heat Sinking for VLSI. *IEEE Electron Device Letters* Volume EDL-2 5 (1981) 126-129.
2. Mehendale, SS, Jacob AM, Shah RK. Fluid Flow and Heat Transfer at Micro- and Meso-Scales with Application to Heat Exchanger Design. *Applied Mechanics* 53 (2000) 175-193.
3. Kandlikar SG, Grande WJ. Evolution of Microchannel Flow Passages - Thermohydraulic Performance and Fabrication Technology. *Heat Transfer Engineering* 24 (2003) 3-17.
4. Wang G, Hao L, Cheng P. An Experimental and Numerical Study of Forced Convection in a Microchannel with Negligible Axial Heat Conduction. *International Journal of Heat and Mass Transfer* 52 (2009) 1070-1074.
5. Gunnasegaran P, Mohammed HA, Shuaib NH, Saidur R. The Effect of Geometrical Parameters on Heat Transfer Characteristics of Microchannels Heat Sink with Different Shapes. *International Communications in Heat and Mass Transfer* 37 (2010) 1078-1086.
6. Wu HY, Cheng P. An Experimental Study of Convective Heat Transfer in Silicon Microchannels with Different Surface Conditions. *International Journal of Heat and Mass Transfer* 46 (2003) 2547-2556.
7. Zhuo L, Wen-Quan T, Ya-Ling H. A Numerical Study of Laminar Convective Heat Transfer in Microchannel with Non-Circular Cross-Section. *International Journal of Thermal Sciences* 45 (2006) 1140-1148.
8. Hetsroni G, Mosyak A, Pogrebnyak E, Yarin LP. Fluid Flow in Micro-Channels. *International Journal of Heat and Mass Transfer*, 48 (2005) 1982-1998.
9. Hetsroni G, Mosyak A, Pogrebnyak E, Yarin LP. Heat Transfer in Micro-Channels: Comparison of Experiments with Theory and Numerical Results. *International Journal of Heat and Mass Transfer* 48 (2005) 5580-5601.
10. Lee PS, Garimella SV, Liu D. Investigation of Heat Transfer in Rectangular Microchannels. *International Journal of Heat and Mass Transfer* 48 (2005) 1688-1704.
11. Asadi M, Xie G, Sunden B. A Review of Heat Transfer and Pressure Drop Characteristics of Single and Two-Phase Microchannels. *International Journal of Heat and Mass Transfer* 79 (2014) 34-53.
12. Morini GL. Single-Phase Convective Heat Transfer in Microchannels: a Review of Experimental Results. *International Journal of Thermal Sciences* 43 (2004) 631-651.
13. Rosa P, Karayiannis TG, Collins MW. Single-Phase Heat Transfer in Microchannels: The Importance of scaling effects. *Applied Thermal Engineering* 29 (2009) 3447-3468.

14. Webb RL. Effect of Manifold Design on Flow Distribution in Parallel Micro-Channels. International Electronic Packaging Technical Conference and Exhibition 2 (2003) 527–535.
15. Kandlikar S, Garimella S, Li D, Colin S, King MR. Heat Transfer and Fluid Flow in Minichannels and Microchannels, Elsevier Ltd., Oxford, pp. 87–116, 2006.
16. Kakaç S, Yener Y. Convective Heat Transfer, Second edition CRC press, Washington, 1994.
17. Incropera F, Lavine A, DeWitt D. Fundamentals of Heat and Mass Transfer, Sixth Edition, New Jersey, 2007.
18. Altınöz M. Experimental Investigation of Single Phase Liquid Flow and Heat Transfer in Multiport Minichannels, Middle East Technical University, Ankara, 2013.
19. Holman JP. Experimental Methods for Engineers, Eighth edition McGraw–Hill, New York, pp. 64, 2012.
20. Dai B, Li M, Dang C, Ma Y, Chen Q. Investigation on Convective Heat Transfer Characteristics of Single Phase Liquid Flow in Multi-Port Micro-Channel Tubes. International Journal of Heat and Mass Transfer 70 (2014)114–118.
21. Shah RK, London AL. Laminar Flow Forced Convection in Ducts, Supplement 1 to Advances in Heat Transfer, New York Academic press, 1978.
22. Troniewski L, Ulbrich R. Two-Phase Gas-Liquid Flow in Rectangular Channels. Chemical Engineering Science, 39 (1984) 751–765.
23. Spiga M, Morini GL. A Symmetric Solution for Velocity Profile in Laminar Flow through Rectangular Ducts. International Community of Heat and Mass Transfer, 21 (1996) 283–296.
24. Pelevic N, van der Meer TH. Heat Transfer and Pressure Drop in Microchannels with Random Roughness. International Journal of Thermal Sciences 99 (2016) 125–135.
25. Kakac S, Shah RK, Aung W. Handbook of Single-Phase Convective Heat Transfer, JohnWiley and Sons Inc., New York, 1987.
26. Zhang J, Diao Y, Zhao Y, Zhang Y, Sun Q. Thermal-Hydraulic Performance of Multiport Microchannel Flat Tube with Sawtooth Fin Structure. International Journal of Thermal Sciences 84 (2014) 175–183.
27. Webb RL. Performance Evaluation Criteria for Use of Enhanced Heat Transfer Surfaces in Heat Exchanger Design. International Journal of Heat and Mass Transfer 24 (1981) 715–726.

NATIONAL & INTERNATIONAL SCIENTIFIC EVENTS

MULTIPHYSICS 2016

Venue: ZHAW School of Engineering
Location: Zurich, Switzerland

BEGINS: Dec 08, 2016
Ends: Dec 09, 2016

11th Triennial Congress of the World Assoc.ion of
Theoretical and Comput. Chem. (WATOC2017)

Venue: Gasteig München GmbH
Location: Munich, Bavaria, Germany

BEGINS: Aug 27, 2017
Ends: Sep 01, 2017

2016 8th International Conference on
Bioinformatics and Biomedical Technology (ICBBT
2016)

Venue: Hotel Colón
Location: Barcelona, Spain

BEGINS: Jun 10, 2016
Ends: Jun 12, 2016

2016 7th International Conference on
Environmental Science and Technology (ICEST
2016)

Venue: HOTEL COLÓN
Location: Barcelona, Spain

BEGINS: Jun 10, 2016
Ends: Jun 12, 2016

2016 5th International Conference on Petroleum
Industry and Energy (ICPIE 2016)

Venue: Colón Hotel Barcelona
Location: Barcelona, Spain

BEGINS: Jun 10, 2016
Ends: Jun 12, 2016

2016 3rd Int. Con. on Mech. and Mechatronics
Res. (ICMMR 2016)--Ei & Scopus (ICMMR 2016)

Venue: Crowne Plaza Chongqing Riverside
Location: Chongqing, China

BEGINS: Jun 15, 2016
Ends: Jun 17, 2016

2016 2nd Int. Con. on Power Control and Opt.
(ICPCO 2016)--Ei & Scopus (ICPCO 2016)

Venue: Crowne Plaza Chongqing Riverside
Location: Chongqing, China

BEGINS: Jun 15, 2016
Ends: Jun 17, 2016

WCSE 2016 6th International Workshop on
Computer Science and Engineering _ EI, SCOPUS

Venue: Park Hotel Tokyo
Location: Tokyo, Japan

BEGINS: Jun 17, 2016
Ends: Jun 19, 2016

ICEIM 2016 5th Int. Con. on Engineering and
Innovative Materials_SCOPUS, Ei Compendex

Venue: Amb. Row Hotel Suites by Lanson Place
Location: Kuala Lumpur, Malaysia

BEGINS: Sep 10, 2016
Ends: Sep 12, 2016

2016 3rd Int. Conf. on Power and Energy Systems
Engineering (CPESE 2016)

Venue: Kitakyushu Int. Conference Center
Location: Kitakyushu, Japan

BEGINS: Sep 08, 2016
Ends: Sep 10, 2016

ICRED 2016 2nd International Conference on
Renewable Energy and Development_Ei, Scopus

Venue: Kitakyushu Int. Conference Center
Location: Kitakyushu, Japan

BEGINS: Sep 08, 2016
Ends: Sep 10, 2016

2016 5th International Conference on Nutrition
and Food Sciences --Ei Geobase

Venue: Ananta Legian Hotel
Location: bali, Indonesia

BEGINS: Jun 25, 2016
Ends: Jun 27, 2016

